UNIVERSITY OF MINNESOTA

This is to certify that I have examined this copy of a doctoral dissertation by

Wei Zhou

and have found that it is complete and satisfactory in all respects,
and that any and all revisions required by the final
examining committee have been made.

James R. Leger

Name of Faculty Adviser

Signature of Faculty Adviser

Date

Miniature Computer-Tomography-Imaging-Spectrometer

A DISSERTATION
SUBMITTED TO THE FACULTY OF THE GRADUATE SCHOOL
OF THE UNIVERSITY OF MINNESOTA
BY

Wei Zhou

IN PARTIAL FULFILLMENT OF THE REQUIREMENTS
FOR THE DEGREE OF
DOCTOR OF PHILOSOPHY

James R. Leger

December 2007

Acknowledgements

It has been a great honor to have Professor James Leger as my doctoral advisor. I greatly appreciate his countless encouragement, support, inspiration and commitment throughout my entire PhD study. I will always remember my time working in his group with great fondness.

I am also very grateful for having an exceptional doctoral committee and wish to thank professors Anand Gopinath, Joseph Talghader and Tanner Akkin. Their support and advice over the years have been very helpful, and thanks for the gracious service as my academic committees.

I am very grateful for all of the help I received from the staff at the University of Minnesota's Nanofabrication Center. I have had the honor of working with a number of outstanding graduate students. I am particularly indebted to Eric shields for his patience and support early in my graduate career. I would also like to thank Zhaohui Yang, Bing Hao, Mercedeh and Brad.

My parents have given me unconditional support throughout my academic career (and even before!). Everything I have achieved so far would not have been possible without them.

Finally, I would like to thank my wife, Meixia. Her inspiration and support throughout the ups and downs of my graduate career were invaluable. She has been a source of great strength in my life and I look forward to our future.

Dedication

This dissertation is dedicated to my family and friends. A special feeling of gratitude to my wife and loving parents, whose words of encouragement and push for tenacity ring in my ears. I also dedicate this dissertation to my many friends who have supported me throughout the process. I will always appreciate all they have done.

Abstract

A novel design methodology for the miniature imaging spectrometer has been demonstrated. The Computer-Tomography detection scheme is applied because of its inherently large etendue and snap-shot function. As opposed to the traditional CTIS design that employs only one dispersive element to generate all different spectral and spatial information mixing, the idea of independent information collection and multiple-channel array structure is introduced. Based on this idea our design will not only achieve a very compact sensor structure for limited system aperture size, but also dramatically reduce the alignment and assembly difficulty compared with other micro imaging spectrometers.

By combining diffractive, refractive and graded-index (GRIN) optics into single optical element, every information channel consists of three quarter-pitch GRIN lenses (diameter of 250um) with an on-axis dispersion imaging function. By rotating the information channel to arbitrary azimuthal directions along the optical axis, different dispersion mixing is introduced to the same object's image. This scheme provides the freedom of increasing information channels for higher spectral resolution.

One miniature CTIS sensor was designed with 16 information channels in a 1mm x 1mm x 2mm cube. A single channel was fabricated and tested. A Focused-Ion-Beam Etch method was employed to directly fabricate the grating on the cylinder GRIN lens. A simple but efficient hyper-spectral information reconstruction algorithm was built up and successfully tested with NASA AVIRIS satellite hyperspectral data. The designed sensor performance was tested with different polychromatic objects.

Table of Contents

List of Figures

1. Background

Since Isaac Newton[1] first defined the "spectral" in 1704 by separating sunlight into its constituent colors with a prism, spectroscopy has been developed significantly. Spectroscopy was first applied to astronomy in 1817 by Joseph Fraunhofer [2] to study the solar atmosphere components. Today it is an important and efficient way to study the stars and trace the origin of the universe.

For many years spectroscopy technology has been tightly combined with astronomy, for fulfilling the human curiosity on the far-away universe. Today the spectro-photometric devices that distinguish the atmospheric chemistry of distant planets have found applications on Earth with the help of optical imaging technology[3]. Sophisticated airborne and space-based imagers from NASA, such as the Airborne Visible-Infrared Imaging Spectrometer (AVIRIS)[4] and the Hyperspectral Digital Imagery Collection Experiment (HYDICE)[5], are enabling precision agriculture[6], geological applications[7], urban applications[8] and environment surveillance[9, 10]. For example, by collecting the spectral information of land scenes, scientists can distinguish different species from each other. In agriculture this technology is applied for plant harvest pre-evaluation. In recent years, the combination of optical imaging and spectroscopy has been applied to medicine and manufacturing[11, 12]. This has led to the development of modern macro/micro imaging spectrometers, which motivated the research presented in this thesis.

In this chapter, the fundamental theory of traditional imaging spectrometers is reviewed in the first section. Micro optical imaging system design rules are studied in

detail in the second section. Following the theoretical discussion, a micro push-broom imaging spectrometer's design and fabrication process is presented in the third section to serve as a successful micro imaging spectrometer design example[13].

1.1 Imaging spectroscopy fundamental

1.1.1 Basic category

Based on the amount of spectral detail measured, imaging spectroscopy can be categorized into three types[14]: multispectral, hyperspectral and ultraspectral. Multispectral spectroscopy deals with discrete and relatively narrow spectral bands. Multispectral sensor may have many bands covering the spectral from the visible to the longwave infrared, e.g., a sensor with 40 discrete spectral bands covering the VIS, NIR MIR and LIR is categorized as multispectral. Nevertheless, because of its measurement of "discrete and narrow bands", multispectral detection does not produce the "spectral" of an object.

Hyperspectral spectrometers measure narrow spectral bands over a contiguous spectral range and produce the spectra of all pixels in the scene. A sensor with only 30 bands can be hyperspectral if the 30 bands are 10-nm wide continuously covering the spectral range of 400 to 700nm.

The term "ultraspectral" is typically reserved for interferometric-type imaging sensors with very fine spectral resolution. These sensors often have a low spatial resolution of only a few pixels, a restriction imposed by the high data rate.

Imaging spectrometers are primarily based on multispectral and hyperspectral technologies.

1.1.2 Detection Schemes

The objective of imaging spectrometers is to measure the "spectra" of a two-spatial-dimensional scene and the intensity distribution over the wavelength. This $I(x,y,\lambda)$ information base is often referred to as the "data cube", where x and y represent spatial coordinates and λ represents wavelength. The basic unit in this data cube is called "voxel", corresponding to the fundamental spatial-spectral resolution of an imaging spectrometer.

This special three-dimensional information base has an interesting property -- the spectral information is fundamentally different from spatial information so that it can be separated from spatial information very well with a variety of methods. This leads to different hyper-spectral information detection methods. The easiest approach is to simply put multiple band-pass filters in front of a traditional two-dimensional detector. Every color filter has certain narrow spectral bandwidth to provide the desired spectral resolution. The combination of different color filters either covers certain continuous spectral ranges (hyperspectral instruments), such as in the AVIRIS system with 224 spectral channels to cover 400~ 2500nm wavelength range, or only picks up certain interesting discrete spectral bands (multispectral instruments). This kind of imaging spectrometers is normally called a "color filter imaging spectrometer". Since every shot

collects all spatial information but discrete spectral information, this detection scheme is categorized as a spectral scanning scheme, as shown in figure 1-1.

Color filter imaging spectrometers normally require a complicated instrument structure. Instruments have to carry all the filters during the detection. In the temporal-slow-variation environment like land-base detection, a small detector is employed with color filter switching mechanics. A single shot collects the spatial intensity distribution from one spectral band; hence a relatively long detection time is required. For the temporally fast-variation detection case like air-based remote sensing where detection time is extremely limited, a color filter detector array is normally used. Every detector corresponds to the entire spatial image of the object and one spectral band, so the detector size is proportional to the number of spectral bands.

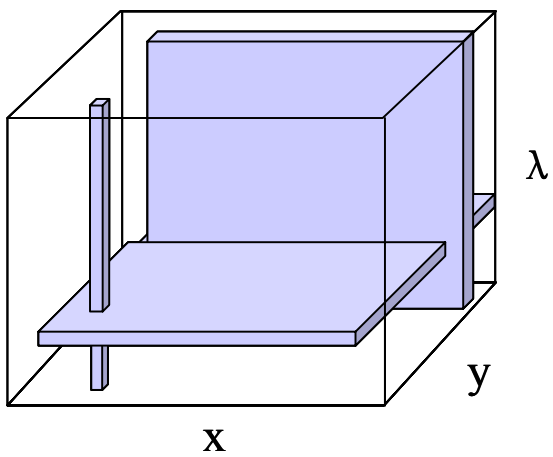

Figure 1-1, Hyperspectral information date base and associated detection schemes

In air-based or space-based detection the space for instruments is very limited. Therefore another detection scheme is normally employed, which scans in the spatial domain rather than in the spectral domain. The instrument's entrance pupil is designed to be a one-directional slit, which is perpendicular to the direction of flight. A single shot only collects a one-dimensional slit image. Light from this one-dimensional image is dispersed perpendicular to the slit by a dispersive element, either a grating or a prism, forming a two-dimensional light pattern of spectral and spatial information. Information regarding successive one-dimensional image slices is usually obtained by moving the spectrometer along the perpendicular spatial dimension, often by flying the spectrometer in a straight-line path across the object field. This detection scheme also requires a two dimensional detector. Creating a two-dimensional image in this way is reminiscent of the sweeping action of a push broom, giving rise to the name of the architecture as a "push-broom imaging spectrometer". The classic structure of this type of instruments is shown in figure 1-2.

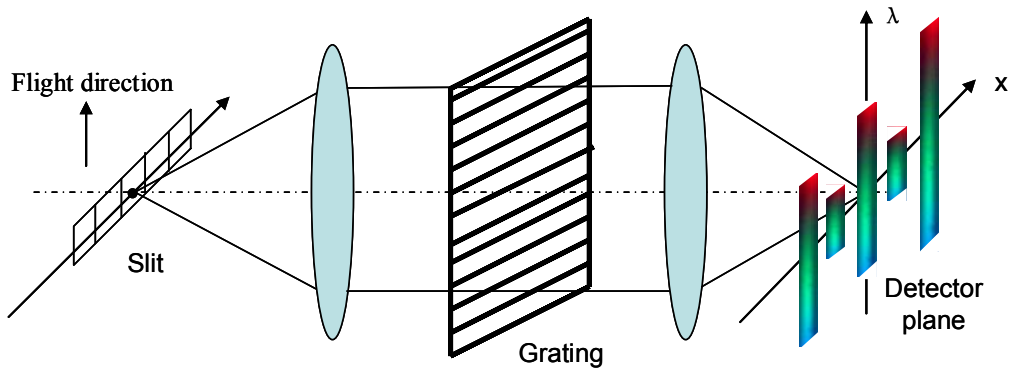

Figure 1-2 Traditional push-broom imaging spectrometer design

One modification of this spatial scanning detection is to design the instrument entrance pupil as a two-dimensional aperture instead of a one dimensional slit. A single shot will only collect one spatial pixel from the scene. The dispersive element spreads the spectral information of this spatial point onto a one-dimensional detector. So while the instrument has to scan in both spatial directions to achieve three-dimensional hyperspectral information, only one dimensional detector is required in the system. This kind of instruments is called "whisk-broom imaging spectrometer".

Since the spatial scanning detection scheme employs a dispersive element, which provides the continuous spectral analysis ability in certain wavelength range, this type of instruments is only used for hyperspectral detection.

In additional to scanning schemes, there is another detection scheme that utilizes multiplexing technology to achieve snap-shot detection by mixing the spectral information with the spatial information and using a traditional two-dimensional detector to collect the distorted images. The three-dimensional hyperspectral information is obtained by post data processing. Computer-Tomography Imaging Spectrometers (CTIS) uses this non-scan detection scheme. The primary parts of this thesis will explore the CTIS method in some detail.

1.2 Micro-imaging spectrometer design requirements and limitations

1.2.1 Resolution

The two most important performance criteria of imaging spectrometers are spatial resolution and spectral resolution. The spatial resolution of the object field is

fundamentally limited by the object-side numerical aperture of the fore-optics through Abbe's resolution equation. Therefore any design of a spectrometer that requires high object-space resolution must contain appropriately sized fore-optics. However, care must be taken in designing the subsequent optical system to ensure that this resolution is not compromised. This simply means that the numerical aperture on the image side of the fore-optics must be matched or exceeded by the optics contained in the micro-spectrometer array. A key advantage of using a microspectrometer is that many lens and mirror aberrations are reduced by the micro-optical format[15].

A similar statement can be made regarding the spectral resolution of a grating spectrometer. Although there are a variety of techniques for designing high-resolution spectrometers, the resolving power of a simple blazed grating is limited by the product of the number of grating lines and the diffraction order utilized. Since there is a limit to the minimum grating pitch, high spectral resolution gratings are generally physically large in size. Thus, systems that require high spatial and spectral resolution are inherently large in volume. It is easy to show that a grating spectrometer is diffraction-limited by its grating of width w when the spectrometer slit has a half-width y of at most

$$\Delta y = \frac{f\lambda}{w} \tag{1-1}$$

where $\boldsymbol{f}$ is the focal length of the collimating mirror or lens in front of the dispersive element and $\boldsymbol{\lambda}$ is the wavelength of light. To completely capture the light cone from the fore-optics, the f-number of the spectrometer must be at least as low as the f-number of

the fore-optics. By equating these two lens speeds, the resolving power of a first-order grating is given by.

$$\frac{\lambda}{\Delta\lambda} = \frac{f}{p\ (f/\#)} \tag{1-2}$$

where ***p*** is the grating pitch and (*f*/#) is the f-number of the fore-optics. Clearly, the resolving power is proportional to the mirror focal length, and will be reduced in a grating-based microspectrometer when compared to its macrospectrometer counterpart.

1.2.2 Etendue

The optical throughput or etendue of the spectrometer is considered next. This figure of merit is important in assessing the amount of power that will be passed by the instrument, and ultimately, together with the detector characteristics, determines the signal-to-noise performance of the spectrometer. The etendue of the spectrometer can be defined as the area of the light passed by the slit multiplied by the light divergence solid-angle that is accepted by the collimating mirror and grating.

Let us consider the case of a push-broom microspectrometer with a single grating placed in the system aperture. Assuming that the slit width is chosen according to Eq. 1-1 (and the NA of the microoptics exceeds that of the fore-optics), the angular divergence exiting the slit and passed by the grating should be the same as the numerical aperture of the light incident on the slit. Thus, the one-dimensional etendue in the spectral direction will be the same for a macro-spectrometer and a micro-spectrometer. The etendue of either spectrometer can be increased by opening the slit beyond the diffraction limit at the

cost of a reduction in spectral and spatial resolution. It can be argued that a macro-spectrometer (with a larger focal length f and larger grating) starts out with a higher spectral resolution, allowing a certain degree of the resolution be traded for increased throughput. However, the spatial resolution in the cross-slit (y) direction is also compromised by enlarging the spectral slit. Thus, if a full spatial resolution in the cross-slit direction is required because of the diffraction limit of the fore-optics, the one-dimensional etendues of the micro- and macro-spectrometers are identical.

1.2.3 Structure size

From a general system design point of view, a miniaturized sensor structure can be achieved in three steps. A concise architecture should always be designed first with all required functions and desired performance. The fewer optical elements involved, the smaller sensor physical size can be achieved.

The second step is decreasing individual optical element size without significantly compromising system quality. It is well known that an imaging lens' point spread function will not be affected by changing the lens' diameter if the lens' *f*/# is maintained. This suggests that an optical imaging system depth can be minimized by proportionally decreasing the aperture size and lens' focal length. The advantage is that less aberration will be carried in the system with small aperture size, while the disadvantage is that the object side angular resolution has to be sacrificed proportionally.

This leads to the third step of system miniaturization. A fore optics with large aperture size can be used to maintain object side resolution, and an array of miniaturized

imagers is positioned at the image plane of the fore optics. Individual small imagers only pick up a portion of the image. As long as the small imager object side NA matches the fore optics image side NA, the whole sensor's object side resolution can be preserved even though the sensor depth is dramatically decreased.

1.3 Micro Imaging Spectrometer Design Example

1.3.1 System overview

Many modern optical imaging spectrometers are capable of collecting data at rates that greatly exceed computational capabilities. Hyperspectral imagers, for example, simultaneously generate spectral and spatial data with high resolution and space-bandwidth product (SBP). The number of spectral data points collected per image point is generally fixed at the maximum value across all image points (i.e. space-invariant), resulting in an exceedingly large information bandwidth. For example, the HYDICE and AVIRIS spectrometers collect data at over 200 wavelengths for every image pixel and generate 0.725 and 3.175 GBytes data per second, respectively[16]. These are both airborne systems, and the data are recorded during flight and then processed after the aerial vehicle has landed.

The large amounts of data generated by these and similar hyperspectral systems present two major concerns. First, the amount of useful information within these data sets is often quite small. In some applications, this can be on the order of a few percent. Analysis of these data can require computationally intensive data mining techniques[17]. Real-time data processing is often expensive, if not impossible. This data processing

challenge is likely to grow, as larger detectors are developed that collect even more detailed information. The transmission of the data in its raw form represents an additional challenge. For satellite-based applications, transmitting these large data sets in real-time is often impossible, even with aggressive compression.

A second design concern with hyper-spectral imaging systems is the overall size and weight of the hardware. Since many hyperspectral systems are used in aerial surveillance, these concerns often constrain the design. Therefore, it is desirable to explore optical architectures that promote miniaturization while maintaining system performance. In addition to airborne and space-borne platforms, there are non-traditional application areas that may benefit from hardware miniaturization.

The following example describes a prototype hyperspectral imaging system that offers solutions to both these issues. It utilizes microelectro-mechanical systems (MEMS) components to modify the dispersive power of the spectrometer on a pixel-by-pixel basis by controlling the light path within the spectrometer in a dynamic manner. Thus, the spectral resolution is both space-variant (a function of the image-point location) and adaptive (able to change with time) to optimize spectral performance. An additional dynamic adjustment of the central wavelength could be added to offer a complete control over the spectral response of each pixel. With proper feedback control, the overall system is able to adjust the spectral characteristics of each image point to achieve optimal information extraction.

The second innovation consists of designing the spectrometer in an integrated micro-format to occupy a very small volume. An array of these micro-spectrometers can cover an arbitrarily large image format.

1.3.2 System design

The basic concept of the entire system is shown in figure 1-3. Figure 1-3(a) shows the entire system. An image containing high spatial resolution is projected onto the entrance slit of the spectrometer array by the fore-optics. A relatively small number of pixels is grouped into a sub-image and processed by a single micro-spectrometer. By constructing an array of these micro-spectrometers in the direction of the one-dimensional image, an arbitrarily large SBP image can be spectrally resolved with a very compact spectrometer assembly.

The adaptive space-variant nature of each micro-spectrometer is illustrated in figure 1-3(b). The spectral slit shown for a single micro-spectrometer is composed of many individual MEMS mirrors in a linear array. Each mirror performs the dual role of acting as the spectrometer slit oriented along the x-direction as well as controlling the light path through the spectrometer from a single pixel in the one-dimensional image. The ability to control this internal optical path dynamically on a pixel-by-pixel basis allows the device to be used in an adaptive space-variant manner, in this case adjusting the dispersion of each image point.

A planar-optics geometry was chosen for the adaptive space-variant micro-spectrometer design. All the optical elements are patterned on the surfaces of a single

bulk substrate to allow the light to propagate freely along a zigzag path within the substrate[18]. The basic geometry of the spectrometer is shown in figure 1-4. The optical layout is identical to that of figure 1-3, where the y-axis in figure 1-3 is rotated into the plane of the substrate and the z-axis is rotated in the y-direction to form the zigzag path. Thus, all the optical elements are inherently used in an off-axis manner.

The fore-optics image a scene onto the spectrometer entrance slit defined by a one-dimensional array of tilting MEMS mirrors. In this particular design, the MEMS mirrors are fabricated to be larger than the diffraction-limited slit-width, and an image of a slit is projected onto the mirror surface by the fore-optics. This makes it possible to externally adjust the width of the slit. The light reflected from these MEMS mirrors is collimated by the first micro-mirror and directed to one of three blazed gratings for spectral dispersion. The dispersed light is focused by the second micro-mirror onto the two-dimensional detector array. In this way, the spectral dispersion of every point in the one-dimensional image can be dynamically adjusted to an optimum value.

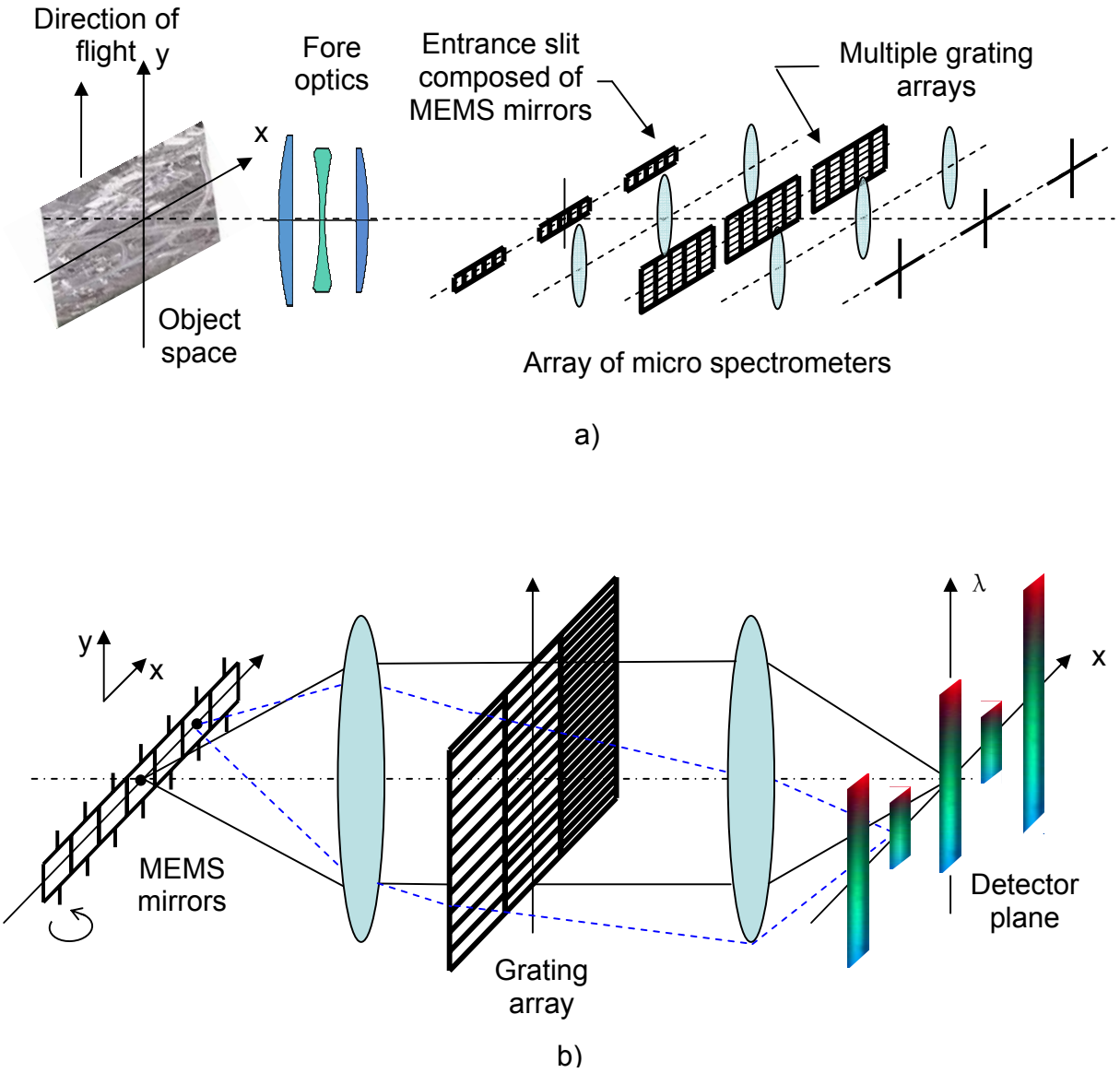

Figure 1-3 Optical architecture of adaptive space-variant microspectrometer. a) Full system including fore-optics and micro-spectrometer array. b) Expanded view of single micro-spectrometer (diffraction angle bend not shown)

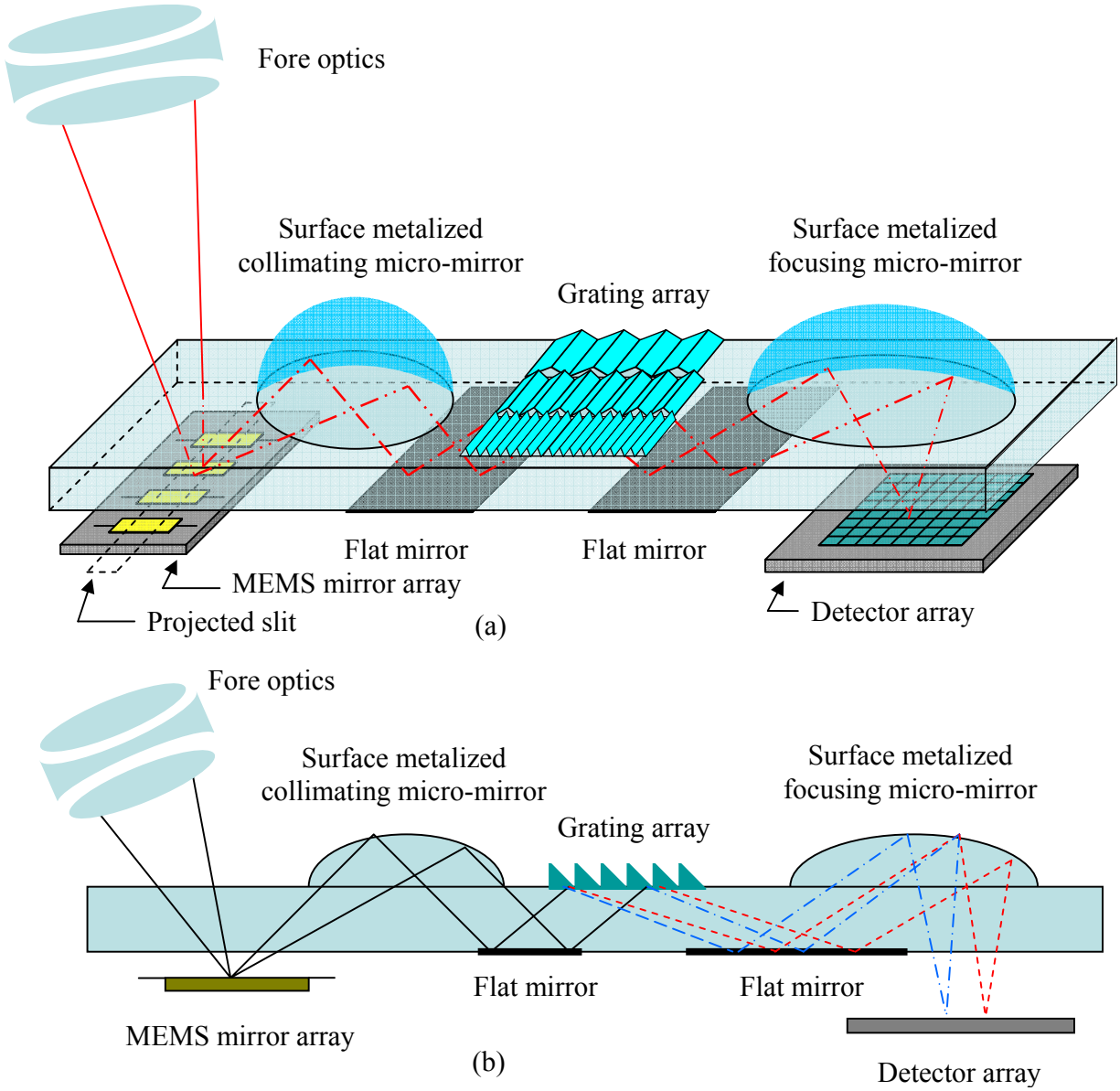

Figure 1-4 Schematic diagram of the imaging spectrometer: a) 3-D view, b) side view, showing two spectral components.

1.3.3 Sensor fabrication

Since all optical elements are assembled on the same substrate surface, the fabrication and integration of this micro imaging spectrometer can be greatly facilitated with modern micro-fabrication technology. Traditional photolithography is applied for fabricating the two surface-metalized micro-lenses fabrication, while the grating array is patterned with an e-beam-lithography tool.

The MEMS mirror array that comprises the spectrometer entrance slit is the key component for achieving the adaptive and space-variant performance. This MEMS mirror array was designed in-house specifically for this purpose. The individual electrically-controlled tilting mirrors direct the light of each pixel along a specific path through the spectrometer. The width of each individual mirror in the x-direction (along the slit and the one-dimensional image) was chosen to match the fore-optics point spread function width (Airy disk diameter of 24μm). The mirror length in the y-direction was designed to be 200μm. This large width in the spectral slit direction was specifically chosen so that the etendue of the spectrometer could be enlarged at the cost of spectral resolution.

The MEMS mirrors were designed to continuously rotate by ±4 degrees to direct the light to any of the three gratings. Each spectrometer was designed to resolve 10 pixels in the one-dimensional image, so 10 independently addressable mirrors were supplied at the entrance slit of each spectrometer. The large mirror length-to-width ratio increases the mirror fabrication difficulty, making the mirror supporting beam size a critical factor. The mirror collapse voltage (under which the supporting beam will break) and the pull-in voltage (where the edge of the tilted mirror contacts the bottom electrode, shorting the

mirror and the bottom electrode) were calculated to provide the initial geometrical size of the supporting beam[19].

The MEMS mirror array chip was fabricated by MEMSCAP Inc. using the PolyMUMPs process[20]. The mirror supports consist of polysilicon, using silicon nitride as an electrical insulator and aluminum as an electrical conductor and optical reflector. The mirror design and a SEM picture of a single free-standing mirror are shown in figure 1-5 (a) and (b). To achieve the maximum tilt angle with the minimum voltage, the supporting beams' geometrical size was optimized by adjusting the beam thickness through a dry-etching post-processing.

The performance of the MEMS mirrors is illustrated in figure 1-6. By applying the proper voltage, the mirrors were driven to rotate through their range of angles. The resulting laser spot deflection can be seen in the figure. The mirror response time to applied voltage was measured to be less than 5 μs.

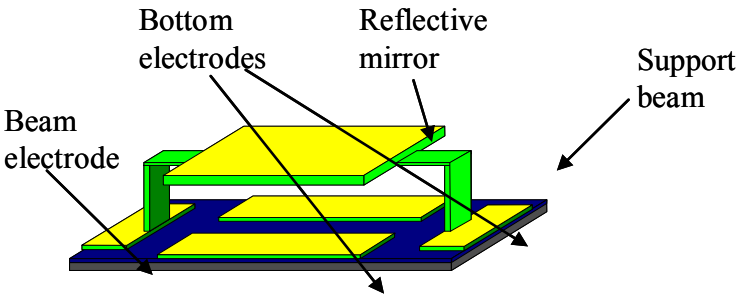

(a) MEMS mirror three-dimensional diagram.

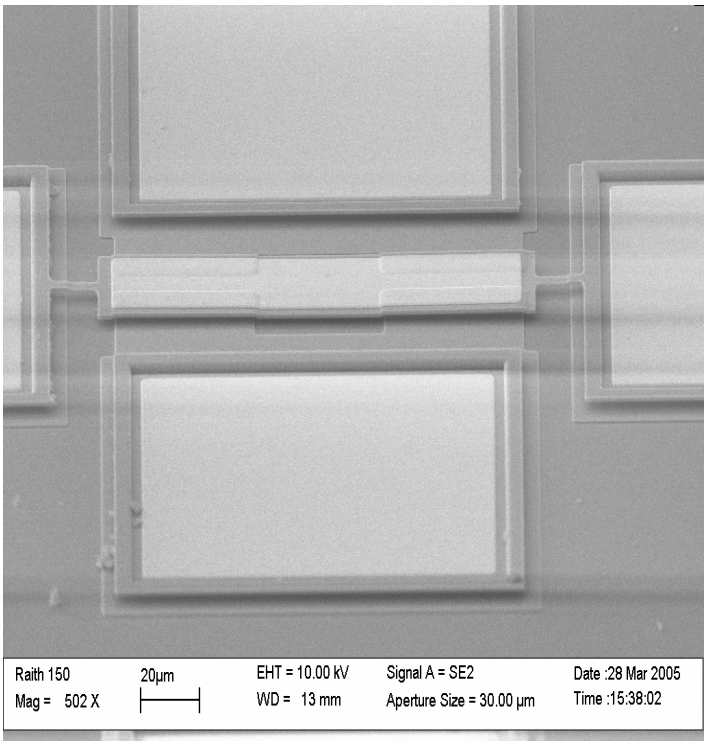

(b) SEM picture of a single MEMS mirror

Figure 1-5 MEMS mirror structure diagram

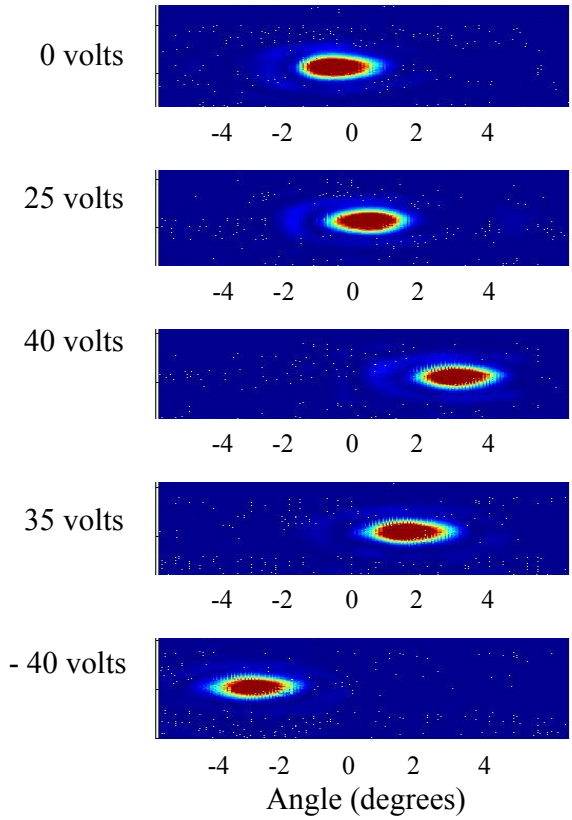

Figure 1-6 MEMS mirror rotation angle measurement

1.3.4 System performance test and conclusion

The spectrometer was first tested with a HeNe laser with a wavelength of 632.8nm. The measured point-spread functions and theoretical curve are shown in figure 1-7. The spectrometer was also tested with a helium discharge tube. These data are shown in figure 1-8. The reference data were measured with a Bausch and Lomb monochromator. The micro-spectrometer can successfully measure the peaks of the spectrum, subject to its resolution constraints.

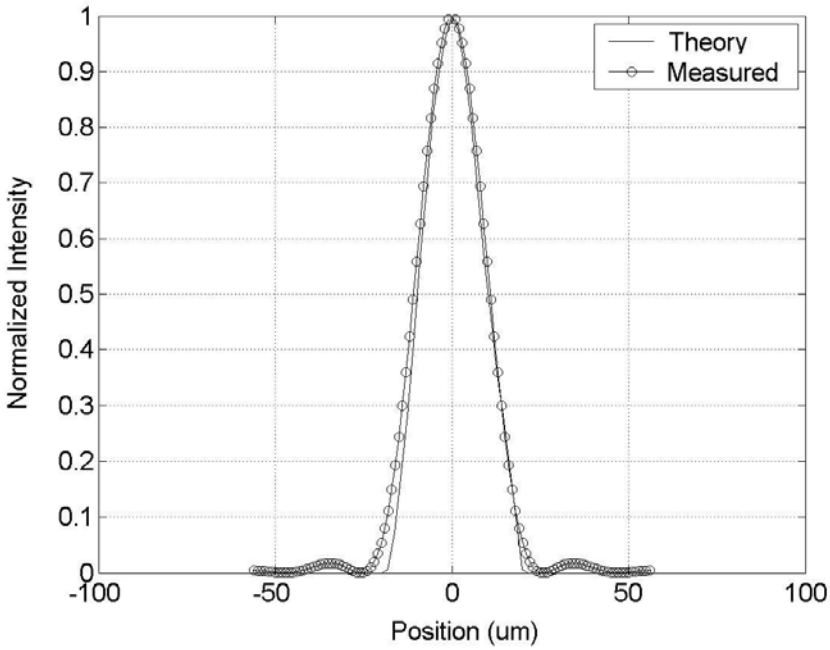

Figure 1-7 System point spread function measurement

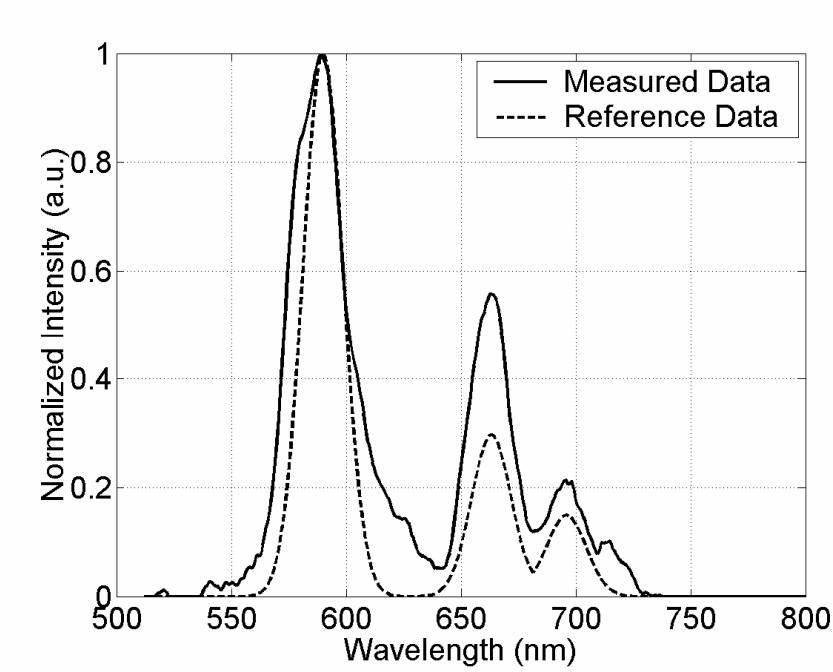

Figure 1-8 Spectrometer performance tested with a continuous source

2. Computer Tomography Imaging Spectrometers (CTIS) detection scheme

Traditional imaging spectrometers collect hyper-spectral information by scanning either in the spatial domain (push-broom imaging spectrometer) or in the spectral domain (color-filter imaging spectrometer). These classical detection schemes are only useful for the objects with slow time variation. In certain applications with fast time variation, like bio-imaging, a real-time detection scheme is critical to accommodate the short time variation.

While traditional spectroscopic techniques require some type of scanning to measure the three-dimensional data cube with a two-dimensional detector, new techniques are emerging that can measure the whole cube within a single frame of data[21,22]. One of these is the computed-tomography imaging spectrometer (CTIS)[23,24]. As the name suggests, this spectrometer uses tomographic techniques to computer the data cube.

In conventional medical computer tomography[25], a two-dimensional section of a body is projected onto a line detector by an X-ray line source on the opposite side of the body. By moving the source and detector around the body simultaneously, multiple images can be collected associated with different azimuthal projections. Then an image can be constructed based on those projections to show the information detail in the corresponding two-dimensional section of the body. Hence the key idea of tomography is projection, i.e., projecting the information of an object that cannot be directly measured to an easily accessed detector.

In many ways, the CTIS detection scheme is similar to medical CT. Basic CTIS theory is presented in the first section of this chapter. A corresponding frequency domain analysis and the detection resolution based on the sampling theory are discussed in the second section.

2.1. CTIS fundamentals

For an object with three dimensional information (x, y, λ), a traditional imaging system maps the collected photons on to the detector in a pan-chromatic manner. Individual detector pixels integrate across all wavelengths and provide an intensity distribution in the image plane. Since the intensity distribution on the image plane is the sum of the spectral information from the same spatial point, we can view non-dispersive imaging as a projection from the three-dimensional hyper-spectral space onto the two dimensional spatial domain along the spectral axis as shown in figure 2-1 (a).

Naturally, with a dispersive element in an imaging system, the parts of the two dimensional images corresponding to different spectral features will be shifted from each other, as shown in figure 2-1(b) and (c). Each detector pixel sums the photons from several object points. This is equivalent to a projection along different angles with respect to the spectral axis.

To simplify the analysis, let us assume the projection occurs in a two dimensional domain (x, λ). One projection mixes the two dimensional intensity distribution onto a one dimensional detector array (as figure 2-1 shows). This line integral through the projection determines one line through the origin in Fourier space of the two dimensional object, (as

shown in figure 2-2). By varying the dispersion and projection directions, different line integrals will result; therefore, the Fourier space can be reasonably covered. Similar projections can be carried out in the three dimensional case.

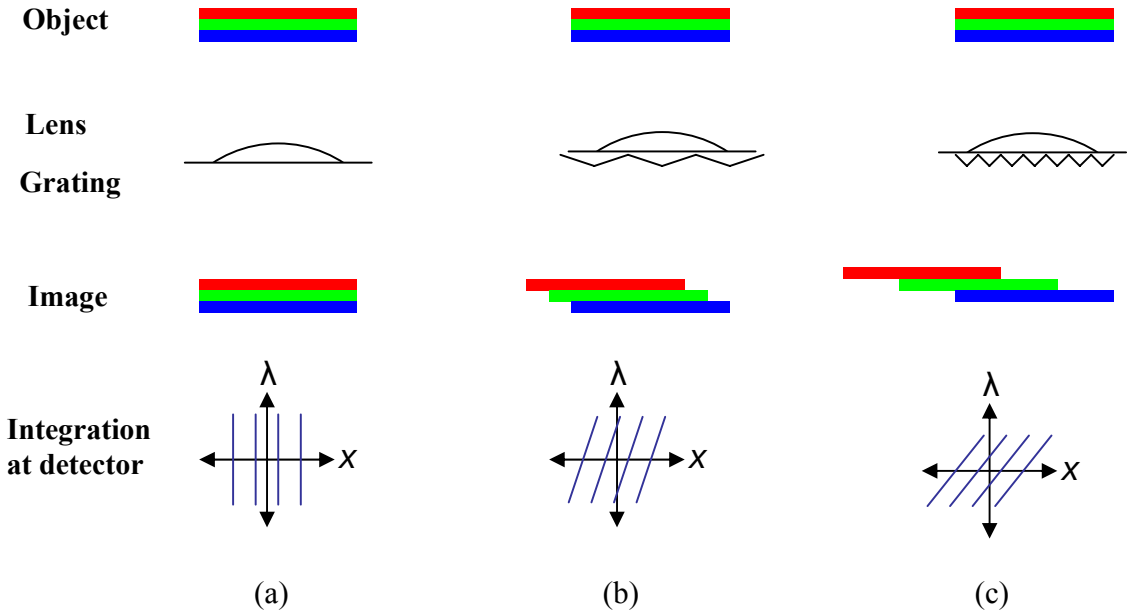

Figure 2-1 CTIS recording scheme

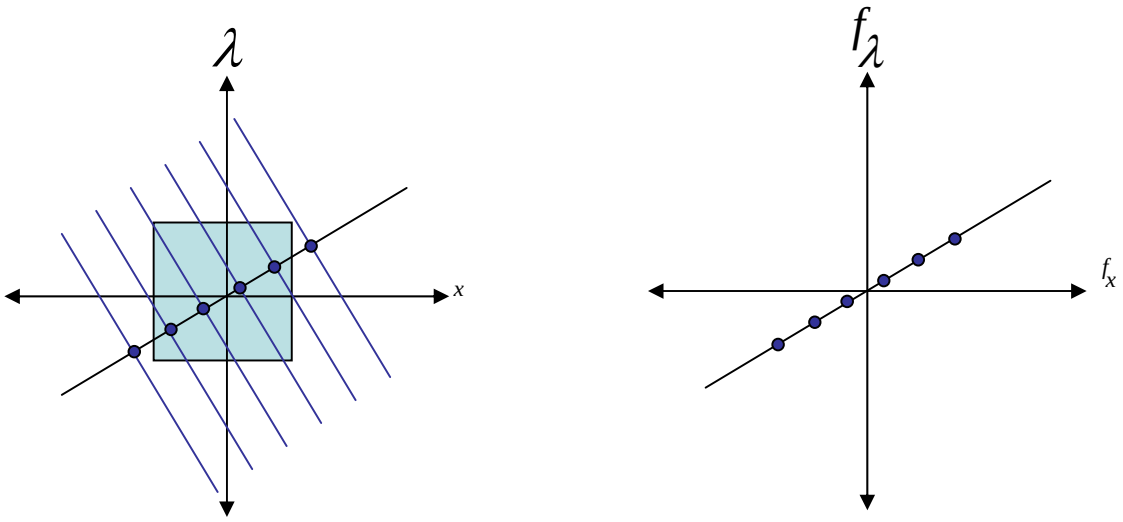

Figure 2-2 Projection in spatial domain and line integral in Fourier domain

The Austrian mathematician Radon showed that a higher dimensional function can be re-constructed from a set of lower-dimensional integrals of this function[26]. This is the fundamental theory of the Computer-Tomography Imaging Spectrometer: by projecting the three dimensional data cube onto a two-dimensional detector and properly introducing the spectral distortion, the entire data cube can be reconstructed from the collected two dimensional images.

The CTIS benefits from increased optical throughput compared to the push-broom imaging spectrometers, because the entire two-dimensional image is sent through the imaging system with no absorption or wasted photons. Furthermore, since multiple projections can be executed at the same time, scanning is not necessary and the data can be collected at a faster rate. This allows spectroscopic imaging of rapidly changing scenes.

However, in order to record the laterally shifted images, this technique requires the detector to be significantly larger than what is necessary in other techniques. Furthermore, the spectral and spatial resolutions both depend on the number of projections employed.

2.2. Detection resolution issue

2.2.1. Frequency domain analysis

As described in the previous section, the three-dimensional information cube is projected onto a two-dimensional detector using specialized optics. The Fourier transform of this recorded two-dimensional intensity distribution generates a plane in the three-dimensional frequency domain. A vector normal to this plane is parallel to the

projection angle in the three-dimensional spatial/spectral domain. By filling the three-dimensional frequency domain information cube with multiple projections as shown in figure 2-3, the original three-dimensional information cube can be recovered by inverse Fourier transformation.

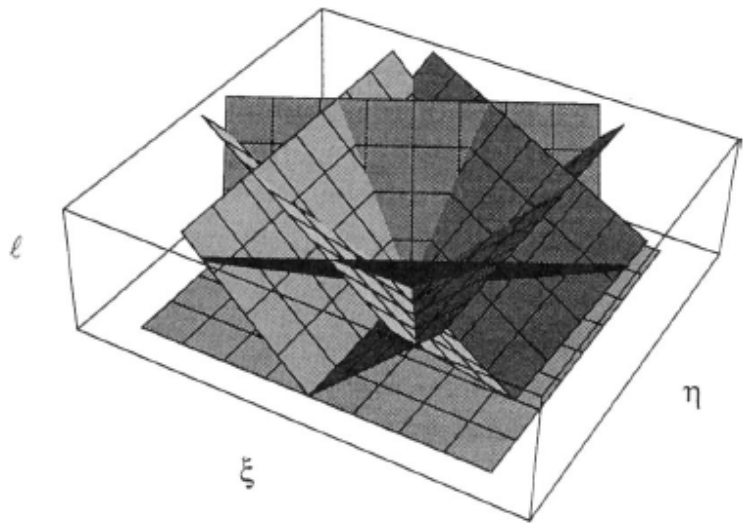

Figure 2-3, the three-dimensional information cube in frequency domain filled with projections in spatial domain (M.Descour, 1995), where η and ξ are spatial frequency unite and ℓ is spectral frequency unite

The finite detector size and finite dispersion limit the maximum projection angle that can be utilized. So in the frequency domain this leads to a missing data zone where information cannot be recovered (see figure 2-4). Because of this missing data zone, a unique reconstruction of the object cube is impossible in theory. Since the missing data zone is mostly concentrated in the low spatial frequency and high spectral frequency area, the high resolution reconstruction is still achievable for those objects with high spatial

intensity variation and low spectral intensity variation. This makes the CTIS technique spatial- frequency dependent, while other scanning methods are not subject to this issue.

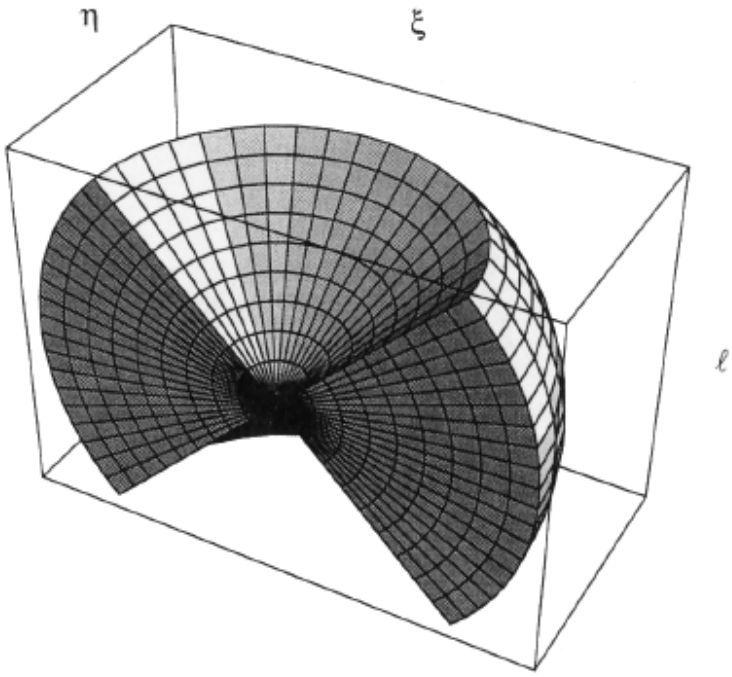

Figure 2-4 The useful data zone in the frequency domain (M.Descour, 1995)

Since the spectral information is multiplexed onto the spatial information by projections, the retrieved maximum spectral resolution can be estimated by considering the spatial frequency distribution. The higher the spatial frequency, the more spectral information can be included in the useful data zone and the higher spectral resolution can be achieved.

For example, if the object has a uniform spatial intensity distribution in every spectral band, the Fourier transform of the spatial intensity distribution generates a delta

function at the origin along the spatial frequency axis in the frequency domain. No matter how the spectral frequency data distribute, all the data are located in the missing data zone (on f_λ axis), as shown in figure 2-5 (assuming that a two dimensional information (x, λ) is analyzed here).

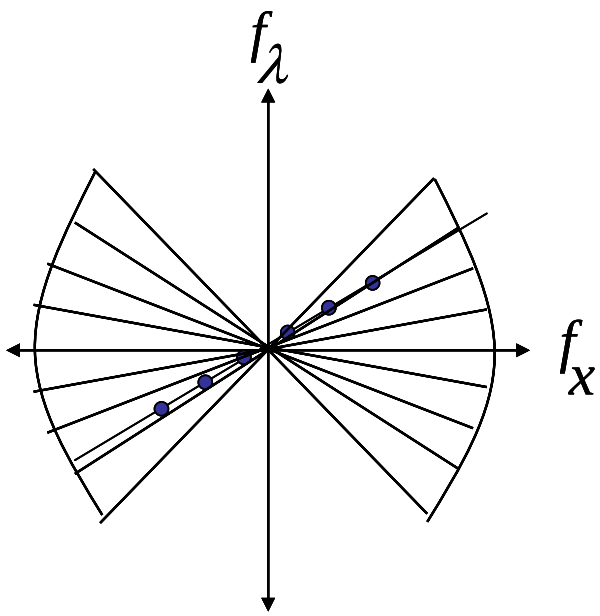

Figure 2-5 Useful and missing data zone in frequency domain

A field stop can be used in the optical system to limit the area of interest in the object space. Mathematically, this is equivalent to multiplying the object by a rectangular function $rect(x/a, y/a)$, where ***a*** is the dimension of the field of interest, and the ***rect*** function is defined as $rect(x) = \begin{cases} 0 & if\ |x| > 1/2 \\ 1/2 & if\ |x| = 1/2 \\ 1 & if\ |x| < 1/2 \end{cases}$. The Fourier transform of this new spatial intensity distribution results in a $sinc(f_x, f_y)$ function, where this function is

defined as $sin\,c(x) = sin(\pi x)/\pi x$. This ***sinc*** function occurs along the spatial frequency axis, indicating that high spatial frequency components are introduced into the object by the sharp edge of the field stop. Correspondingly the object's frequency information is shifted into the useful data zone. The smaller of the field stop is, the more information will be shifted into the useful data zone for information retrieval. This is the reason why a field stop is essential for the CTIS detection. This also suggests that, by spatially modulating the object intensity distribution at the field stop, the hyper-spectral information can be shifted from the missing data zone to the useful data zone in the frequency domain. This can be realized straightforwardly by adding a binary amplitude mask on the field stop to modulate the spatial frequency.

2.2.2. Sampling issues

Projection methods provide a method to measure the information contained in the useful data zone. In our case, a projection can be considered as a rule under which the spectral and spatial intensity is multiplexed onto the detector plane. Without the loss of generality, a two-dimensional object base (x, λ) is employed for analysis.

For the simplest case, let us consider one spatial point containing a specific spectrum across an infinite continuous range. The intensity distribution in the two-dimensional frequency domain is the multiplication of a uniform line along $\boldsymbol{f_x}$ (Fourier transform of the single spatial point) and the Fourier transform of the spectral information. If the spectral intensity is uniformly distributed, then the Fourier transform will only generate a point at the origin of $\boldsymbol{f_\lambda}$. So the frequency domain intensity distribution of this

particular object will be a uniform distribution along f_x axis only, as shown in figure 2-6(a).

The projection along the spectral axis will only generate a single point on the detector plane (figure 2-1 (a)), assuming the detector has an infinitely large size and an infinitely small pixel size. The Fourier transform of this single point will be a uniform intensity distribution along f_x axis without carrying any spectral information. So this projection readout will only carry the spatial intensity distribution information.

Any other projection with an arbitrary angle to the spectral axis will cause a uniform intensity distribution along a line on the detector plane. By carrying out the Fourier transform along this data line, the frequency information will be a point in the origin of f_λ axis. This single point reveals the continuous uniform spectral information. So by combining the two projection outputs together, the overall two-dimensional information can be reconstructed correctly.

With a finite detector extent and a finite detector pixel size, the projection data will be sampled by a series of *rect* functions. Correspondingly, a *sinc* function is convoluted onto the Fourier transform of the collected detector output. This will not affect on the frequency distribution along f_x axis for this simple object, but will broaden the single point along the projection direction, as shown in figure 2-6 (b). The parameters of the *sinc* function are determined by the detector pixel size and the projection, so in return the spectral resolution of this detection process can be derived from this *sinc* function. This forms the foundation of the "Push-broom imaging spectrometer", where

only one spatial point is always assumed along the projection direction and spectral resolution is directly calculated by the dispersion and detector pixel size.

If the spectral intensity distribution is not uniform, the frequency domain intensity distribution can be represented as shown in figure 2-7 (a). Again, a projection will introduce a data line cutting the frequency intensity distribution. The cross section is perpendicular to the projection direction (figure 2-1 (b)). This cross section essentially contributes a data point for every spatial frequency (figure 2-7 (b)). In order to retrieve the spectral information at any spatial frequency, multiple data points are required as dictated by the sampling theory[27, 28]. This is the reason why multiple projections are necessary for CTIS detection. Although more spatial points will complicate the frequency domain intensity distribution, the overall detection scheme always follows the same rule as described above.

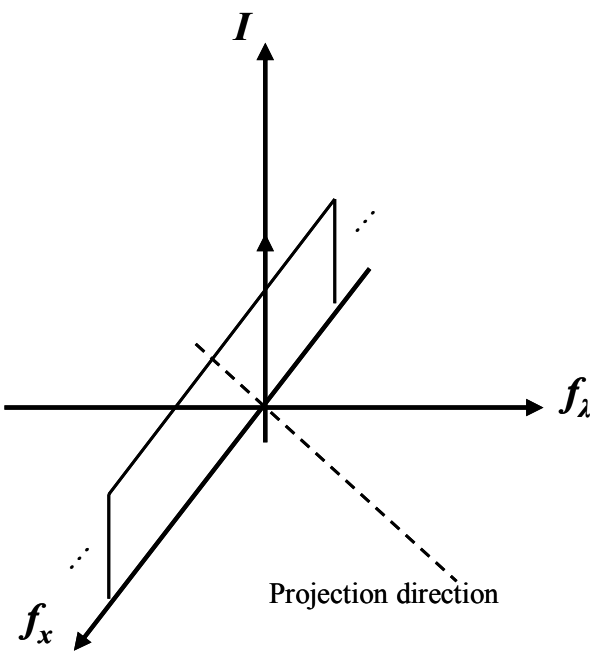

(a)

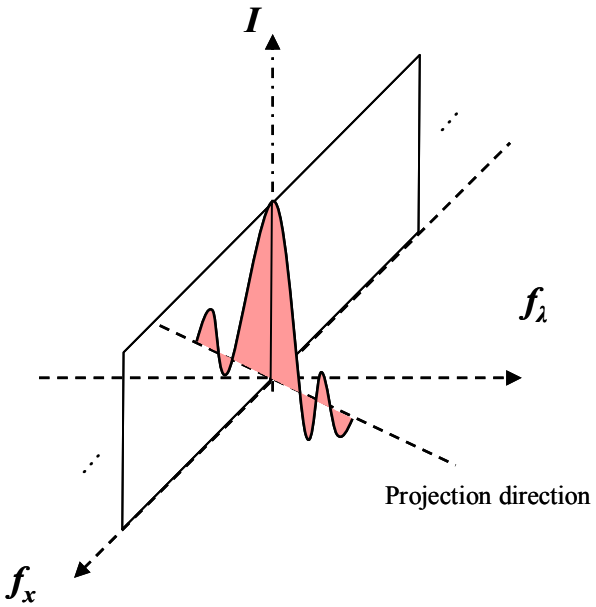

(b)

Figure 2-6 Projections contribution in frequency domain for a simple case

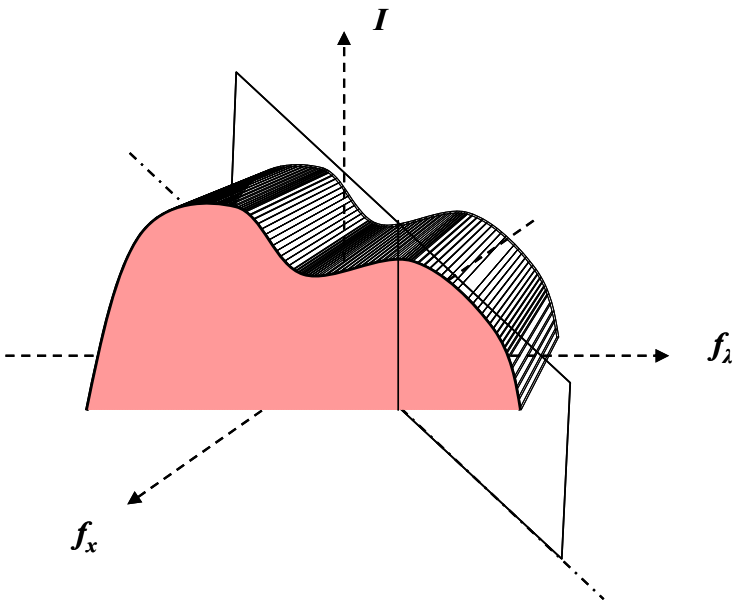

(a)

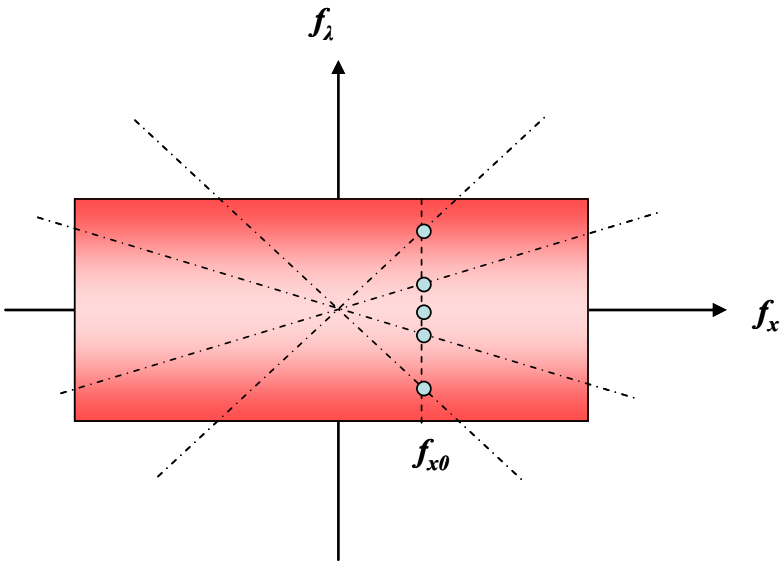

(b)

Figure 2-7 Projection contributions in frequency domain for a complicated case: (a) three-dimensional view, (b) two-dimensional top view

3. Imaging reconstruction

One output of a Computer-Tomography Imaging Spectrometer (CTIS) is a projection of the continuous three-dimensional (x,y,λ) information onto a two-dimensional plane by using dispersive elements to multiplex the spectral information into the spatial plane. The spectrally distorted images make themselves unique from each other by experiencing dispersion associated with different azimuthal directions (around the wavelength axis) or the vertical angle (away from the wavelength axis) as shown in figure 3-1. Every image carries all the three-dimensional information of the hyper-spectral object.

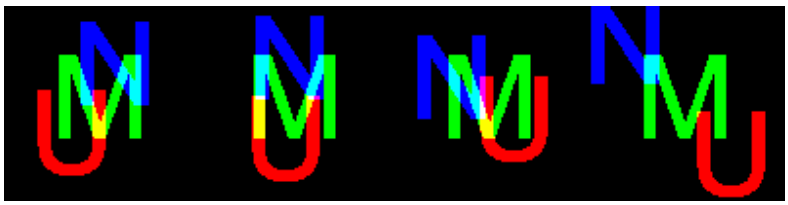

(a) (b) (c) (d)

Figure 3-1 Different type of dispersion for a hyper-spectral object: (a), (b) and (c) are projections along different azimuthal directions, (c) and (d) are projections along different vertical angle

According to the central-slice theorem[29], the two-dimensional Fourier transform of every image represents a plane in the three-dimensional frequency domain, and the plane's normal direction is uniquely determined by the azimuthal projection direction and vertical projection angle. Therefore, multiple spectral images give rise to samples in the

three-dimensional frequency domain. This information sampling method provides enough information for the three-dimensional information reconstruction.

Traditional hyper-spectral information reconstruction methods are reviewed in the first section. A simple algorithm generated for this project is described in second section. This algorithm was tested with a multiple-spectral object and a hyper-spectral object respectively as shown in the end of the chapter.

3.1. Traditional hyper-spectral information retrieval methods

Recovery of a three-dimensional distribution from a series of two-dimensional projections is known as the x-ray transform[30], which is extensively applied in the area of traditional medical computer tomography[31, 32, 33]. For any optical imaging system, the transfer function can be defined as an M by N matrix $\boldsymbol{\varphi}$, which operates on the object vector $\boldsymbol{f}$ and produces the image vector $\boldsymbol{g}$, as described in equation 3-1.

$$g = \varphi f + n \qquad (3\text{-}1)$$

where $\boldsymbol{n}$ is the additional system noise. In the CTIS system, the individual transfer function $\boldsymbol{\varphi}$ associated with every projection can be determined by calibrating the system with a spatial point object with multiple-spectral or hyper-spectral values. The additional system noise $\boldsymbol{n}$ represents the adjacent spatial points' spectral-spatial confusion caused by the projection process.

The Expectation-Maximum likelihood theory[34] is applied to solve mixed information situations. Expectation normally represents the process of guessing the system transfer function φ; maximum likelihood process is a popular statistical method to

calculate the best way to fit the mathematical model (equation 3-1) to some mixed information data.

By following the derivation of Myung, I.J., the probability density function f_θ is described as $f_\theta(x_1, x_2 \ldots x_n|\theta)$ associated with the observed n-value sample $(x_1, x_2 \ldots x_n)$, where θ is an unknown value. The likelihood function can be defined as

$$L(\theta) = f_\theta(x_1, \cdots, x_n|\theta) \tag{3-2}$$

The method of maximum likelihood estimates θ by finding the value of θ that maximizes L(θ). It is commonly assumed that the data drawn from a particular distribution are independent and identically distributed. This considerably simplifies the problem because the likelihood can then be written as a product of n univariate probability densities:

$$L(\theta) = \prod_{i=1}^{n} f_\theta(x_i|\theta) \tag{3-3}$$

Since maxima are not affected by monotonic transformations, one can take the logarithm of this expression and have:

$$L^*(\theta) = \sum_{i=1}^{n} \log f_\theta(x_i \mid \theta) \tag{3-4}$$

The maximum of this expression can then be calculated numerically with various optimization algorithms[35]. An algorithm based on the Maximum-likelihood theory was developed for CTIS detection in University of Arizona[36] and applied in many hyper-spectral detection studies.

3.2. Simplified reconstruction algorithm

The primary objective of this project is to develop a miniature CTIS sensor design. Therefore, a simple algorithm with flexibility to handle different simulation tasks is required.

For CTIS detection, an intensity distribution is sampled by the digitized camera pixels on the image plane. Without loss of generality, let us assume a specific projection in the two-dimensional (x, λ) domain. Each camera pixel records the intensity combination from different spatial points, described by the following equation:

$$I_{image}(x_n) = I_{object}(x_1, \lambda_n) + I_{object}(x_2, \lambda_{n-1}) + \ldots + I_{object}(x_m, \lambda_{m-n}) \qquad (3\text{-}5)$$

where n and m represent the index of the pixel position and spectral bands, respectively. The number of pixels with nonzero output corresponds to the number of linear equations we can generate, assuming no system background noise is involved. So the ability to solve individual object points' spectral information is linearly dependent on the number of camera pixels with nonzero readout. For the extreme scenario where there is only one spatial point in the object plane, the spectral information can be directly read out because the number of unknowns (intensities of spectral bands) is equal to the number of pixels with nonzero readout.

If there are n spatial points with m spectral bins, there are a total of n x m unknowns, and at least n x m linear equations are required to solve the problem. This leads to the relationship between the desired system resolution and the number of projections required. A system space points and spectral bandwidth product can be estimated by knowing the number of spatial points and spectral bands. Since one

projection can provide at least $n+(m-1)$ linear equations by shifting one spectral band per pixel, the minimum number of the projections required to resolve the space/spectral bandwidth product is

$$m \cdot n/(n+(m-1)) \qquad (3\text{-}6)$$

The projections in opposite directions may introduce some dependent equations, which can be easily demonstrated by using an example of 3 spatial points with 3 spectral bands. So in order to tolerance those dependent equations, normally the number of projections employed is larger than the predicted numbers required by equation 3-6.

There is another way to view the linear equations that describe this process. If the object has a high spatial frequency (spatial points' intensities vary over the FOV), then a projection would generate a unique intensity distribution on the detector plane. Since the calibration process can precisely predict the position of any spectral band from any spatial point on the detector plane for any projection, the corresponding intensity distribution can be determined accurately for any projection as long as the object hyper-spectral information is known. Therefore, we can always guess a three-dimensional object hyper-spectral information distribution and generate the corresponding intensity distribution on the detector plane for a projection. By comparing the simulated output and true detector output, an error matrix can be generated in the imaging plane detector pixel based scale. Since, for any imaging plane pixel scale, we know how much intensity is contributed by a particular spectral bin of a particular spatial point in the object plane by calibrating the projection, the error corresponding to this imaging plane pixel can be accurately subtracted from that particular spectral bin based on the weight of contribution;

consequently a new object three-dimensional information matrix can be generated. By running this calculation through different projections, the error matrix can be reduced and the estimate of the object three-dimensional data cube will be uniquely driven to the true value.

Obviously the non-dispersed image is one of the best candidates for the initial estimate of the three-dimensional hyper-spectral object. Since there is no spectral information, all spectral bins are set to the same intensity distribution. A simple hyper-spectral information reconstruction algorithm is developed based on this linear relationship and the concept of error redistribution based on the contribution weight.

This algorithm depends highly on the number of the independent equations and the object's spatial intensity distribution. For example, if all spatial points in the FOV have the same intensity value within every spectral bin, but the intensity varies from spectral bin to bin, then the imaging plane pixels near the center of the FOV will always have same readout no matter how the three-dimensional information is projected. Independent equations only come from the far edge of the distorted image along the projection direction. This also agrees with the frequency domain analysis developed in chapter two, i.e., the useful information in CTIS detection always comes from the high spatial frequency part of the image.

The first advantage of the algorithm presented here is that it can be easily modified and used for different objects and projections. Second, for an object with a small space/spectral bandwidth product, this algorithm is more computationally efficient

than the Maximum- likelihood algorithm because it utilizes simple linear calculation rather than a complicated statistical analysis.

3.3. Algorithm performance demonstration

The algorithm was programmed in Matlab and tested with various multiple-spectral and hyper-spectral information databases. After being validated, the algorithm was used to elucidate the CTIS theory described in Chapter 2 and to demonstrate the system performance (shown in Chapter 6).

3.3.1. A simple multiple-spectral object test

A simple multiple-spectral object was generated with the software "Photoshop". The RBG colors were used to simulate three spectral bins. A letter "U" was assigned to the red channel, a letter "M" to the green channel and a letter "N" to the blue channel as shown in figure 3-1 (a) ~ (c). Every color represents a discrete spectral band. In every spectral band, the pattern pixels' value was set to 255. These three spectral channels were added together without shift to generate a pattern and simulate the zero dispersion projection output (figure 3-1 (d)). This non-distorted pattern was used to generate the initial guess. Several projections were simulated by shifting the red channel and blue channel relative to green channel to generate the different dispersions in the azimuthal direction as shown in figure 3-2.

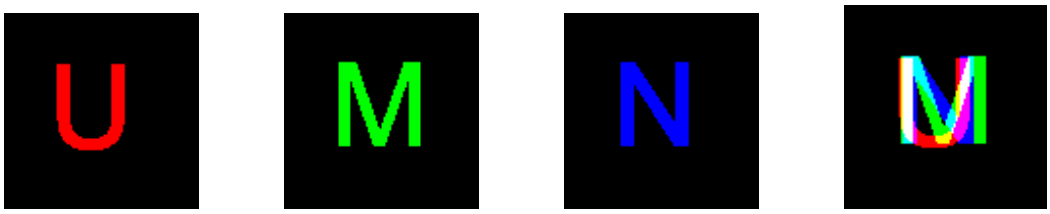

(a) (b) (c) (d)

Figure 3-1 Computer generated multiple-spectral object and non-dispersed image

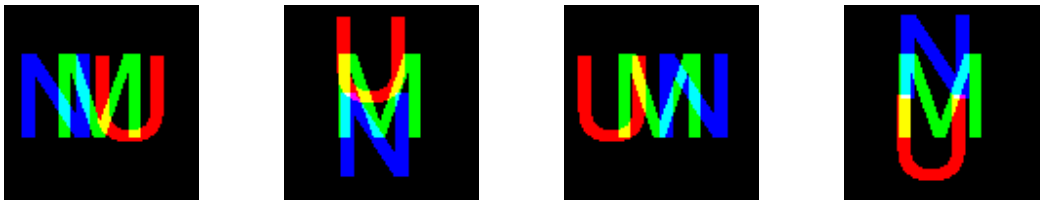

(a) (b) (c) (d)

Figure 3-2 Computer generated four projections along different azimuthal directions

(a)

(b)

Figure 3-3 Reconstructed multiple spectral information: (a) based on three projections, (b) based on four projections

The reconstruction was first tested with only three projections. After 138 iterations, the intensity error matrix RMS value was reduced to 0.9984 from 10^3, and the reconstructed three spectral bands are shown in figure 3-3 (a). Clearly one can recognize some errors in every spectral band. In a second reconstruction, all four projections were used to recalculate the multiple-spectral information. After 5 iterations, the intensity error matrix RMS value was reduced to 0.1862, and no obvious noise can be observed in the reconstructed multiple-spectral information in figure 3-3 (b).

This initial test based on a simple multiple-spectral object validated the proposed algorithm, and demonstrated the rule of thumb for the CTIS design: larger numbers of projections lead to increased accuracy.

3.3.2. AVIRIS data test

A more realistic hyper-spectral information database, "NASA AVIRIS database", was employed for the algorithm validation. AVIRIS data were collected from a proven and calibrated airborne instrument designed to collect Earth Remote Sensing data. The data base includes 224 contiguous spectral channels with wavelengths from 400 to 2500 nanometers. In the test, 39 spectral channels were utilized. Various projections were generated by shifting a spectral bin one spatial point in different azimuthal directions. One of the projections was selected randomly to generate the initial estimate of the three-dimensional object; the spatial intensity distribution of every spectral band was set to be this projection's intensity distribution.

In the first reconstruction, an object with 2 by 2 spatial points was tested. Two projections were used and after 990 calculation iterations, the hyper-spectral information of this 2x2 spatial object was reconstructed almost perfectly as shown in figure 3-4 (a). The same three-dimensional hyper-spectral information was retrieved successfully after 107 iterations with 3 projections as shown in figure 3-4 (b). This experiment validates the developed algorithm for hyper-spectral information reconstruction.

An object with 10 by 10 spatial points was tested with 2 projections, 4 projections and 8 projections, respectively. A fixed spatial point's reconstructed spectral information was displayed in figure 3-5 (a), (b) and (c), respectively. The blue line is the true spectral intensity distribution and the red line is the retrieved spectral information. Clearly the error reduces as the number of the projections increases.

The last experiment was carried out with 8 projections but the number of the spatial points was increased from 10 by 10 to 20 by 20 and 40 by 40, respectively. The same spatial point's reconstructed spectral information was shown in figure 3-6 (a), (b) and (c), respectively. Again, as discussed in the previous section, the reconstruction error increases with the size of the space/spectral bandwidth product. This algorithm is more efficient for the hyper-spectral object with a small space/spectral bandwidth product.

The algorithm is proved to be valid for the general hyper-spectral information reconstruction and the operation is very simple. Nevertheless, it is efficient only for an object with a small space/spectral band width product, and furthermore it is very sensitive to system noise. Keeping these limitations in mind, we will apply this algorithm to evaluate the CTIS theory and sensor system performance in the subsequent chapters.

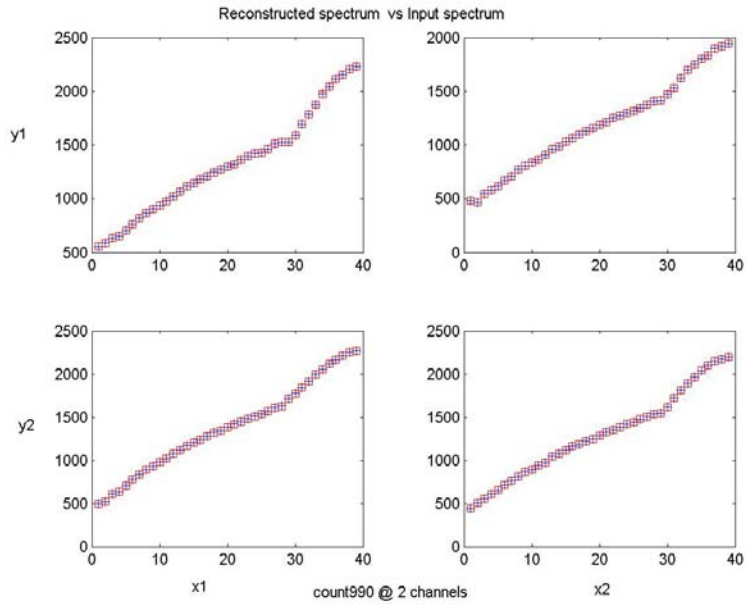

(a)

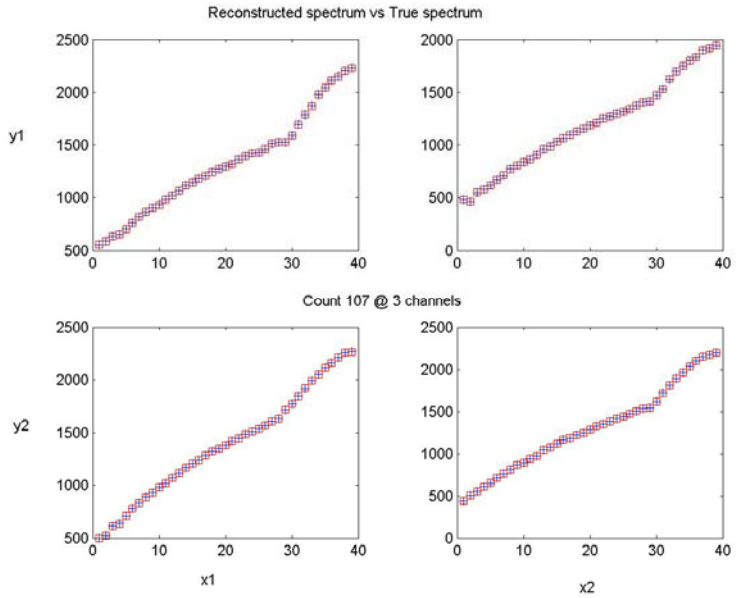

(b)

Figure 3-4 hyper-spectral information reconstruction with 2x2 spatial points and 39 spectral bins: (a) with 2 projections, (b) with 3 projections

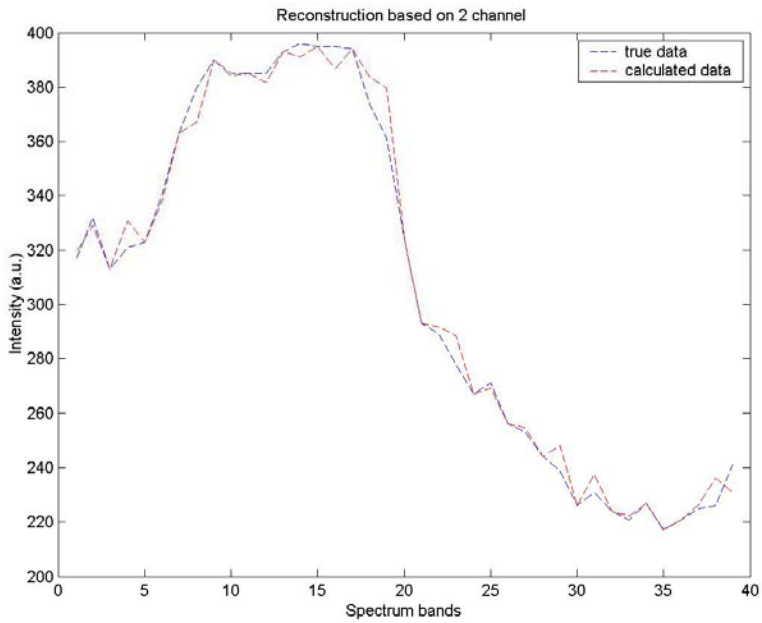
Reconstruction based on 2 channel
true data
calculated data
Intensity (a.u.)
Spectrum bands
400
380
360
340
320
300
280
260
240
220
200
0
5
10
15
20
25
30
35
40

(a)

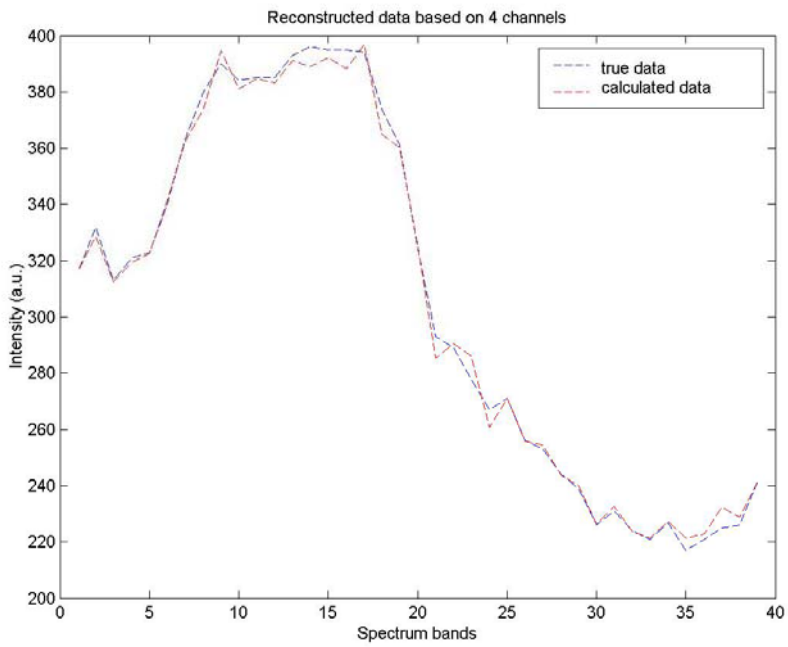
Reconstructed data based on 4 channels
true data
calculated data
Intensity (a.u.)
Spectrum bands
400
380
360
340
320
300
280
260
240
220
200
0
5
10
15
20
25
30
35
40

(b)

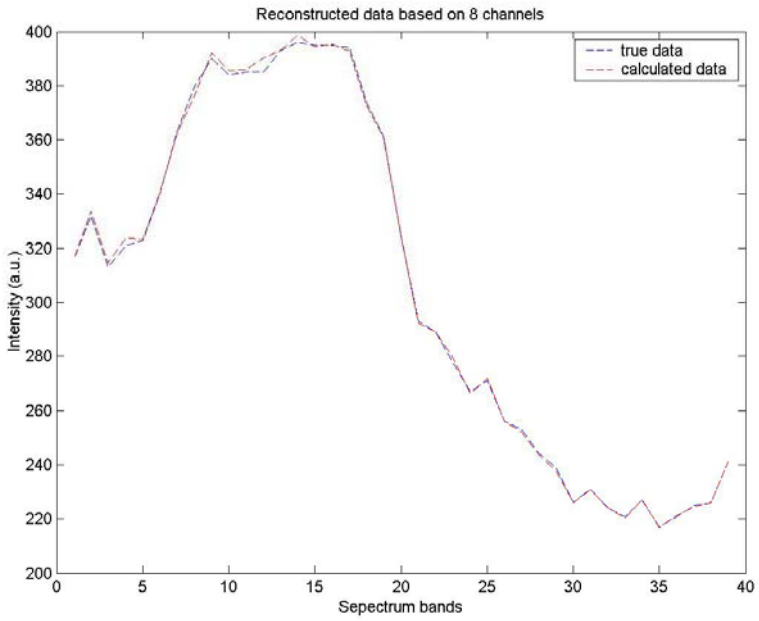

(c)

Figure 3-5 Estimate of the spectral content from one point in a 10x10 point image: (a) 2 projections, (b) 4 projections, (c) 8 projections

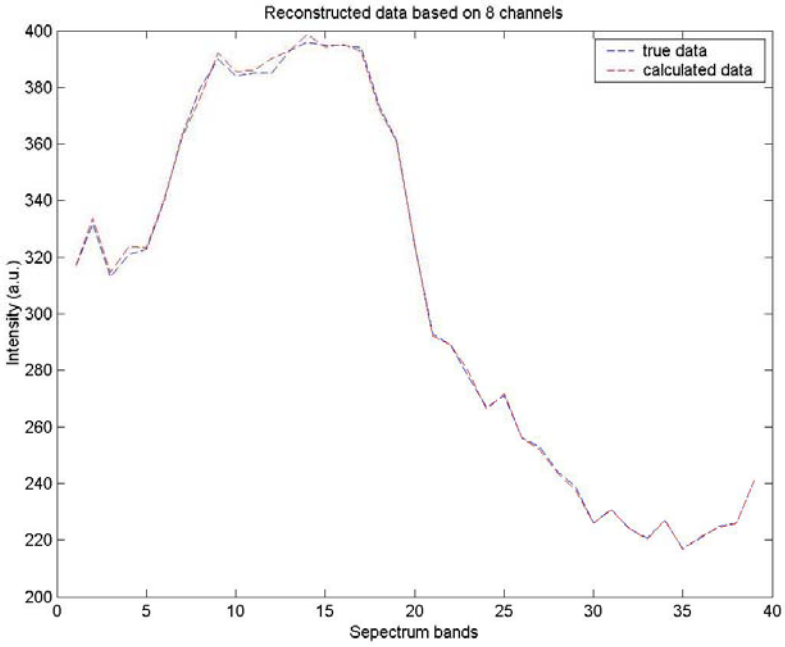
Reconstructed data based on 8 channels
true data
calculated data
Intensity (a.u.)
Sepectrum bands
400
380
360
340
320
300
280
260
240
220
200
0
5
10
15
20
25
30
35
40

(a)

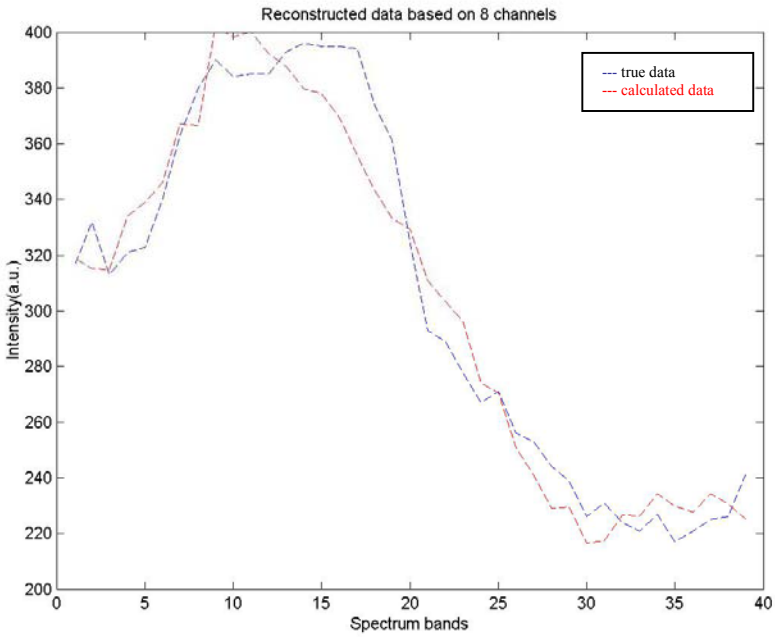
Reconstructed data based on 8 channels
true data
calculated data
Intensity(a.u.)
Spectrum bands
400
380
360
340
320
300
280
260
240
220
200
0
5
10
15
20
25
30
35
40

(b)

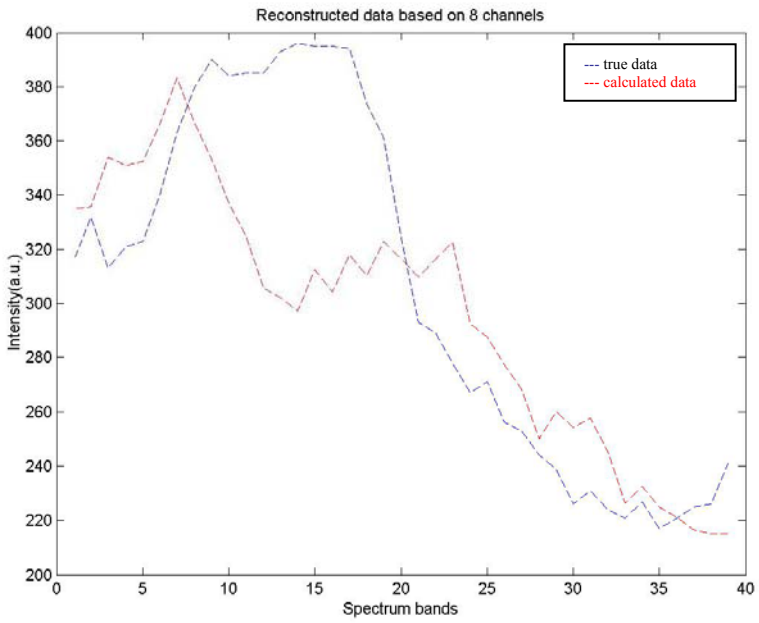

(c)

Figure 3-6 Estimate of the spectral content from one point in the object using eight projections: (a) 10 by 10 spatial points, (b) 20 by 20 spatial points and (c) 40 by 40 spatial points

4. System design

The primary objective of this project is to develop a design methodology for a miniature CTIS sensor. A compact system architecture was chosen first, then individual optical elements were optimized to decrease the sensor size without compromising performance quality significantly. A computer model was generated, and system performance was evaluated.

4.1. System architecture design

The key to the CTIS detection scheme is the projection of an object's three-dimensional information (x, y, λ) onto a two-dimensional plane (x, y), by multiplexing the spectral information into the spatial information. Multiple spectrally distorted images need to be generated to retrieve the hyper-spectral information. The main elements for any CTIS detection system include a field stop to isolate a particular area of object space, and a dispersive imaging system to record the intensity. The basic architecture of a CTIS sensor can be drawn as figure 4-1.

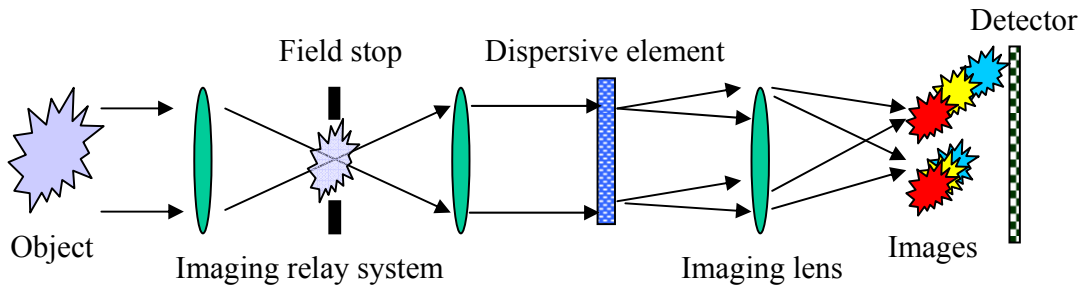

Figure 4-1 The fundamental architecture of a CTIS sensor

An imaging relay system introduces a field stop and collimates the light passed by the field stop. A dispersive element multiplexes the spectral information onto the spatial information and a final lens system images this intensity distribution onto the detector. Hence a CTIS system essentially combines a traditional two-dimensional imager with a dispersive element.

4.1.1. Coupled information channel design

Multiple images with different spectral dispersion are required for the hyper-spectral information reconstruction, as discussed in Chapter 3. The classic implementation is using multiple gratings in an imaging system to generate multiple spectrally distorted images simultaneously, as shown in figure 4-1.

In order to achieve different amounts of dispersion, a grating should be designed to work with multiple diffraction orders, usually symmetric to the zero order. Multiple gratings can also be used in a single imaging system. Associated dispersion directions are separated by specific azimuthal angles around the imaging system optical axis. For example, in M.Descour's design[34], there are 2 gratings in an imaging system, each grating generates 5 diffraction orders (0th, ±1st and ±2nd). The dispersion directions are perpendicular to each other. So there are total 25 different spectrally distorted images generated in one imaging system.

We define optics that generates one spectrally dispersed image as one information channel. In this CTIS design, there is a single imaging system with multiple gratings. So

this single imaging system and the dispersive element are shared by all the information channels. This architecture is called a “coupled information channel” design.

The advantage of this design is only one imager is required and the aperture size can be maximized to achieve the best object side resolution. There are several disadvantages of this design. First, more complex dispersive elements, like computer generated hologram[37] or a combination of multiple gratings[34] need to be used. Second, because all diffraction orders (except the zero diffraction order) propagate at an angle with respect to the optical axis, the imaging system experiences larger aberrations. In order to improve system imaging quality, a more complex lens system is required as shown in M.Descour’s design (figure 4-2), which makes system miniaturization difficult. Another disadvantage for sensor miniaturization is that the collected photons are distributed across multiple information channels. Decreasing the sensor entrance pupil size will decrease the photon collection ability dramatically, and may result in a poor signal noise ratio for a given information channel.

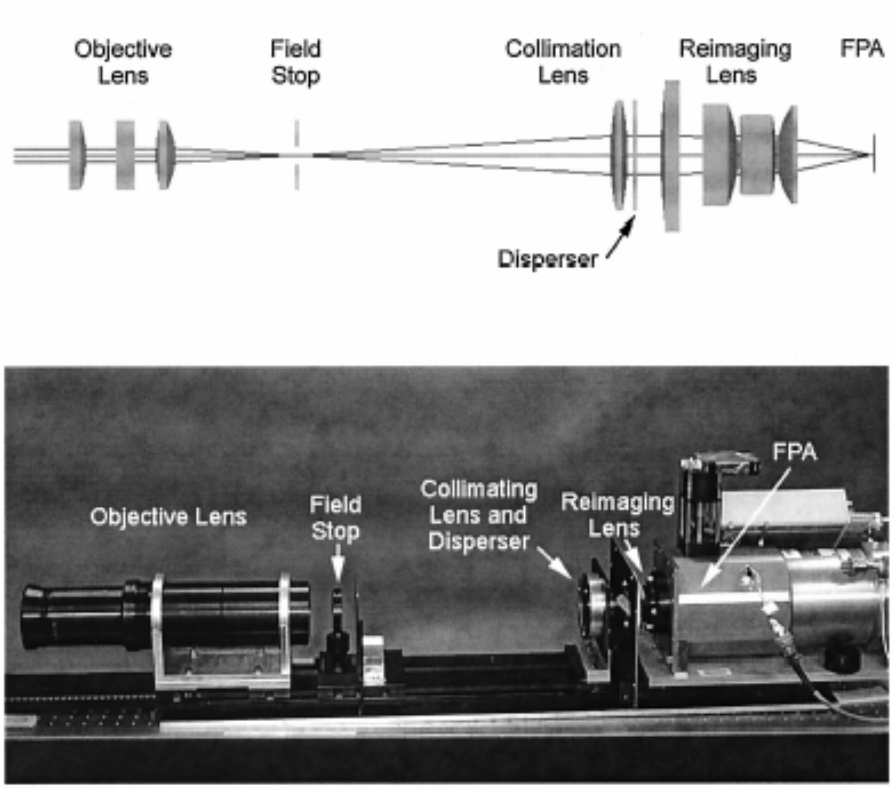

Figure 4-2, An implemented CTIS sensor in the "coupled information channel design" (M.Descour's design, 1995)

4.1.2. Independent information channel design

While the "coupled information channel design" utilizes one imager and a dispersive element to generate multiple spectrally distorted images, the "independent information channel design" is more suited to a sensor array structure. Multiple imaging systems are employed. The dispersive element in every imager generates a single spectrally dispersed image, with each individual imaging system essentially forming its

own information channel. These information channels are independent from each other since they do not share any optical elements.

The properties of this independent information channel design are complementary to the coupled information channel design. For example, suppose there are ***n*** information channels in each design, and in the array design every individual imager's aperture area is one $\boldsymbol{n}^{th}$ of the aperture area in the coupled information channels design. Hence every information channel in both designs has the same light flux and experiences the same signal noise ratio level. However, since each individual imager in the array structure has a smaller aperture size, the depth of this individual imager can be n times smaller than the coupled design, which can significantly reduce the sensor size.

Since only one dispersed image is involved in every information channel under the independent information channel design, the dispersed light may propagate near the optical axis to experience less aberration under a special optical design. The small imager size also results in potentially smaller aberrations[15]. So this imaging system can be much more compact than the coupled information channel design. Therefore, the independent information channel design is a better solution for our miniature hyperspectral sensor. As the penalty, when an individual imager's aperture area is decreased by ***n*** times, the object side resolution will also decrease by the square root of ***n***, though a large fore optics can be used to maintain the object side resolution as described in Chapter one.

4.2. Individual optical element optimization

The independent information channel design can result in a simple imaging system because of simplified aberration concerns. So a reduced number of lenses is required in every individual information channel: two lenses for a relay system and one lens as the final imager. Since this miniature imaging system is a combination of lenses in series, a cylinder gradient index rod lens was proposed for this design.

4.2.1. Gradient index lens theory

In general a Gradient index (GRIN) rod lens refractive index distribution has a parabolic refractive index profile (4-1) along the radius direction, and the partial derivative of n^2 with respect to z is zero[38]:

$$n^2(x) = \begin{cases} n^2(0)[1-(gx)^2 + h_4(gx)^4 + h_6(gx)^6 + ...], & x \le a \\ n_2^2, & x > a \end{cases} \tag{4-1}$$

$$\begin{aligned} \frac{dX_1}{dz} &= X_2 \\ \frac{dX_2}{dz} &= \frac{1}{n^2}(1+X_2^2)X_2 \frac{\partial}{\partial z}\left(\frac{1}{2}n^2\right) - \frac{1}{n^2}(1+X_2^2)\frac{\partial}{\partial x}\left(\frac{1}{2}n^2\right) \end{aligned} \tag{4-2}$$

where $X_1 = x;\ X_2 = dx/dz$.

By solving the ray equation in cylindrical coordinate (4-2) with a perturbation theory, an approximate solution is given as follows

$$x = x_i \cos(\Omega z) + \frac{x_i'}{\Omega}\sin(\Omega z)$$

where

$$\Omega / g = 1 - \frac{3}{4}(h_4 - \frac{2}{3})[(gx_i)^2 + x_i'^2] - \frac{3}{4}\left(h_4 - \frac{2}{3}\right)$$

$$\times[21(gx_i)^4 + 46(gx_i)^2 x_i'^2 + 17x_i'^4]/12 - [\frac{3}{4}\left(h_4 - \frac{2}{3}\right)]^2$$

$$\times[7(gx_i)^4 + 46(gx_i)^2 x_i'^2 + 23x_i'^4]/12 - \frac{15}{16}(h_6 - \frac{17}{45})[(gx_i)^2 + x_i'^2]^2 \quad (4\text{-}3)$$

For $h_4 = \frac{2}{3}$, $h_6 = -\frac{17}{45}$, the pitch of each ray is independent of the incident condition. Since each ray is focused at the same point in a distributed index rod lens, this is an aberration-free condition for meridional rays.

The primary method for fabricating a distributed refractive index material is to diffuse metal ions in or out of a glass substrate. Electromigration is a technique where ions migrate with the help of an electric field. Since diffusion takes place at the same time, this process is also called field-assisted diffusion.

GRIN lenses are used to focus and collimate light within a variety of fiber optic components, along with a wide array of products that require either passive or active electrical components. Passive component manufacturers use GRIN lenses in wavelength division multiplexers (WDM)[39], optical switches[40], and attenuators[41]. In active components, GRIN lenses are used in fiber-to-detector and laser-to-fiber coupling[42]. GRIN lenses are well suited to coupling the output of diode lasers into optical fibers because they can achieve aberration correction without complex multi-

element systems or aspheric lenses and real images can be formed at the lens surface[43]. Therefore, GRIN lenses are an economic alternative to conventional lenses.

A quarter-pitch length corresponds to the lens' length with which the GRIN lens can focus the input parallel light into a spot at the back lens surface. A half-pitch lens will generate an inverted image at the back surface when an object is located at the front surface. A full-pitch lens will generate an erect image by doubling the half-pitch lens length, as shown in figure 4-3.

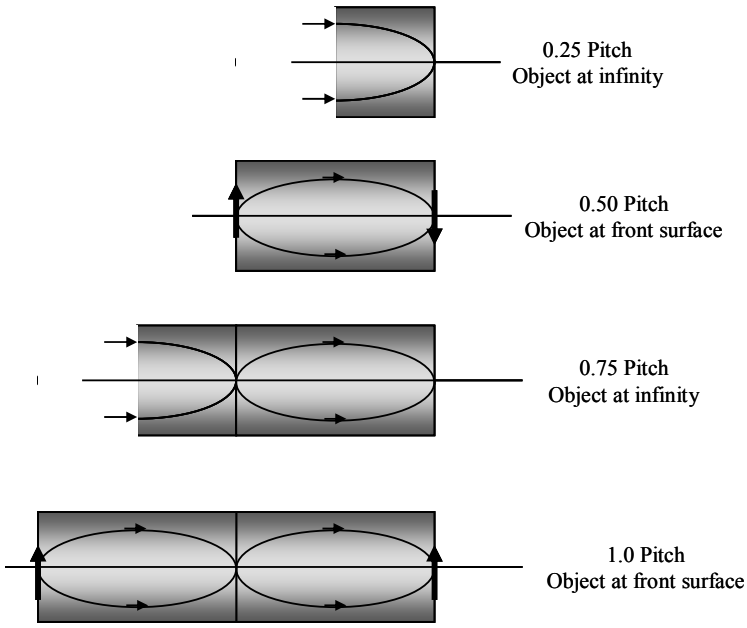

Figure 4-3 GRIN rod lens imaging functions

4.2.2. Dispersive element design and optimization

Since only a single diffraction order is required in any individual information channel, a blazed grating is the best choice for the dispersive element design, as its

trianglar shape can direct 100% of the input light into the desired diffraction order (at least in the scalar diffraction limit and at a single wavelength).

In order to minimize aberration, the light should be constrained near the optical axis of the imaging system. The grating normal must therefore be rotated by a specific angle to keep the input light and diffracted output light parallel to the imaging system optical axis. This angle is governed by the grating equation (4-4).

$$n_o \sin\theta_o - n_i \sin\theta_i = m\frac{\lambda}{d} \tag{4-4}$$

The GRIN lens' cylinder structure provides the particular advantage for this design. One end of a GRIN lens can be ground and polished to a specific wedge angle, resulting in a prismatic surface. By directly fabricating the grating onto this surface, a unique optical element is generated containing the functions of refraction, diffraction and GRIN imaging. The grating disperses the input light; the prismatic surface refracts light in the first grating order (at the central wavelength) back to optical axis and tilts light in the other diffraction orders towards the side wall of the GRIN rod. The GRIN lens then images the spectrally dispersed image onto the detector plane. By combining the grating onto the final imager, a very concise CTIS single information channel can be achieved with only 3 GRIN rod lenses.

A grating period should first be chosen according to the desired dispersion. Then the prismatic surface angle can be calculated based on the equation (4-4) to tilt the propagation angle of the reference wavelength light to propagate along the optical-axis. The last step is to blaze the grating into the best shape to maximize the diffraction

efficiency. The easiest way to optimize the grating profile is to trace the wave-front of the reference wavelength light. The in-phase condition should be satisfied as shown in figure 4-4. The mathematical equation corresponding to this wavefront analysis is listed in figure 4-4.

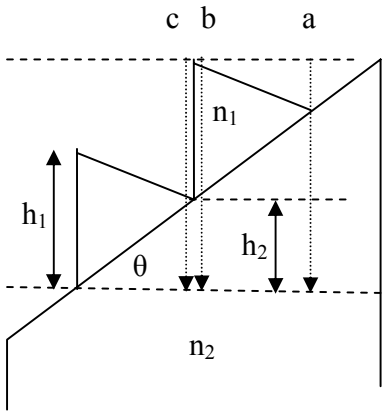

$$\left.\begin{aligned} h_1 n_1 &= (h_1 - h_2) + h_2 n_2 \\ h_1 n_1 + h_2 n_2 &= h_1 + h_2 n_2 + m\lambda \\ h_2 + h_1 n_1 + m\lambda &= h_1 n_1 + h_2 n_2 \end{aligned}\right\}$$

$$\Rightarrow \begin{cases} h_1(n_1 - 1) = h_2(n_2 - 1) \\ h_1(n_1 - 1) = m\lambda \end{cases}$$

Figure 4-4 Wavefront analysis and associated the mathematical equations

Notice that the grating normal does not overlap with the optical axis. The tilting position modifies the grating blazed condition. The direct impact is that the blazed grating modulation depth is decreased, and the grating surface is not perpendicular to the substrate any longer. Both effects can simplify the grating fabrication dramatically.

4.3. Final CTIS design

Once the fundamental system architecture is decided and individual optical elements are selected, the sensor system design can be carried out. In this project, the sensor works in the visible wavelength range, 400nm ~ 700nm, and the reference wavelength is 550nm. In order to design the smallest CTIS sensor, the smallest GRIN rod

lens commercially available was selected[44], (diameter is 250μm). The quarter-pitch length is 670μm.

4.3.1. Single information channel evaluation

The resolution of any type of optical imaging system can be limited by multiple factors, such as imperfections in the lenses or misalignment. However, there is a fundamental maximum to the resolution of any optical system given by diffraction. An optical system with sufficiently small aberration is dominated by diffraction effects and is said to be diffraction-limited. The criterion for diffraction-limited performance usually requires the wavefront error from an object point to its corresponding image point through any part of the pupil to be no more than ¼ wavelength.

The CodeV software was used to implement a computer model of the optical elements and predict the system performance. Since the GRIN rod lens was bought from a commercial vendor, the detailed refraction index distribution was not available. A parabolic profile was modeled as designed.

The imaging system was simulated as shown in figure 4-5 shows. Three GRIN rod lenses were cascaded in a row. The first two are quarter-pitch lenses, and the length of the 3rd lens is 150um shorter than quarter-pitch to introduce a 100μm gap between the lens back surface and the detector. The MTF function study is also shown in figure 4-6. The tangential and sagittal aberration was analyzed at different input angles as shown in figure 4-7, which indicates that if the FOV is limited to be $\pm 8^{o}$, this imaging system operates near the diffraction limit for all field points.

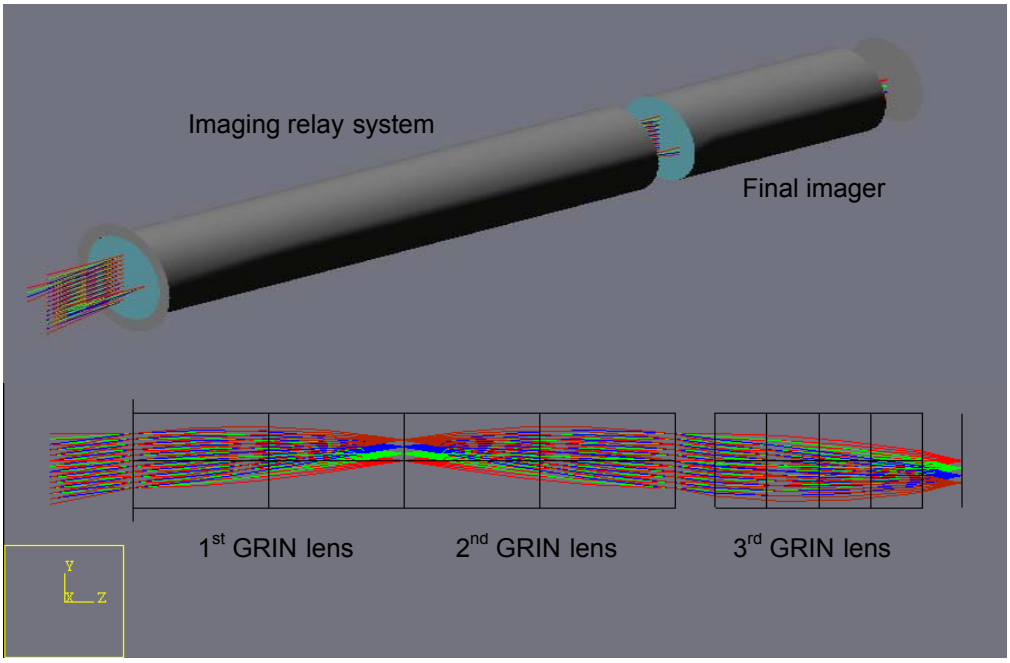

Figure 4-5 Independent information channel imaging system design

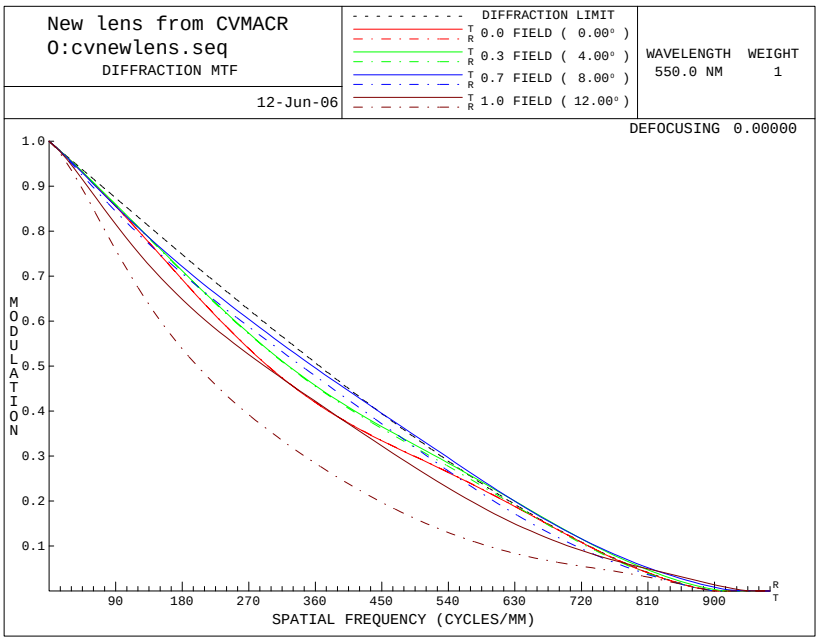

Figure 4-6 Imaging system MTF analysis

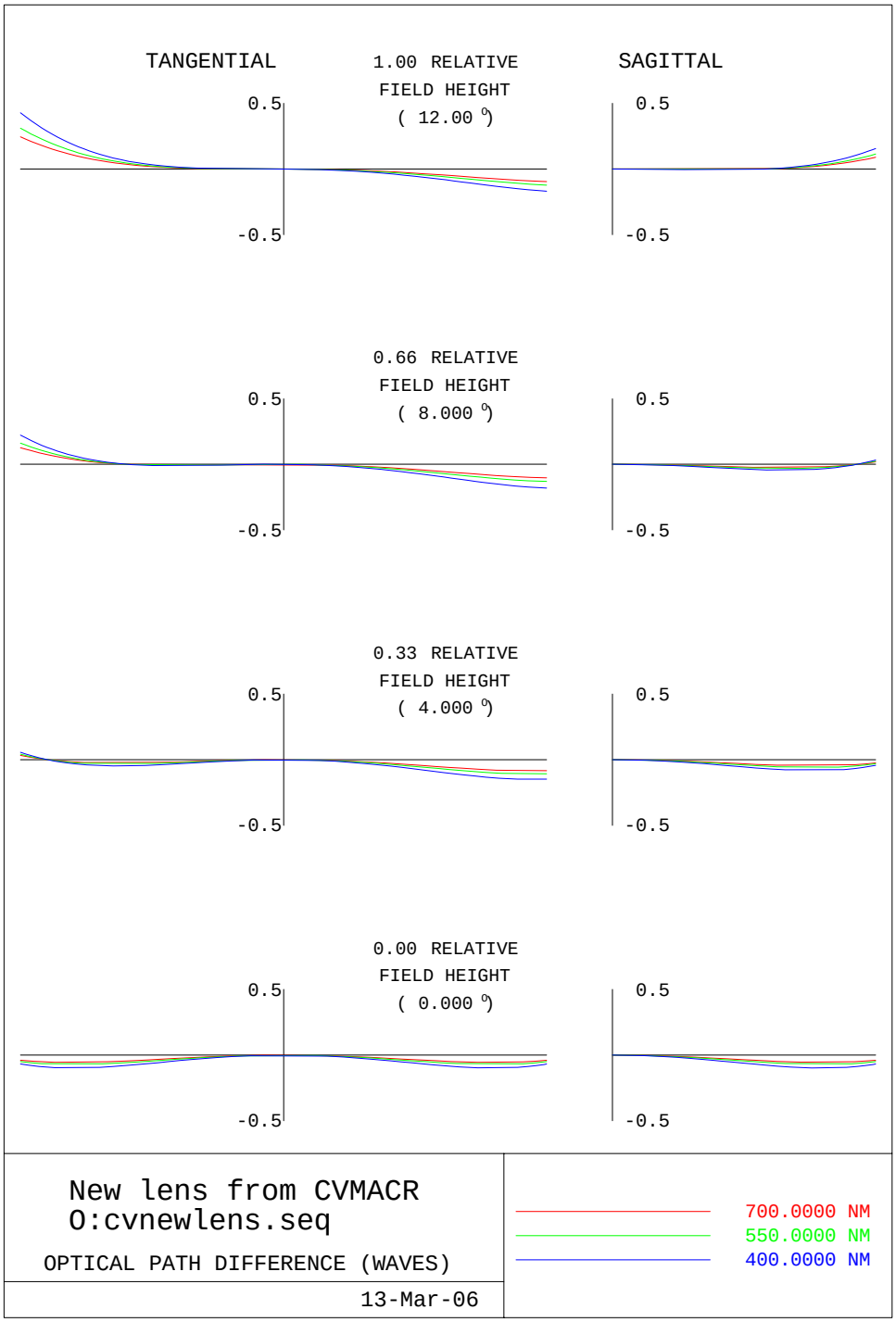

Figure 4-7 Optical path different analysis in wave scale

Once the FOV was chosen, the field stop's position and size can be calculated by the ray trace analysis. In our case, it is on the back surface of the first GRIN lens of the imaging relay system and the front surface of the second GRIN lens. The field stop's diameter is 36.55 μm to limit the $\pm 8^{o}$ FOV.

In this design, the CMOS detector was pre-selected with a 3.2 μm pixel size. Our CTIS sensor has an image side numerical aperture (NA) of 0.25 to match the CMOS detector's 15° input angle, which results in an image system entrance pupil diameter of 143.2μm. With an NA = 0.25, the point spread function (Airy disk diameter) is 2.7 μm at 550 nm, corresponding to an object side angular resolution of 0.27°.

The detector is placed directly behind the final GRIN lens. A GRIN rod lens' radius is 125μm, corresponding to an area of 62,500 μm^2 on the detector plane. With $\pm 8^{o}$ FOV, there are 30 resolvable points in the radius direction on the image plane. This corresponds to a useful detector area of 20,000μm^2. So only around one third of the detector pixels are truly utilized in this design as shown in figure 4-8. The blue square represents the camera area taken by a GRIN rod lens. The brown circle shows the area directly under the GRIN rod lens. Small circles inside of the brown circle correspond to the individual Airy disk imaged onto the camera plane.

The imaging system was designed and related parameters were calculated according to the previous simulation results. The next step of this study is the dispersive element design. The grating period of 2 μm was selected as a trade-off between the maximum spectral resolution and the highest diffraction efficiency. The smaller the grating period is, the larger the spectral dispersion that can be achieved. When the grating

period size approaches to the size of a wavelength of light, scalar diffraction theory is no longer accurate and a full vector solution to Maxwell's equations must be obtained. This solution generally shows that the grating will always diffract some light into unwanted orders even when the grating is perfectly blazed.

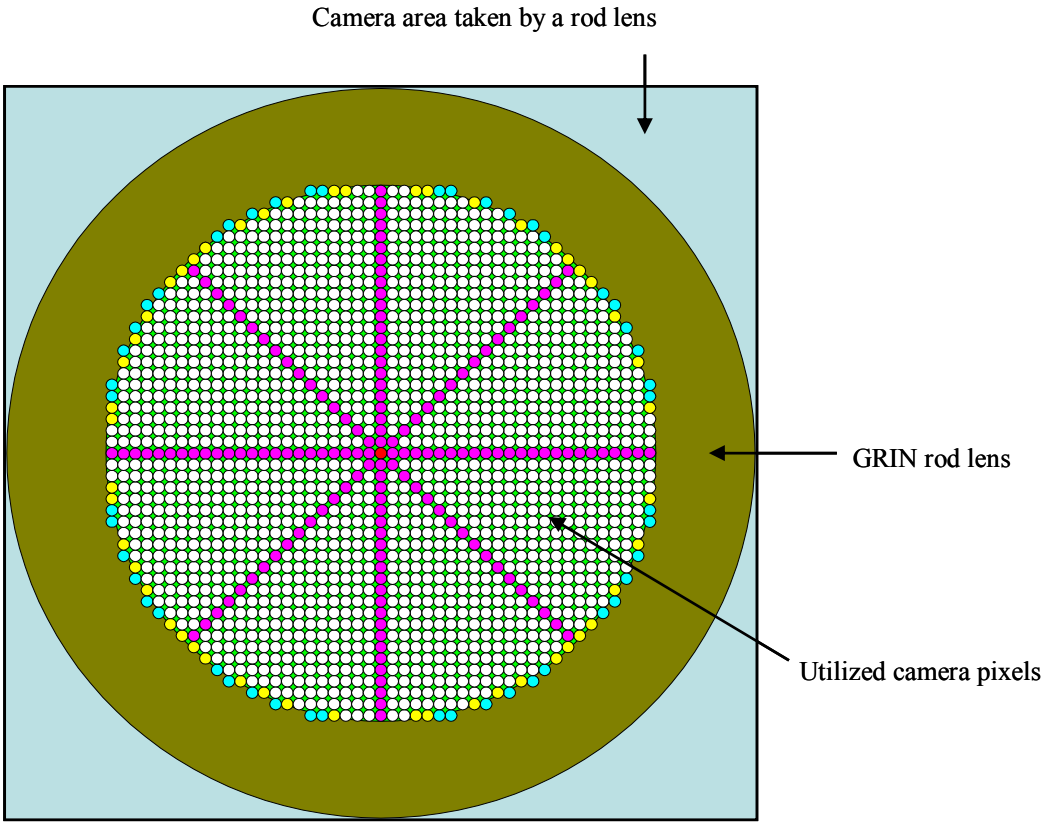

Figure 4-8 Camera efficiency diagram based on the utilized the camera pixels

The blazed grating profile and the tip angle of the prismatic surface of the 3rd GRIN rod lens can be quickly calculated based on the grating period, grating material refractive index and GRIN rod lens refractive index, either using equation 4-4 or

geometrically tracing the wavefront in figure 4-4. In the simulation we assumed that the grating material has the same refractive index as the GRIN rod lens. The optimized grating profile is shown in figure 4-9. The calculated tip angle of the prismatic surface is 65°.

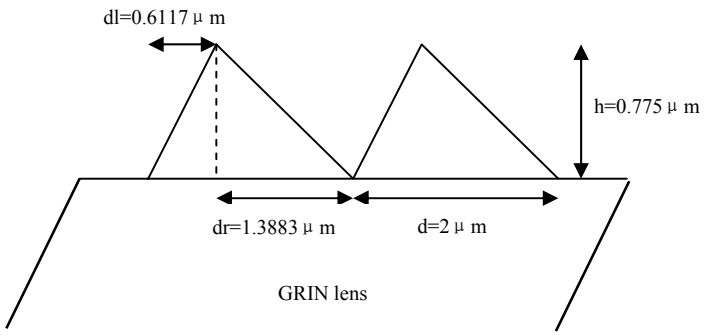

Figure 4-9 The optimized grating profile based on the wave front calculation

A software tool "R-Soft" based on the rigorous wave coupling theory[45] was used to simulate the grating effects. The efficiency of the first diffraction order is in the range of 65% ~ 70% at the period of 2 μm, as shown in figure 4-10.

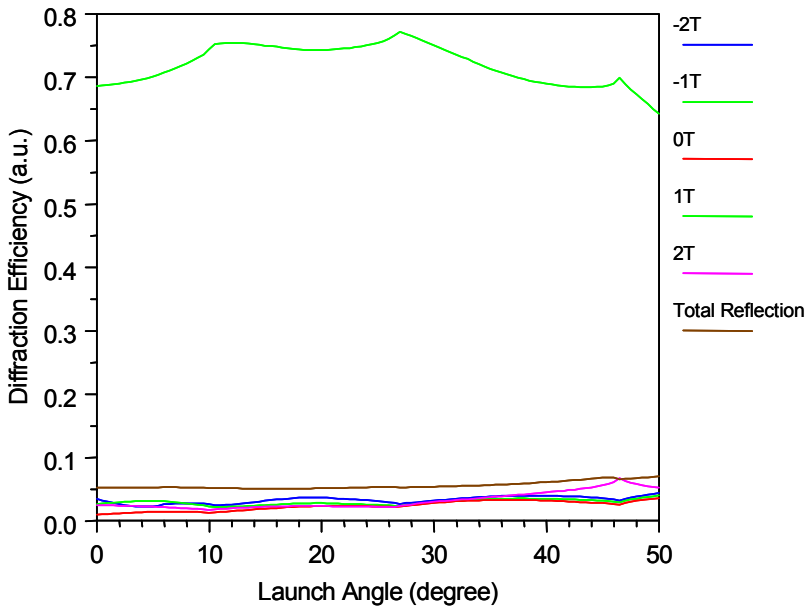

(a)

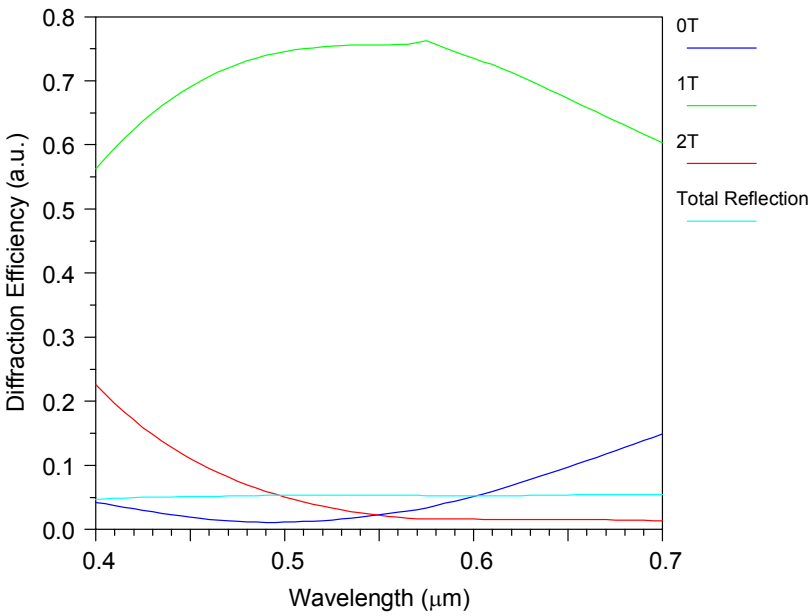

(b)

Figure 4-10 Designed grating diffraction efficiency at non-polarized light input: (a) diffraction efficiency vs launch angle, (b) diffraction efficiency vs wavelength

In this design, a grating with a period of 2 μm cannot be perfectly blazed to 100 % efficiency. Consequently, there is always some light energy in the other diffraction orders. Light contained in these undesirable orders will be bent away from the optical axis as shown in figure 4-11. Once the light hits the GRIN rod lens side wall, it will either be reflected back or transmitted to adjacent information channels in the array structure. In either case, this stray light may reach the detector, leading to additional system noise. One way to avoid this is to add an optical absorber on the GRIN rod lens side wall to absorb the stray light as shown in figure 4-11. This optical absorber can double as the optical glue to keep the multiple information channels aligned correctly in their array structure.

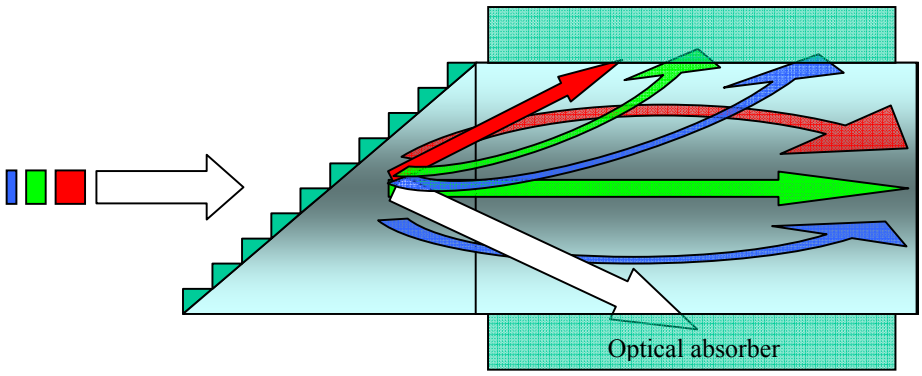

Figure 4-11 Light propagation in designed diffraction element and the final imager

In the computer simulation, the grating material refractive index was assumed to be the same as the index of the GRIN rod lens material. An entire independent information channel is shown in the figure 4-12. An on-axis input beam with a

wavelength of 400 nm (blue lines), 550 nm (green lines) and 700 nm (red lines) wavelength was simulated in this information channel.

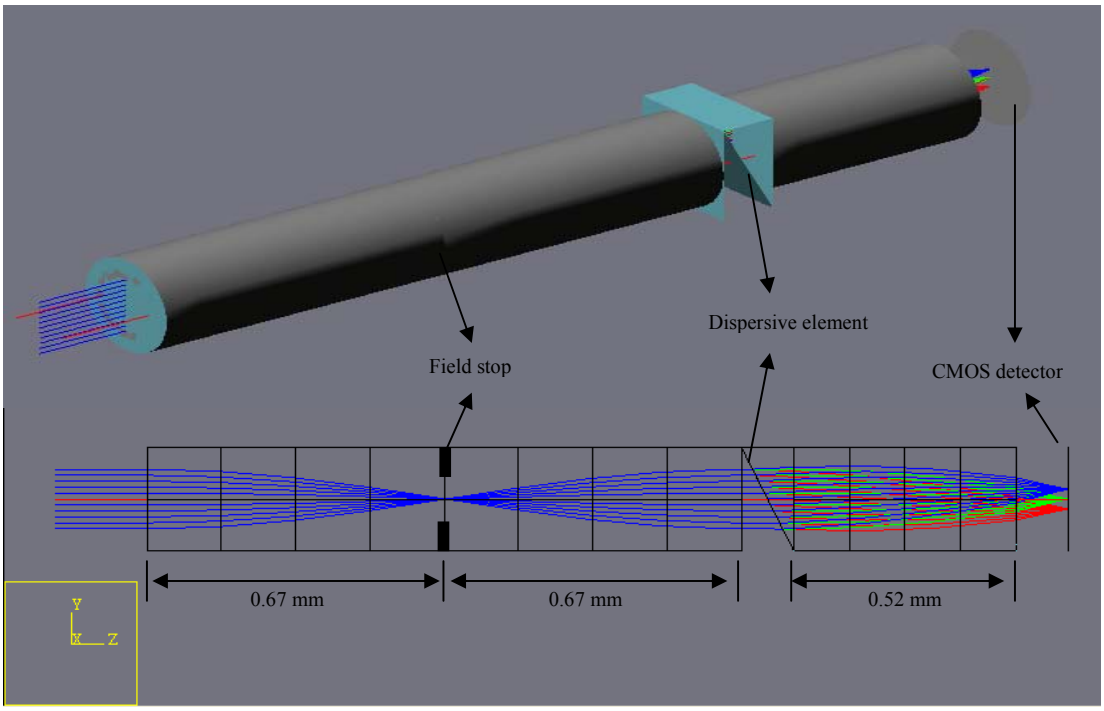

Figure 4-12 Designed individual independent information channel

4.3.2. System tolerance study

The fabrication and alignment tolerance were further studied for the individual CTIS information channel.

The blazed grating profile error will only affect the diffraction efficiency. But a change in the grating period will result in a change in the on-axis wavelength. For example, if the grating period is changed by 0.1μm to 2.1μm, the reference wavelength

will be shifted to 590nm from the desired 550nm. An incorrect prismatic tilt angle has a similar effect. This change will not affect the system image quality.

The length change of a GRIN rod lens will result in a different imaging condition and affect the system aberration. In the ideal case with no fabrication errors, the system is diffraction limited as shown in figure 4-13 (a). If both lenses' lengths in the imaging relay system are decreased by 100 μm each, the output light would not be collimated but divergent, and the system aberration would be out of specification because of mis-focus as shown in figure 4-13 (b). By introducing a 130 μm air gap between these two lenses to compensate the lens length variation and optimizing the imaging distance from the third lens to the detector, the system can be brought back to near diffraction limited operation as shown in figure 4-13 (c). The total path length error for a point at the edge of the field is 0.33 waves.

The alignment error in the direction perpendicular to the optical axis direction will result in the ray propagating further from the optical axis, which not only increases system aberration but also introduces the probability of vignetting by the side wall of the GRIN rod lens. As shown in figure 4-14 (a), the maximum lateral tolerance is 25 μm to avoid vignetting, where the color ray represents the different input angle, not the wavelength. The associated aberration is shown in figure 4-14 (b). The system is still near diffraction limited.

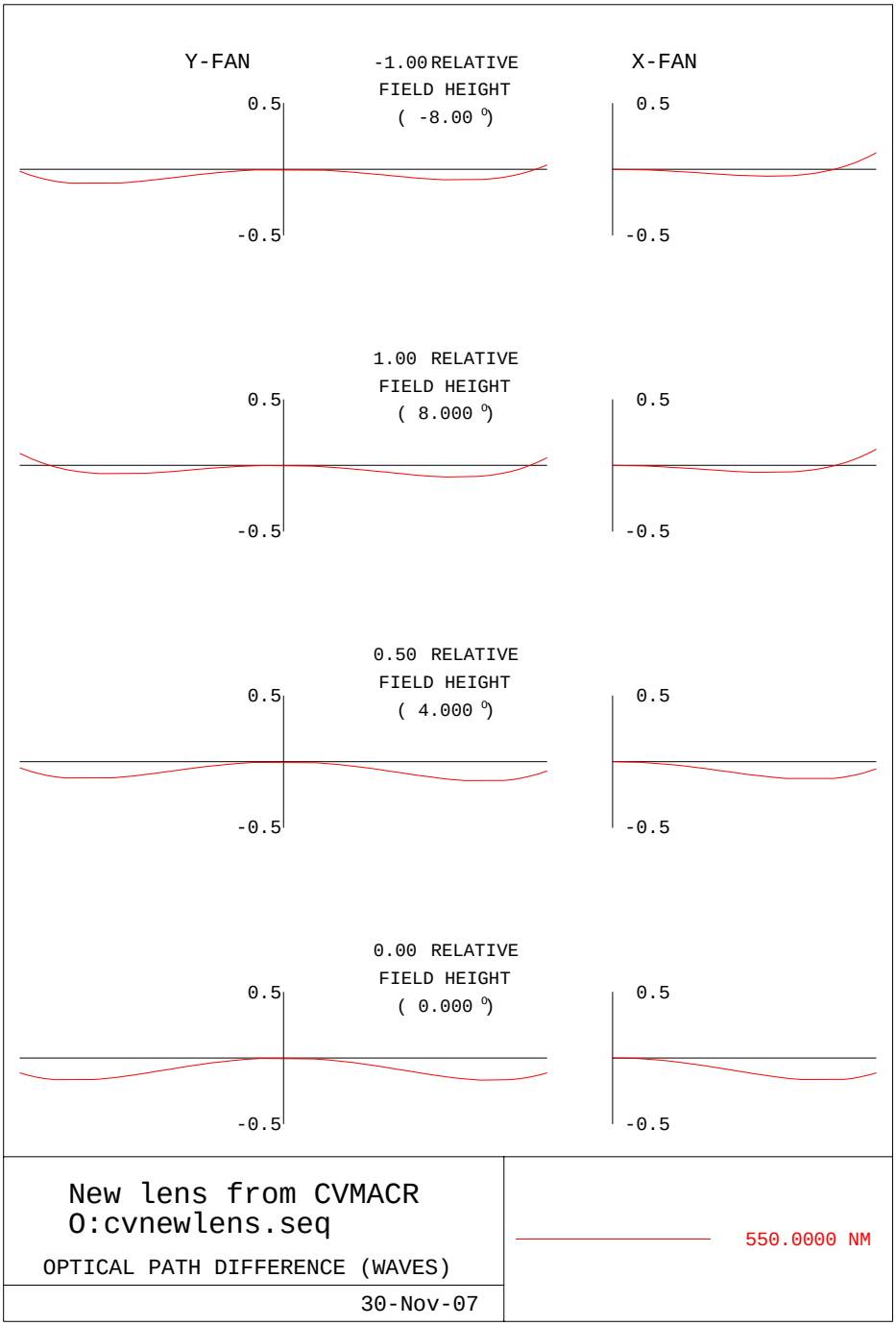

(a) Aberration analysis for ideal situation

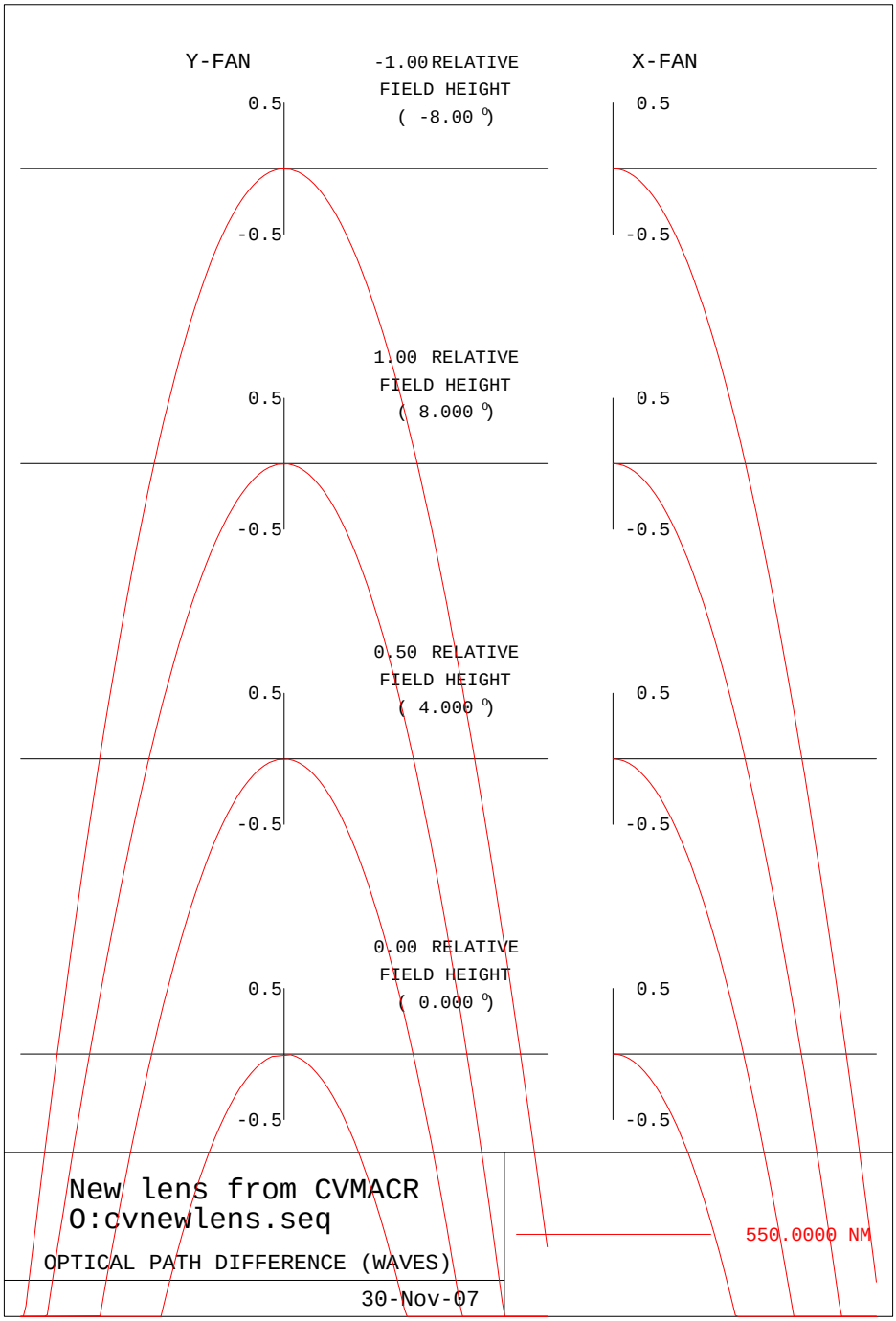

(b) Aberration analysis for lens length variation of 100um

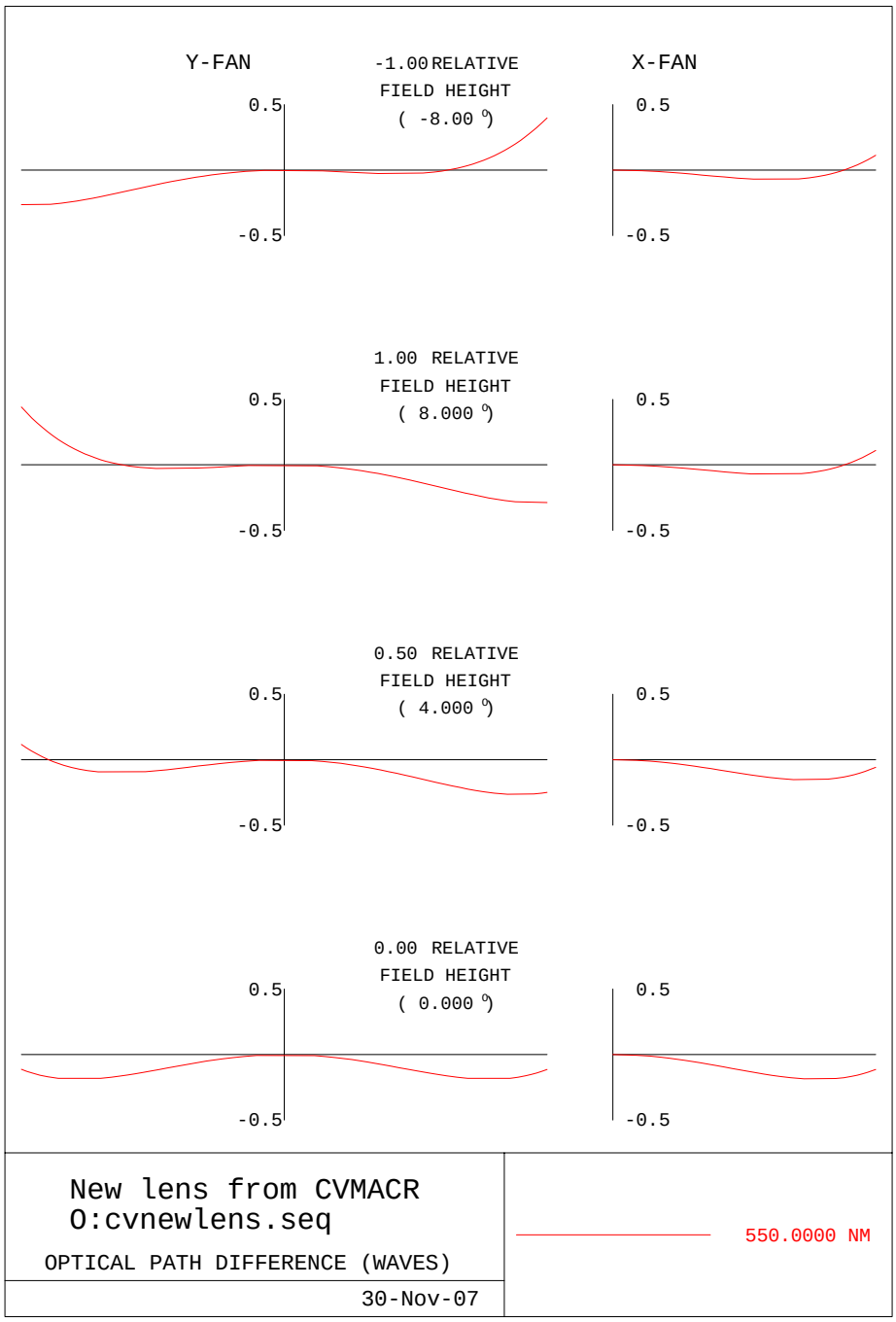

(c) Aberration analysis after the system structure optimization

Figure 4-13 Z direction tolerance aberration analysis

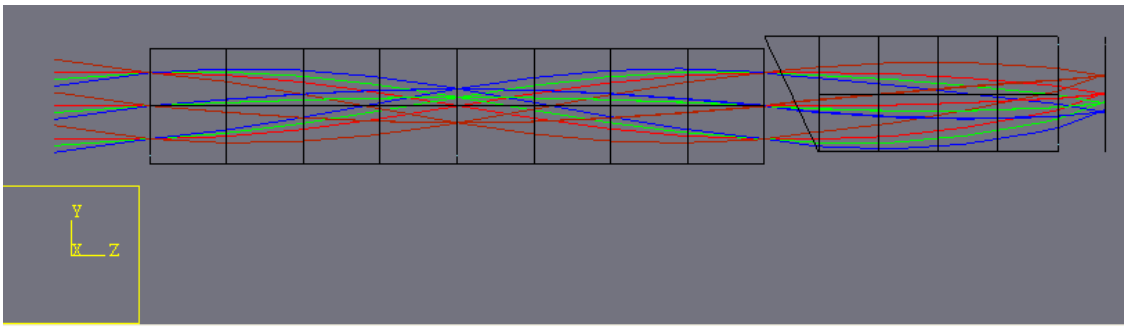

(a) Lateral shift tolerance

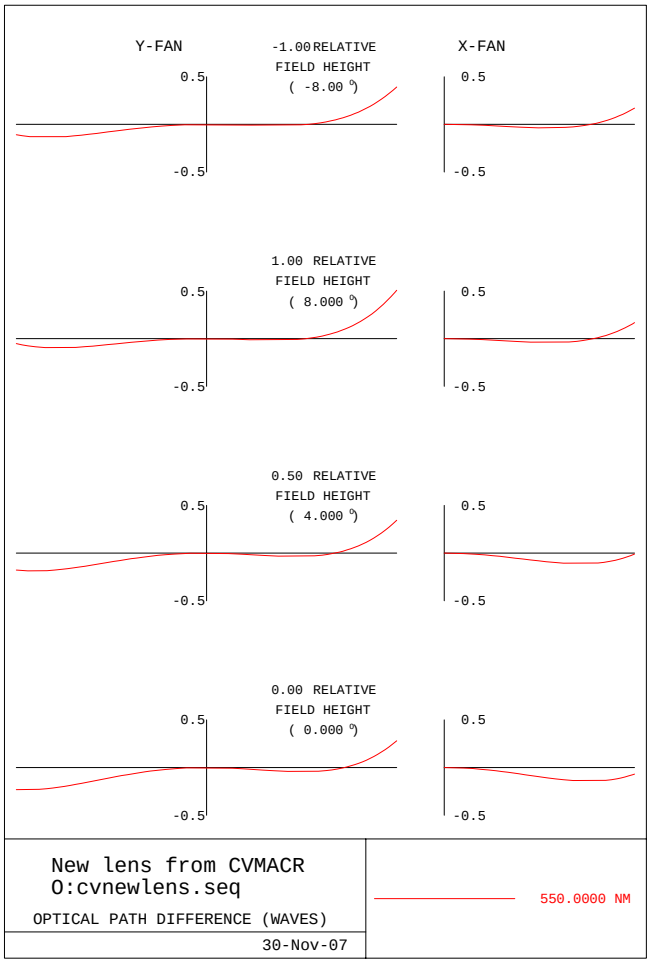

(b) Aberration analysis for lateral misalignment

Figure 4-14 Lateral misalignment analysis

4.3.3. Integrated CTIS sensor array

Once one information channel is designed, multiple information channels can be duplicated and stacked up as shown in the figure 4-15. Each individual information channel can be oriented along different azimuthal directions randomly, or different dispersive element can be used to introduce more dispersion distortions. In this design, 16 independent information channels are integrated into a 1 mm x 1 mm x 2 mm cube.

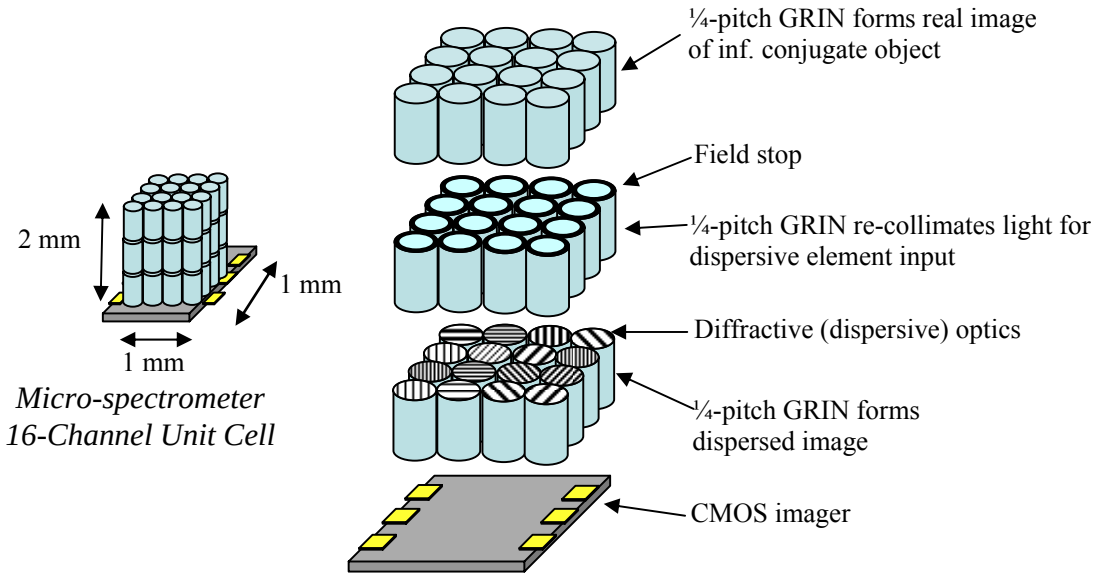

Figure 4-15 Integrated CTIS sensor with 16 independent information channels

5. Fabrication

Two fabrication processes were involved in this sensor design. One is the field stop fabrication and the other one is the grating fabrication. In both processes, the substrate is a flat surface of the GRIN rod lens. So the GRIN lens was first carefully prepared. A set of fine optical lens holders was designed for the small optical element manipulation.

Traditional metal deposition and photolithography technology can be employed for the field stop fabrication. The most complicated procedure is fabricating the grating on the tilted surface with highly accurate profile. e-beam lithography with multiple e-beam-resists was tried but resulted in poor fabrication quality (the reason will be discussed in detail below). As a result, a Focused-Ion beam etching method was used to successfully generate the high quality grating profile on the GRIN rod lens. Since the grating was directly etched in the prismatic surface of the GRIN rod lens, no additional material (e.g. photo-resist) is involved and no additional processing is required.

5.1. Optical element preparation

5.1.1. Optical mechanics design

In our experiment the lens' diameter is 250 μm and the length of each individual quarter-pitch lens is 560 μm. A traditional steel tweezers cannot handle optical elements of such size, because the lens has a tendency to stick on the metal tweezers tip and sometimes the tweezers' steel grooves can damage the lens' side wall. So a specially

designed tweezers with a plastic tip was selected to properly handle the tiny cylinder lenses.

The lens has to be loaded into a vacuum chamber for either metal deposition or grating fabrication. A special lens holder was designed to promote ease of handling. Brass was selected as the lens holder material for several reasons. Strong electronic conductivity and heat dispersion ability are normally required in most common micro-fabrication processes. This material also can be super polished to protect fine optical elements. The 10 mm x 10 mm x 2 mm holder with its central V groove is shown in figure 5-1. This V groove and the hat were specially cut from a single piece of metal by an EDA machine. In this process a thin metal cord with a diameter of 20 μm was used to cut the metal, hence the side wall roughness was estimated to be less than 10 um. The side wall roughness was a significant concern because any stray metal particles could easily damage the glass lens. Also the low roughness provides the advantage that three GRIN rod lenses will be aligned well automatically by simply cascading them in the holder's V-groove.

The holder hat and body are fixed by the smallest standard screw (000). During the fabrication process, a single GRIN rod lens is held at one end of this V groove as shown in figure 5-1 (b) so the lens end inside of the groove will experience more lateral force when the metal hat is attached to the holder body by the screws. A rubber ring was put onto the screw to absorb most of force between the metal and glass to protect the lens.

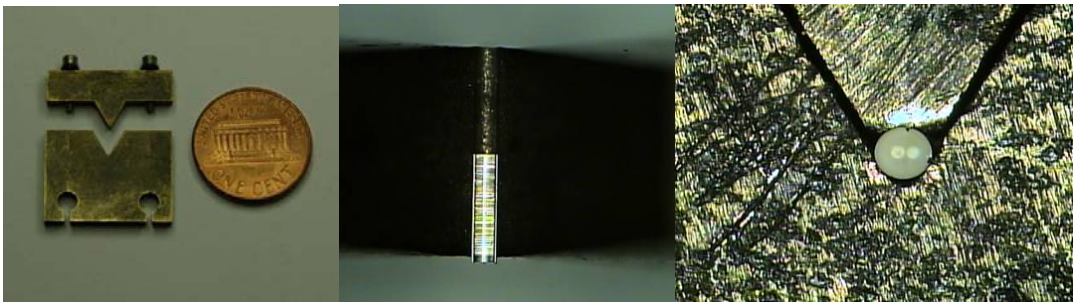

(a) (b) (c)

Figure 5-1 Designed lens holder: a) side view, b) top view with a GRIN lens, c) side view of a GRIN lens loaded in the lens holder

5.1.2. GRIN rod lens preparation

The flat surface of the GRIN rod lens was measured with a white light interferometer to be approximately one fifteenth of the reference wavelength (550nm). In order to tilt the first diffraction order of a 2 μm period grating along the optical axis of a GRIN lens, one end of the lens was cut to an angle of 65°. Several lenses were first loaded into a holder consisting of holes with diameters of 260μm in a plastic sheet and fixed with wax. Then the whole plastic sheet was polished down to 65°. This polishing process was performed by a professional optical company. The cutting angle was measured to be 65.4°. The additional 0.4° angle will shift the on-axis propagation wavelength from designed 550nm to 556nm, and will not affect any other parameters in the design.

The grating profile was optimized to match the GRIN rod lens prismatic surface for on-axis diffraction. The combination diagram of the grating and the GRIN rod lens is shown in figure 4-11.

5.2. Grating fabrication

Several micro fabrication technologies can be employed to make the grating. In the previous push-broom imaging spectrometer project, we successfully used Electron-Beam lithography to fabricate the various gratings. In this project, we experiment with a variety of grating fabrication methods. The following sections describe our results.

5.2.1. e-beam-lithography technology

As an alternative to traditional photo-lithography that employs UV light to pattern photo-resist, electron-beam lithography uses a beam of electrons to generate patterns in the resist[46, 47]. The primary advantage of this technique is that it can improve on the diffraction limit of light and make features in the nano-meter regime. This form of lithography has been widely used in mask-making (for masks used in photolithography), low-volume production of semiconductor components, and research & development. e-beam lithography is not suitable for high-volume manufacturing, however, because of its limited throughput. The beam must be scanned across the surface to be patterned, resulting in a serial process. This normally results in a very slow writing speed compared with a parallel technique like photolithography (the current standard) in which the entire surface is patterned at once.

5.2.1.1. Proximity effect

The resolution of traditional contact photo-lithography is limited by the diffraction of the light as it passes through the resist. In order to achieve a smaller point spread function, shorter and shorter wavelength light source has been used. Electron lithography offers higher patterning resolution than optical lithography because of the shorter wavelength possessed by the 10-50 keV electrons that it employs. However, electrons are charged elements, which interact heavily with the material and experience strong scattering as they pass through the resist. In addition, this scattering can occur during the forward propagation in the material or the backward random reflection from the substrate. These scattering effects often result in a large point spread function.

The lithographic process is usually modeled as a linear system where the point-spread function of the system is given by a double-Gaussian of the form:

$$PSF(r) = \frac{1}{\pi(1+\eta)}\left\{\frac{1}{\alpha^2}\exp(-\frac{r^2}{\alpha^2}) + \frac{\eta}{\beta^2}\exp(-\frac{r^2}{\beta^2})\right\} \qquad (5\text{-}1)$$

where r is the radial position coordinate and α, β, and η are fit parameters[48, 49]. The first Gaussian term accounts for forward scattering of the electrons as they pass through the resist. The second Gaussian term accounts for electrons that scatter backwards within the resist and from the substrate. The η parameter characterizes the amount that the backscattered electrons contribute to the total exposure dosage. There are several ways to measure these parameters[50, 51]. Values of the proximity correction parameters α, β, and η were obtained from the literature[52].

5.2.1.2. E-beam-resist Su-8

In the miniature push-broom imaging spectrometer project, we used SU8-2002 e-beam-resist[53] to pattern the grating. This resist has a negative response so there will be no other residue left on the optical surface after the fabrication process except the pattern. This transparent material is very chemically and physically durable, and therefore is often a very good candidate to transfer the pattern into the substrate.

The contrast curve of SU8 was first calibrated as shown in figure 5.2. The grating fabrication parameters can be calculated based on this calibration curve and optimized by the proximity correction model. The exposure files for the blazed gratings were generated by writing appropriate scripts for the 3Lith program purchased with the Raith 150 electron-beam lithography tool[54]. This program optimizes the written dose profile to compensate the proximity effect.

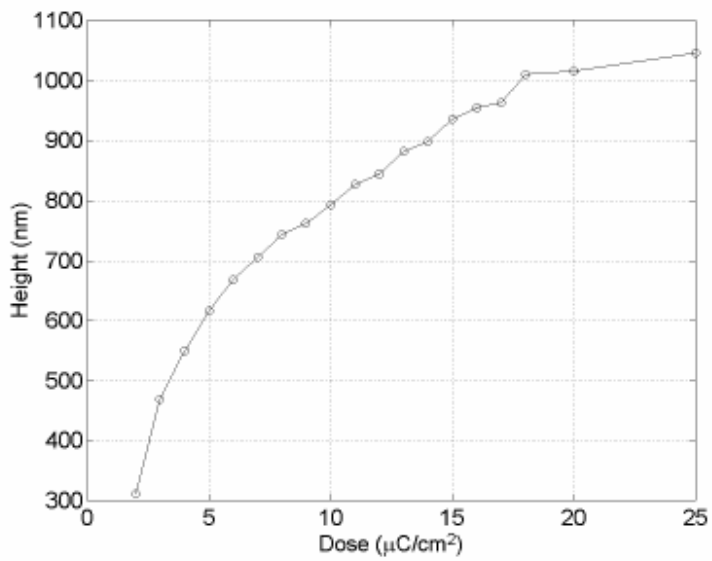

Figure 5-2 SU-8 calibration curve

Based on 3lith simulations, the maximum height cannot exceed 75% of full calibrated depth in order to provide the best proximity correction. For the designed 2μm grating, the modulation depth is 852.1μm, which fulfills the SU-8's linear dynamic range as shown in figure 5-2. However, there is not enough dynamic range for the 3lith program to compensate the scattering effect. By setting the maximum available height to be 100% of the full calibrated depth, the simulation predicted that the largest modulation depth will be 650nm as figure 5-3 shows. Unsurprisingly the true fabricated grating modulation depth was only around 250nm, much less than the desired value. So this material is not appropriate for this application.

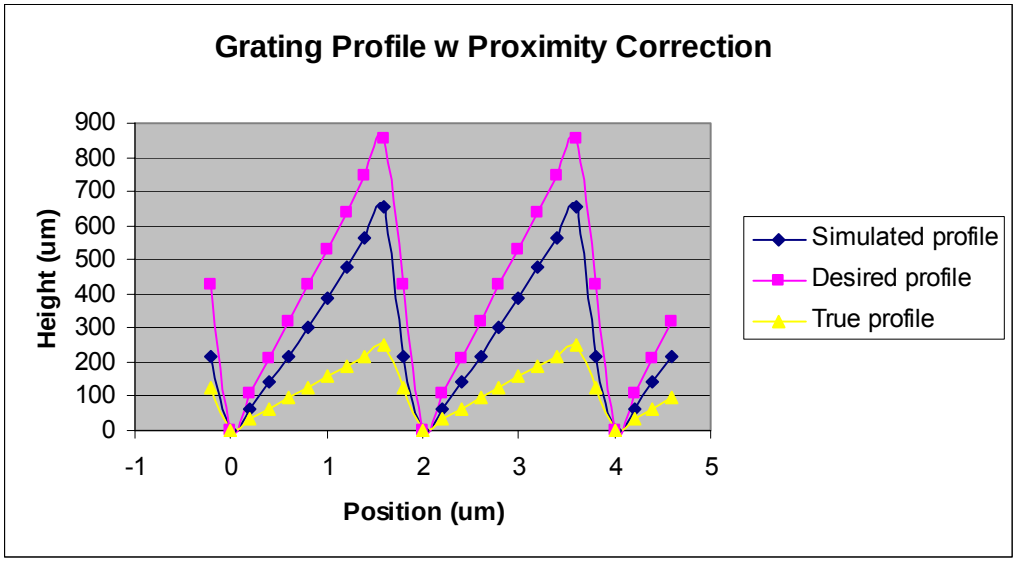

Figure 5-3 Grating designed, simulation and fabricated profile

5.2.1.3. Spin-on-glass e-beam resist

A new e-beam resist, Spin-on-glass[55], was considered as an alternative to SU8. Spin-on-glass resist is a deep UV and electron sensitive material which will turn into silicon oxide after a high temperature bake. The basic molecular structure is shown in figure 5-4. The material can have a thickness of up to 2 μm after the process. This glass-based material has a similar refractive index to the GRIN rod lens and can work directly as a high-quality optical material.

The material was calibrated with the same e-beam lithography tool and the result is shown in figure 5-5. Clearly it is very sensitive to the electron exposure. The slope of the exposure curve is very high in the linear region. A 200 nm wide line was patterned in this material and measured with an atomic force microscope (AFM) as shown in figure 5-6. The forward and backward scattering effects can be modeled easily according to the double Gaussian shapes. The correction parameters α and β were calculated with a Gaussian fitting method. This method will account for e-beam machine effects, the material quality and process conditions. The 3-lith algorithm was carried out based on these calculated parameters. The simulation and experimental results again show a much lower grating modulation depth than the desired value.

There are two main reasons for the failure. First, this material is primarily designed for binary structure fabrication, so the high sensitivity cannot be compensated accurately. Second, the designed grating modulation depth is relatively large for this material's dynamic rang. In order to achieve this large value, the dose variation range is relatively large. The grating triangular shape places a large dose area next to a small dose

area, which results in over-development of the low dose. Our results show this material is not a good candidate for this application.

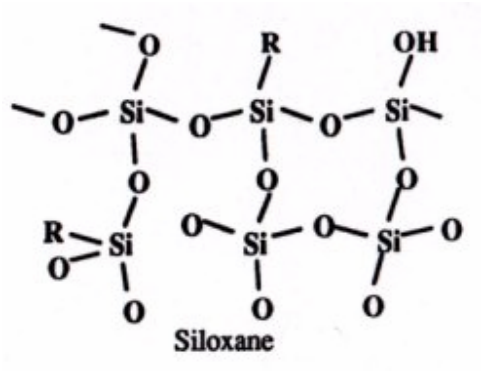

Figure 5-4 Silicon-on-glass resist molecule structure

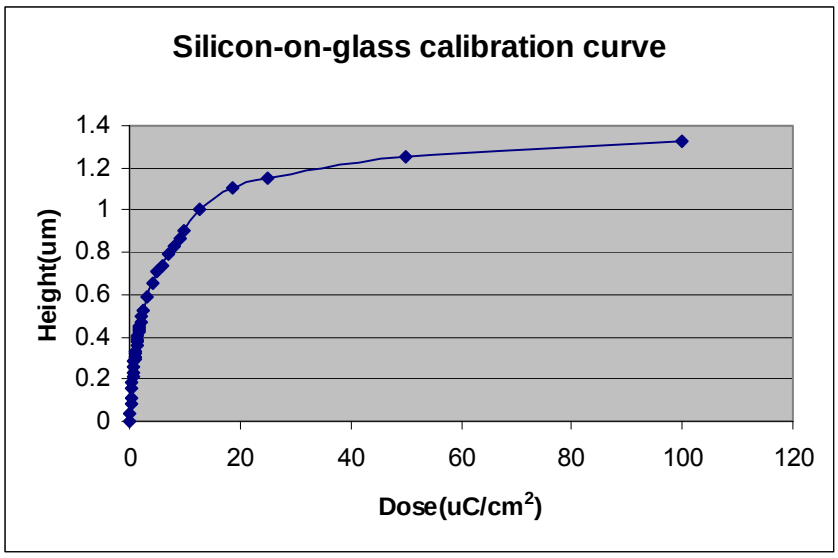

Figure 5-5 silicon-on-glass material calibration curve

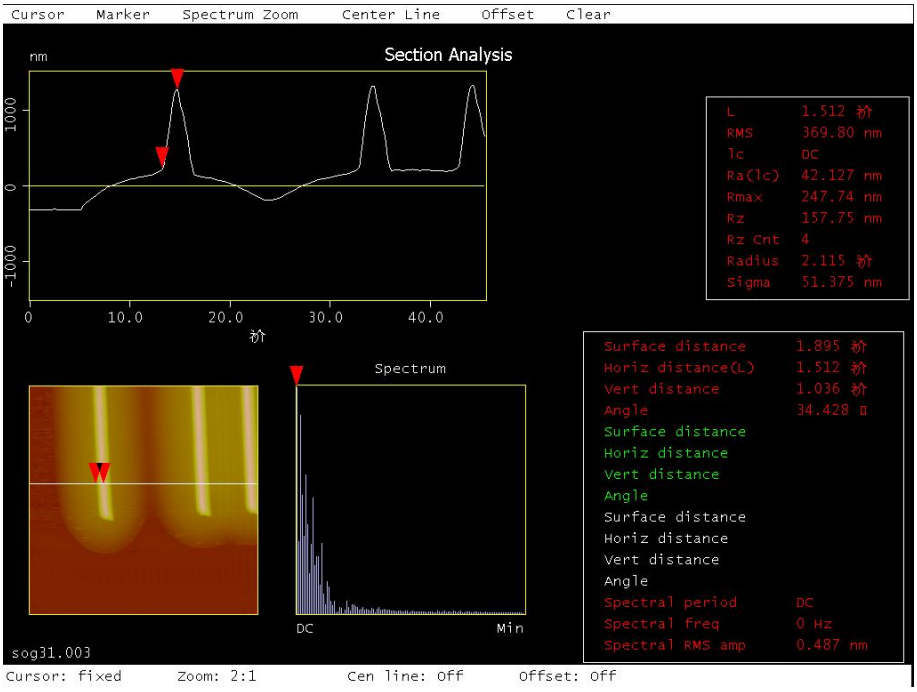

Figure 5-6 Line spread function AFM measurement result

5.2.2. Focused-Ion Beam Etching method

A focused ion beam machine, also known as a FIB[56], is a scientific instrument that resembles a scanning electron microscope. However, instead of electrons, the FIB focuses a beam of gallium ions onto the sample in the chamber. Gallium is chosen because it is easy to build a gallium liquid metal ion source (LMIS). In a Gallium LMIS, gallium metal is placed in contact with a tungsten needle and heated. Gallium wets the tungsten, and a large electric field (greater than 10^8 volts per centimeter) causes ionization and field emission of the gallium atoms. These ions are accelerated to energies of 5-50 keV and then focused onto the sample by electrostatic lenses. A modern FIB can

deliver tens of nano-amps of current to a sample or can image the sample with a spot size on the order of a few nanometers[57].

Unlike an electron microscope, the FIB is inherently destructive to the specimen. When the high-energy gallium ions strike the sample, they sputter atoms from the surface. Gallium atoms will also be implanted into the top few nanometers of the surface, and the surface will be made amorphous. Because of the sputtering capability, the FIB can be used as a micro-machining tool to modify materials at the micro- and nano-scale.

The advantages of this method for our study are obvious. The grating is directly patterned into the GRIN rod lens, and no additional processing is needed. No resist spinning and chemical developing are involved, which significantly reduces the chances of mishandling the tiny optical lens.

The disadvantage is the process speed. In order to preserve high lateral resolution, the ion current is usually set to a very small value and accordingly the etch rate can be very low. This method is most suited to R&D work rather than a manufacturing process.

Since the charged ions are used to bombard the substrate surface, surface charging on a nonconductive material like glass can be a problem (as it is in an e-beam lithography process). The FIB tool we used contains both an ion gun and an electron gun, so FIB and SEM function can be applied at the same time. There is a special function called "Neutralization", using electrons to neutralize ion particles to eliminate the charging problem. But we found this function to be unstable, most likely due to the age of the SEM electron source. In the end we decide not to use this function to solve charging problem.

After the lens was loaded into the metal holder, a thin Au layer was coated onto the lens prismatic surface to remove the charge during the etching process. A great advantage of using a metal coating layer is that the metal layer will be removed only in the patterned area; in the unpatterned area, the metal layer still exists, which can function as a baffle to block the stray rays into the final images. 200 nm-wide lines and 10 μm x 10 μm squares were first patterned on the glass substrate for point spread function and dynamic range calibration measurements as shown in figure 5-7 and 5-8. Since the patterns are etched into the substrate, a traditional Atomic Force Microscopy (AFM) probe cannot scan into the deep narrow trench. Instead a scanning electron microscope (SEM) was applied to estimate the etched pattern sizes under different current conditions. AFM measurements in the open square area do show very low roughness on the etched surface, with the variation measured to be only several nanometers as shown in figure 5-7(b).

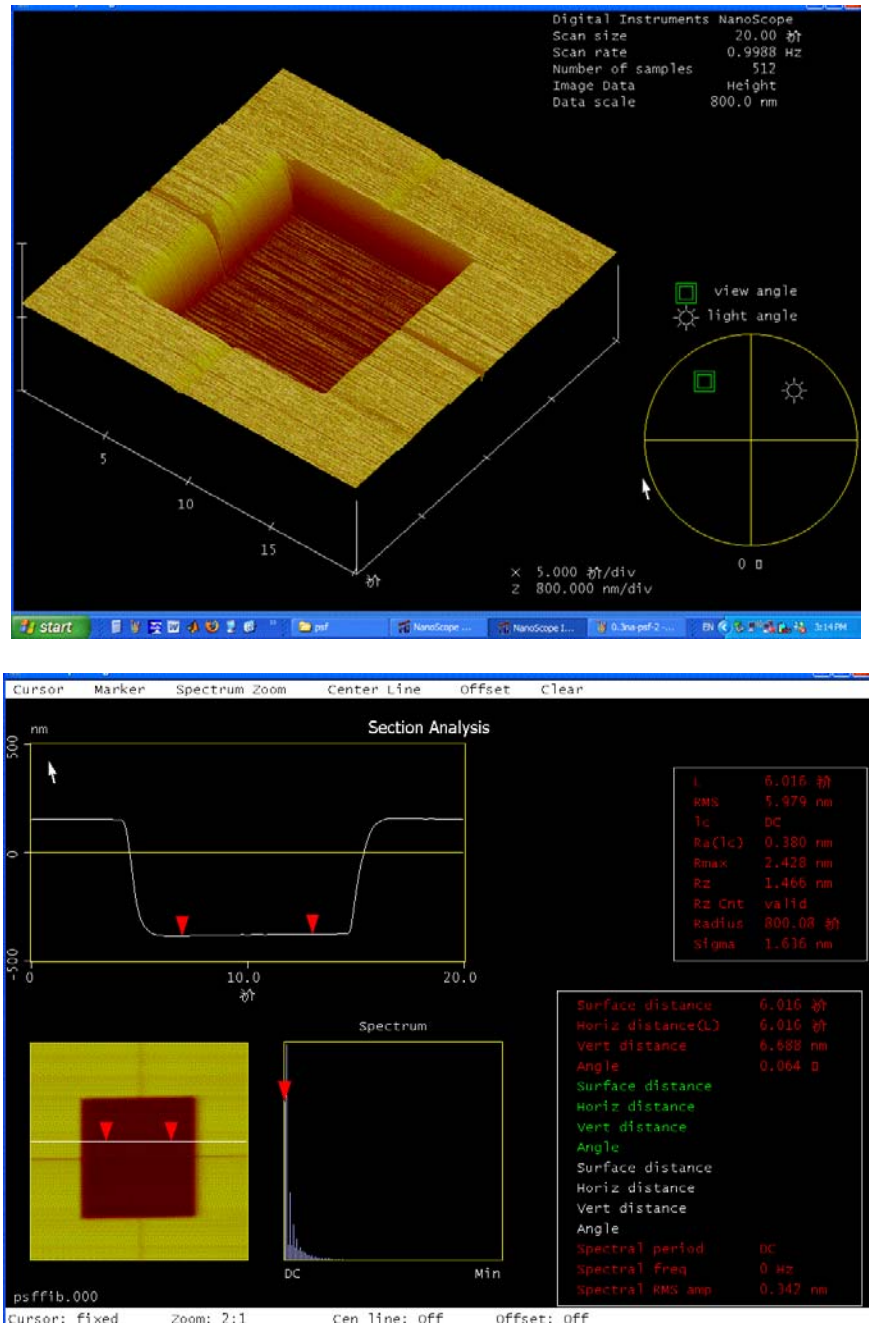

Figure 5-7 FIB point spread function and calibration curve AFM measurement result

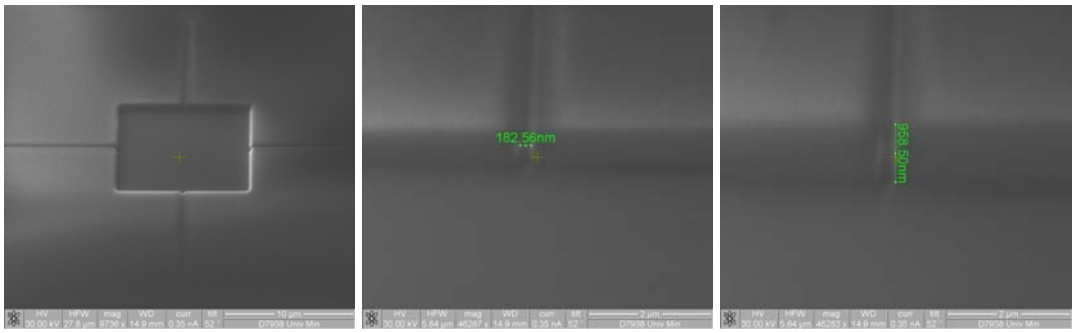

Figure 5-8 SEM measurement of FIB point spread function and calibration curve

The SEM readout proved the FIB's high anisotropic etch property. 0.3 nA ion current will result in the 220 nm lateral resolution. The resolution can be improved by decreasing the ion current. In some applications the lateral resolution can be as small as 10 nm with 10 pA current[56]. In our study the 220 nm resolution is good enough for our 2 µm-pitch grating fabrication. Larger current results in the faster etching rate. With 0.3 nA current the measured etch rate is around 0.073 μm^3/minute, which will result in 4 hours etching time to pattern a grating with the size of 200 µm by 200 µm.

The machine we used supplies some calibrated etching recipes for certain materials. It will convert the input depth into etching time automatically based on the pre-stored calibrated relationship. Users need only input the desired pattern depth profile and material. Unfortunately, it is quite complicated to define a recipe for a new material. So we decided to modify the most approximate material to simulate our silicon dioxide-based glass. The recipe we selected was for silicon-nitride. The etching depth on glass was calibrated relative to the depth on silicon-nitride at the different etching time fixed in

the recipe for silicon-nitride material. The calibration curve is shown in figure 5-9. This linear relationship simplifies the recipe modification.

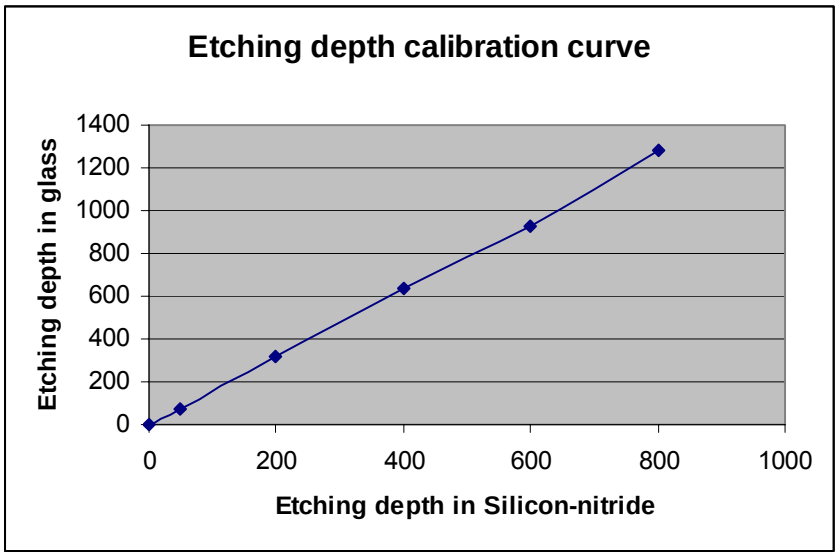

Figure 5-9 etching depth calibration result

The point spread function cannot be measured accurately by the SEM method, but the highly anisotropic etching ability is visually shown in the SEM pictures. So a conclusion can be drawn that proximity correction methods will not be needed in this method. The grating fabrication recipe will be generated based on the linear calibration curve, and the individual pixel values will be adjusted based on the measured grating profile with the SEM.

As a preliminary test, a 5-period grating was fabricated on the edge of a fused silica substrate to optimize recipe (see figure 5-10). The fabricated grating shape could be made to match the designed profile accurately by adjusting the individual position's

etching depth. The observed roughness is caused by the non-polished substrate edge surface. The SEM top view picture shows the grating surface roughness is very small as shown in figure 5-11.

Once the grating fabrication recipe was determined, a 200 μm by 200 μm grating was fabricated in the center of the GRIN rod lens prismatic surface, as shown in figure 5-12. The FIB etching area is coupled to the ion current. At 0.3nA current, the maximum writing field is 100 μm x 100 μm. As a result, this grating was fabricated in 4 pieces. Since the FIB machine is not equipped with an interferometrically controlled stage, stage error is unavoidable, which can be clearly seen in the SEM pictures.

Because the GRIN rod lens was loaded imperfectly into the metal holder, there is a small area shadowed by the metal holder where the grating was not fabricated. The white glare in the picture was caused by the electron charging problem in the grating area during the SEM imaging, where the metal coating was already removed during the ion etching process. Figure 5-13 shows a closer look at the grating in the GRIN rod lens.

This grating was blazed to maximize the first diffraction order, with the modulation depth of 775 nm. In order to increase the spectral resolution of the CTIS sensor, the grating may be blazed into higher diffraction orders where the modulation depth would be even larger. In some other applications, high modulation depth blazed gratings may also be required. Therefore, fabrication of a high modulation depth triangular shape structure was further studied. A 1.5 μm modulation depth was successfully achieved for 2 μm period blazed grating as shown in figure 5.14.

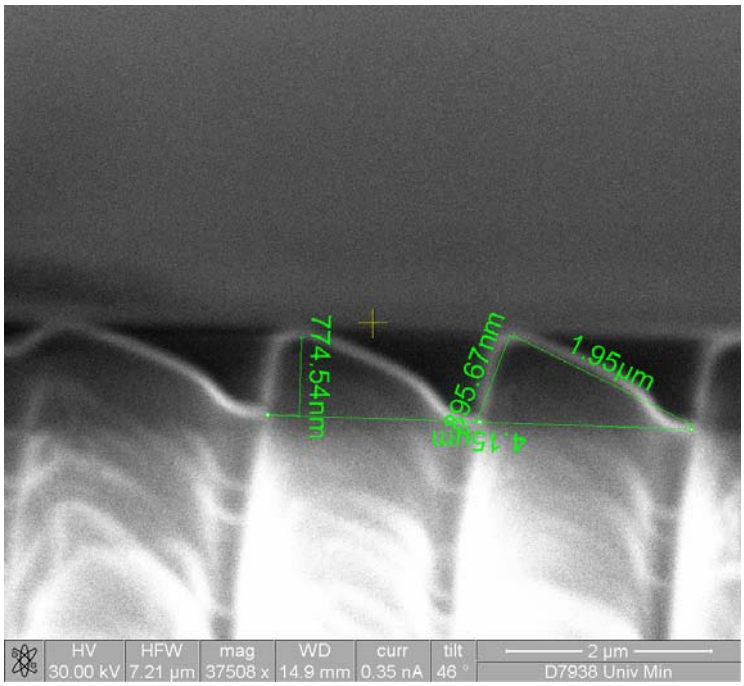

Figure 5-10 SEM picture for grating profile measuremen

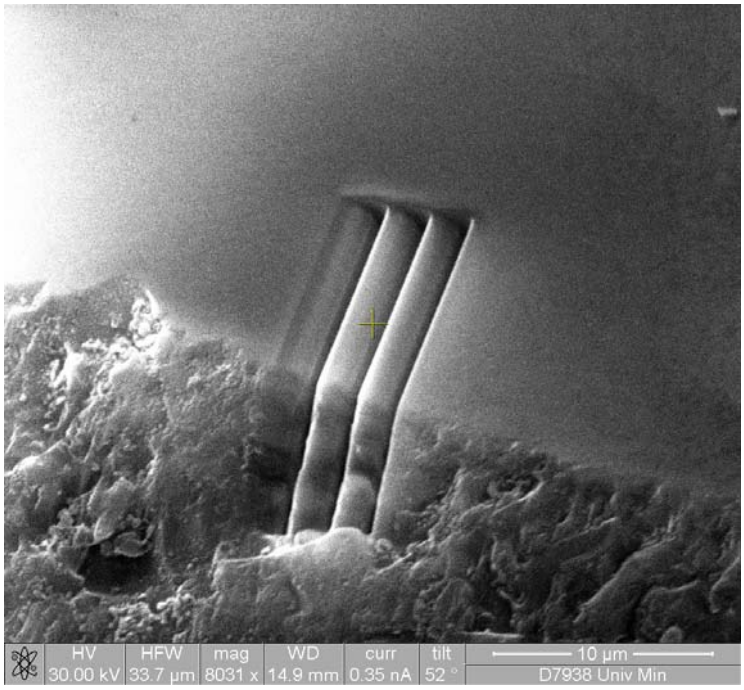

Figure 5-11 SEM picture for grating profile top view

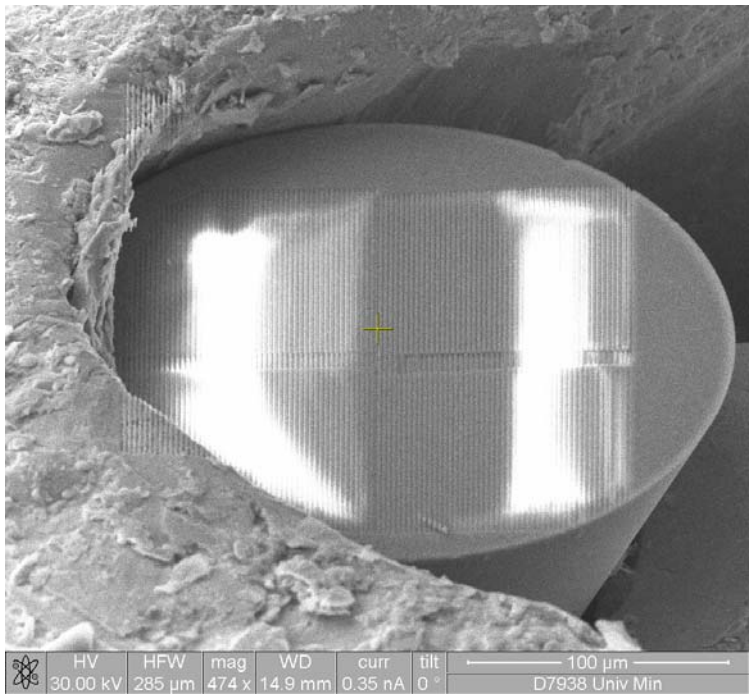

Figure 5-12 Fabricated grating on the GRIN rod lens

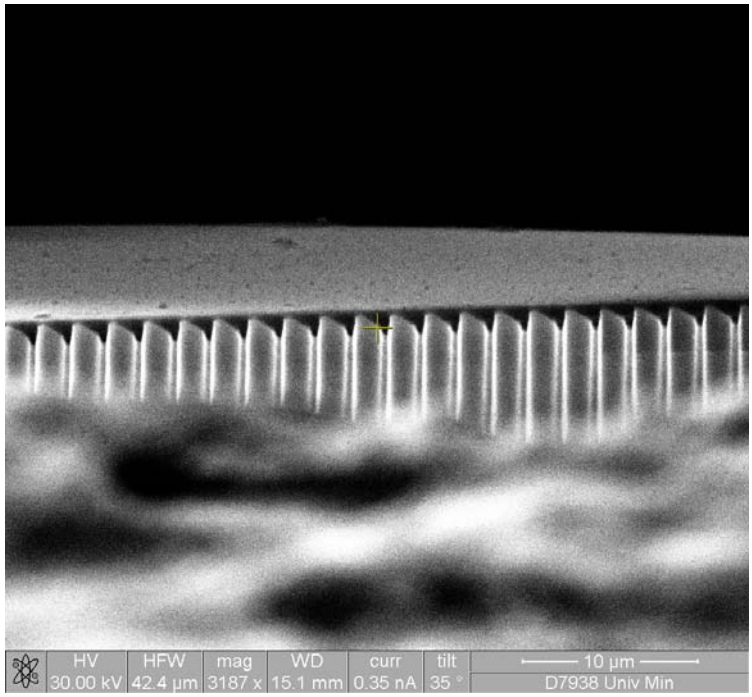

Figure 5-13 Close look at the grating in the GRIN rod lens.

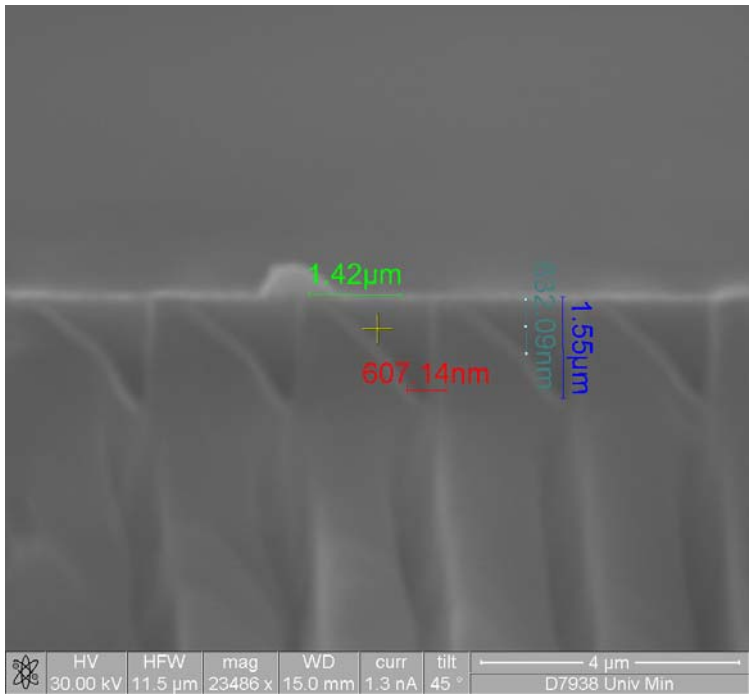

Figure 5-14 large modulation depth grating SEM picture

6. System Test

The imaging performance of the optical system composed of three quarter-pitch GRIN rod lenses was first evaluated. Then a grating was fabricated in a fused silica substrate, and the diffraction efficiency was tested with a laser.

One information channel was fabricated. A first-order blazed grating with the period of 2 um was directly etched into the prismatic surface of a GRIN rod lens. By rotating this information channel along the optical axis, spectral dispersions associated with different azimuthal directions can be introduced into the image of the object. In this way the sensor array's output can be simulated with only one information channel. The designed CTIS sensor's performance was tested based on this method. A multiple-spectral object and a hyper-spectral object were built using LED light sources and color printer dye on transparency material, respectively. The spectral information was reconstructed successfully.

6.1. Single information channels characterization

6.1.1. Imaging system characterization

Three quarter-pitch GRIN rod lenses were cascaded in a row to build an imaging system with no grating and prismatic surface involved. Then the imaging quality of CTIS information channel can be evaluated through this imaging system. A He-Ne laser source was used to test the imaging system point spread function as shown in figure 6-1. Since no entrance pupil aperture was included in the test imaging system, the true NA is 0.386 rather than the designed 0.25. The on-axis point spread function was measured in both x

and y directions since most of the light will be concentrated around the optical axis. The measured results match the theoretically predicted point spread function curve very well, and strongly support the near diffraction limited imaging quality predicted by the CodeV simulation.

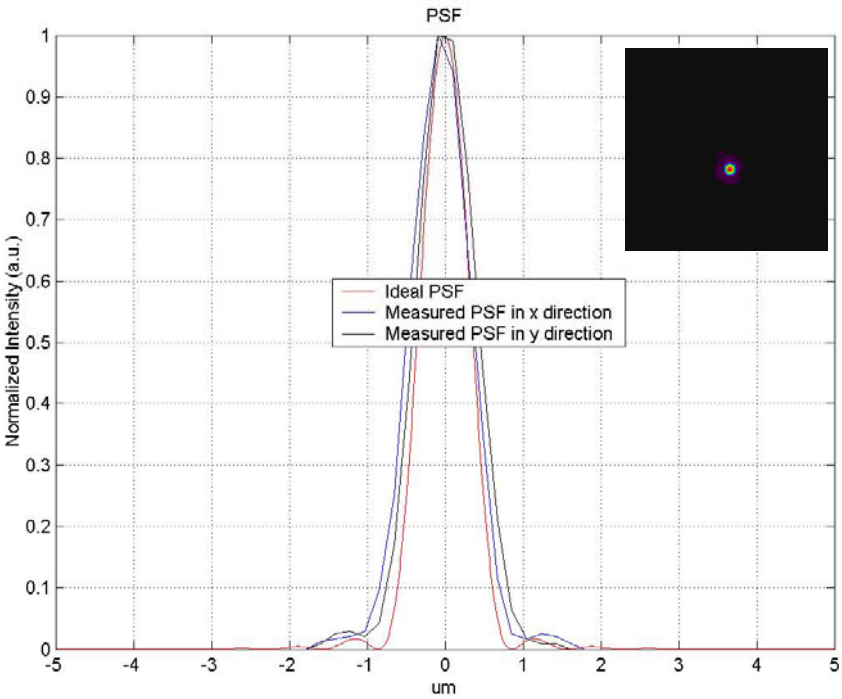

Figure 6-1 Imaging system point spread function theoretical prediction and measured data, the insert image is the captured point spread image.

Figure 6-2 shows a true picture collected by this imaging system. A person, a computer and other furniture can be clearly recognized. Since the aperture size of this imager is only 250 um, the object side angular resolution is 0.15^0. This is the reason why no further detailed information can be observed from this picture.

Figure 6-2 Picture collected as a tested of the imaging system

6.1.2. Grating efficiency test

A 100 um by 100 um grating was fabricated on the fused silica substrate. The grating period is 2 um, blazed to the first diffraction order. The grating profile was optimized to match the GRIN rod lens prismatic surface to provide near optical-axis dispersion as described in Chapter 4. A He-Ne laser was used to test the grating's diffraction efficiency. The laser input angle is 25^0 from the grating's normal to simulate the true application condition in the CTIS sensor. The measured first order efficiency was 63% with unpolarized input light, which matches the theoretical predicted value very well (see figure 6-3). This result proves the conclusion that the FIB method can fabricate the high modulation depth blazed grating profile very accurately.

6.1.3. Single information channel test

A microscope with a back side illumination system was built for a single information channel test and further CTIS sensor performance demonstration. The set-up is shown in figure 6-4. A white light fiber illuminator is used as a light source. Two lenses image the fiber illuminator output facet onto image plane b. Lenses 2 & 3 project

the aperture onto the object to provide a uniform illumination. A metal mask with a through-hole pattern was used as the object. The spectrally dispersed images, oriented along different azimuthal directions, are collected and shown in figure 6-5. In order to collect the zero order non-dispersed image and the first and second diffraction order spectrally distorted images simultaneously, the image conjugation condition was adjusted so that all three order images were projected onto the detector. Obviously by rotating the information channel into different azimuthal directions, the different spectrally dispersed images can be generated. These images were collected with a color camera. In the CTIS sensor performance demonstration test, a gray scale camera was used to avoid the additional spectral distortion introduced by the camera's color filters.

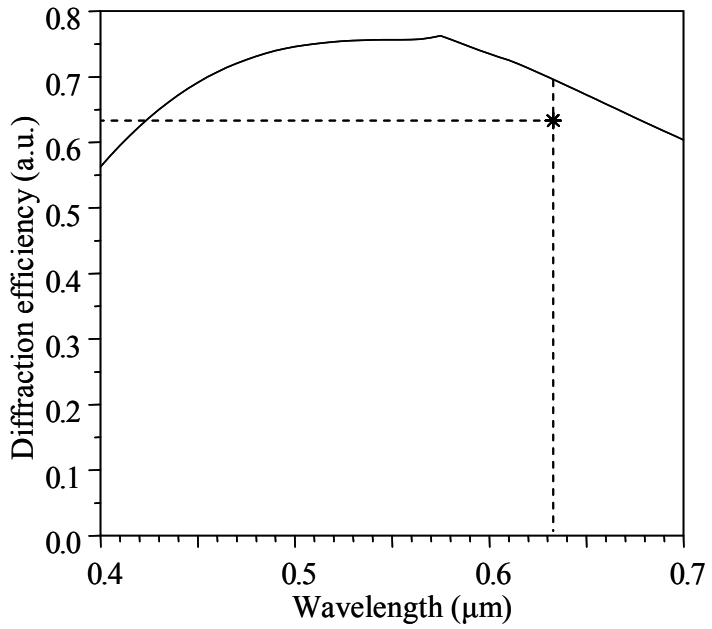

Figure 6-3 First order diffraction efficiency verse different wavelength @ 25^0 input angle

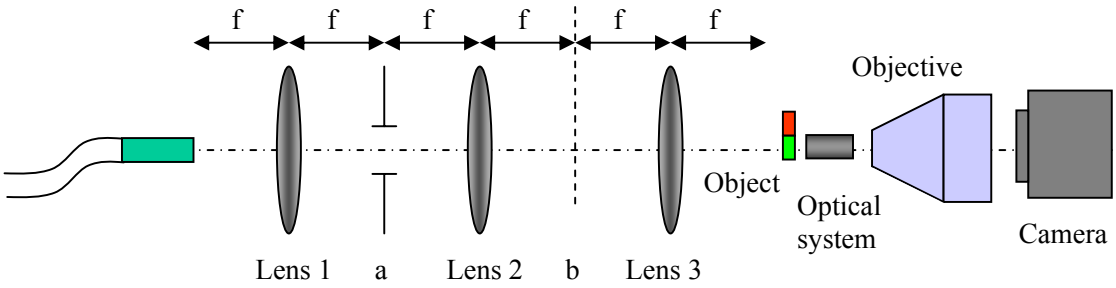

Figure 6-4 Optical set up diagram for single information channel and CTIS sensor test

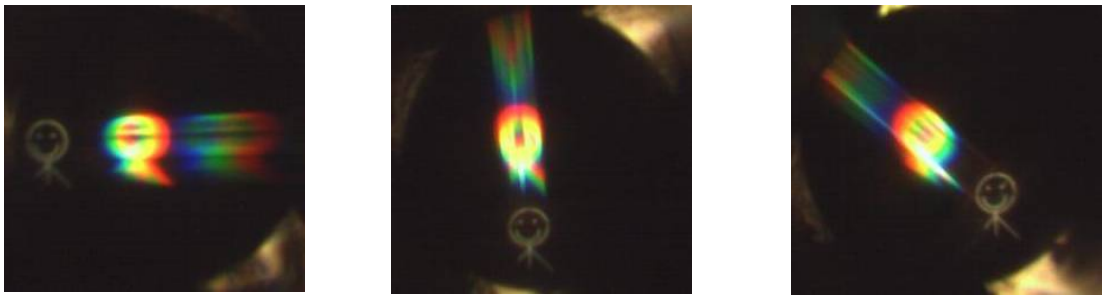

Figure 6-5 Spectrally dispersed images, where dispersion occurs along different azimuthal directions. The zeroth, first, and second diffraction orders can all be seen.

6.2. Micro CTIS sensor imaging function test

6.2.1. Information channel calibration and output image registration

The calibration and registration procedure[58] must be performed for every information channel before the hyper-spectral information can be correctly reconstructed. The instrument is calibrated by accurately measuring the azimuthal angles associated with different information channels. The registration process corresponds to locating the image center in the different information channels. These two key processes directly affect the system resolution.

In this experiment, two narrow band-pass filters were used to aid in the calibration and registration processes. One filter wavelength was centered at 525 nm, and the other at 625nm. Both filters had bandwidths of 10nm, as measured with a monochrometer.

On a metal mask, a small alignment hole was covered by one color filter, and the image was collected with a grayscale camera. Then another image was captured with the second color filter. Using Matlab to add these two images together, the dispersion between these two distinct spectra can be observed clearly in figure 6-6 a, b and c. The dispersion direction, or the information channel azimuthal angle, can then be calculated accurately.

Information channel registration can also be processed based on these two images. The spot position at the reference wavelength can be calculated from the figure 6-6 d). Since the image at the reference wavelength experiences no dispersion and does not shift position at different azimuthal angles, this position can be used as the image center to register the different information channel outputs.

When the same grating is used, the spots with different wavelengths always keep the same absolute shift distance from each other independent of channel orientation. So as long as a spot in any particular wavelength can be separated from other wavelengths clearly, this spot can be used to register the images at different azimuthal angles.

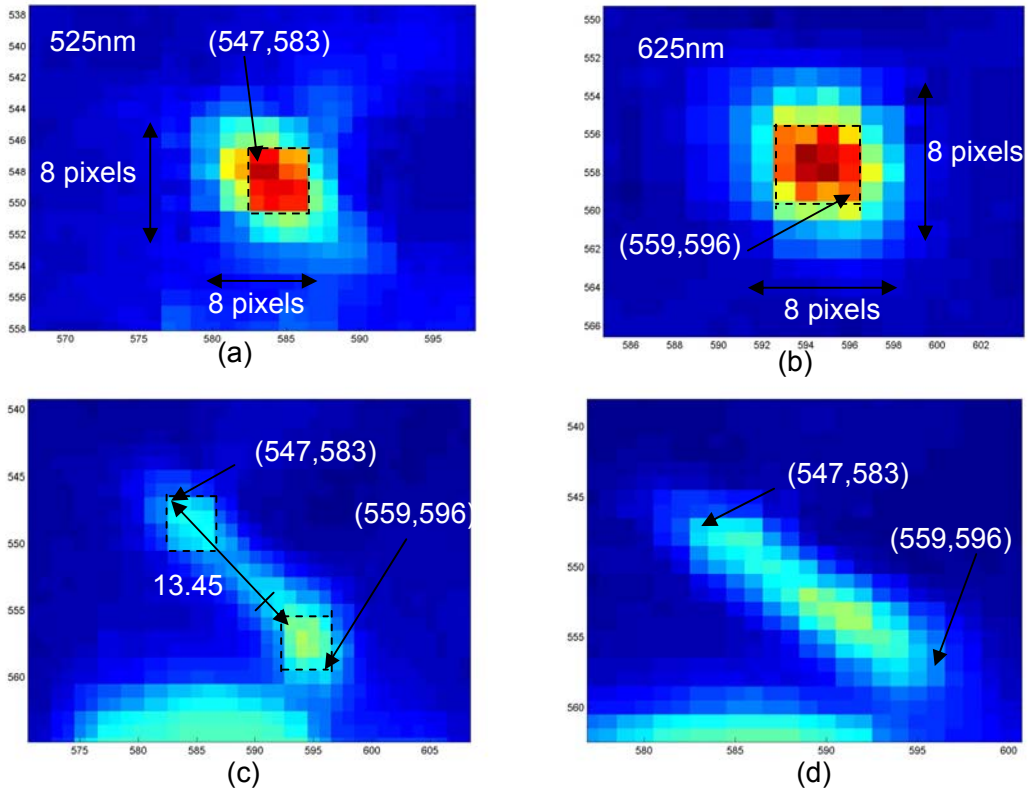

Figure 6-6 System calibration and registration: a) spot position @ 525nm, b) spot position @ 625nm, c) the relative position of these two spots, d) spot dispersed image with a continuous white light source

6.2.2. Performance demonstration with a multiple-spectral object

A multiple-spectral object was constructed with two red LEDs and two green LEDs, as shown in figure 6-7. The object was put far away from the CTIS sensor so that the LEDs appeared as spatial point sources along the x- and y-directions. The double point source carries the sinusoidal distribution in both spatial and spectral frequency domains, leading to enough accessible information in the useful data zone.

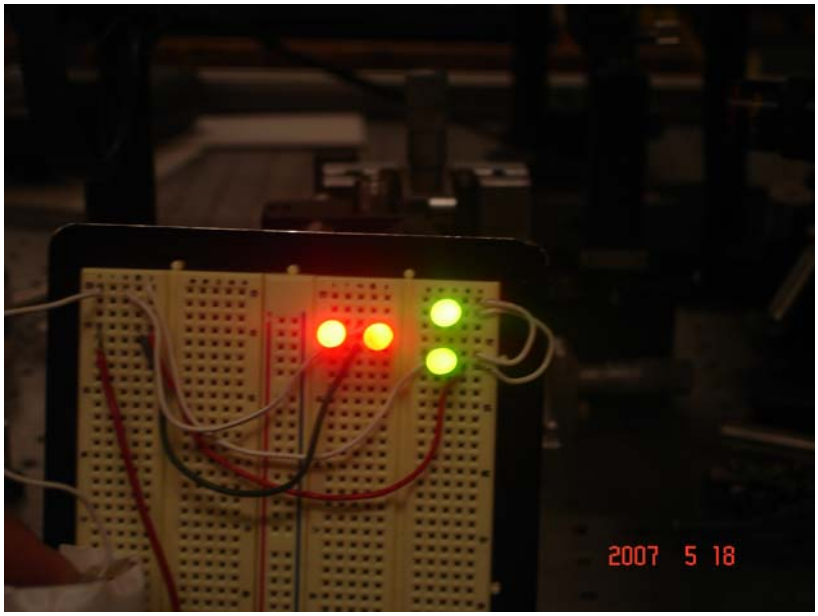

Figure 6-7 A multiple-spectral object built up with 4 LEDs

A single information channel was rotated to three azimuthal directions and these three spectrally dispersed images were recorded, shown in figure 6-8. These three images were registered with green LEDs, and the red LEDs were shifted relative to the green LEDs. The position changes can be clearly seen from these images.

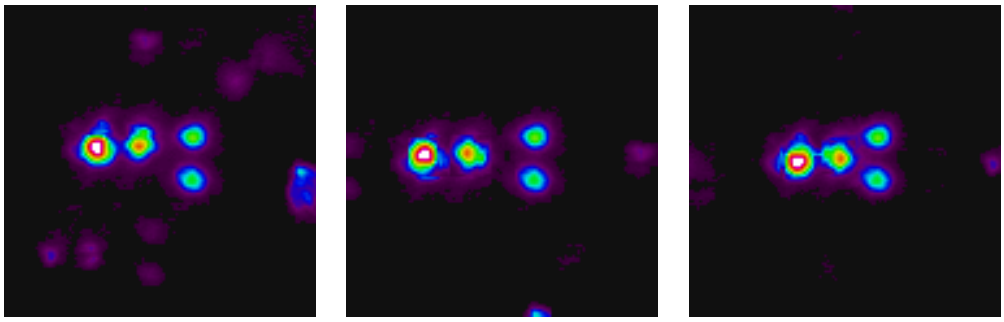

(a) down shift (b) right shift (c) left shift

Figure 6-8 3 multiple-spectral distorted images

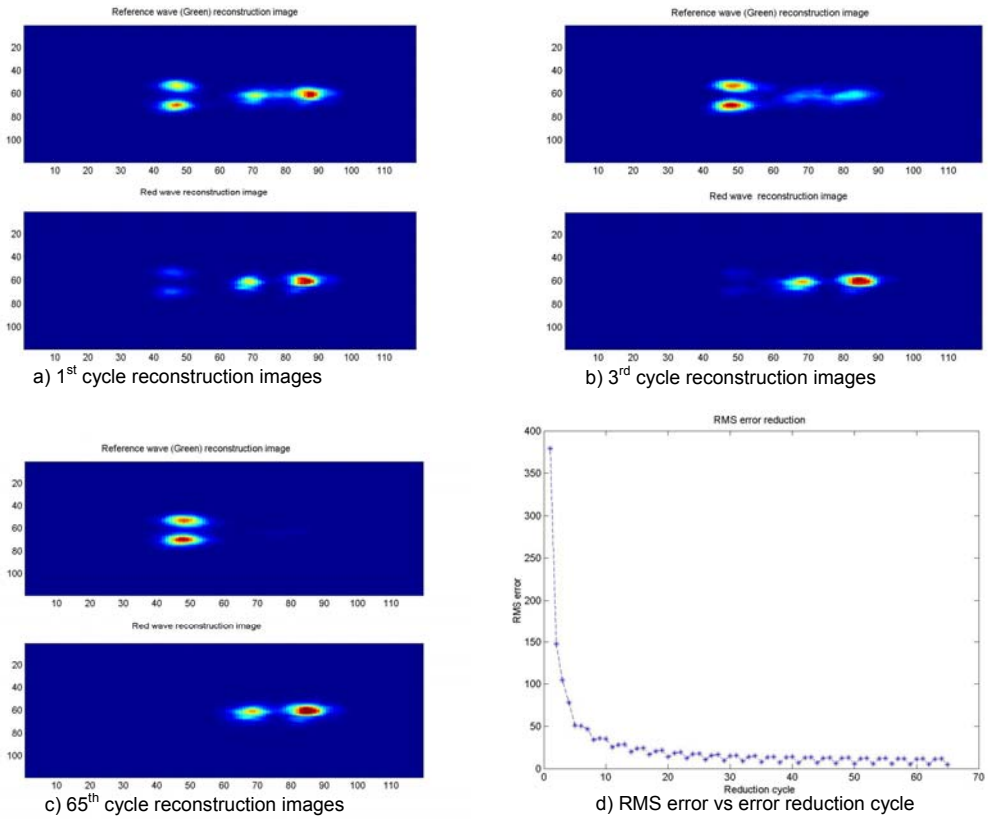

Figure 6-9 reconstructed multiple-spectral information

These images were processed with the hyper-spectral information reconstruction algorithm described in chapter 3. The reconstructed multi-spectral images are shown in figure 6-9 for various numbers of iteration cycles. The first several iterations dramatically decrease the RMS error and the four LEDs are clearly separated based on the different color.

6.2.3. Performance demonstration with a hyper-spectral object

A variety of complicated hyper-spectral objects was constructed by printing color dye onto a transparency film. Two squares were printed in a diagonal direction with green dye. The film was attached to a metal mask with the same opening windows. The metal mask only passes the light through the squares, blocking the light passing through the other area of the film. There are four small alignment holes in the metal mask around the open windows, passing the white light for information channel calibration and image registration. The object is shown in figure 6-10.

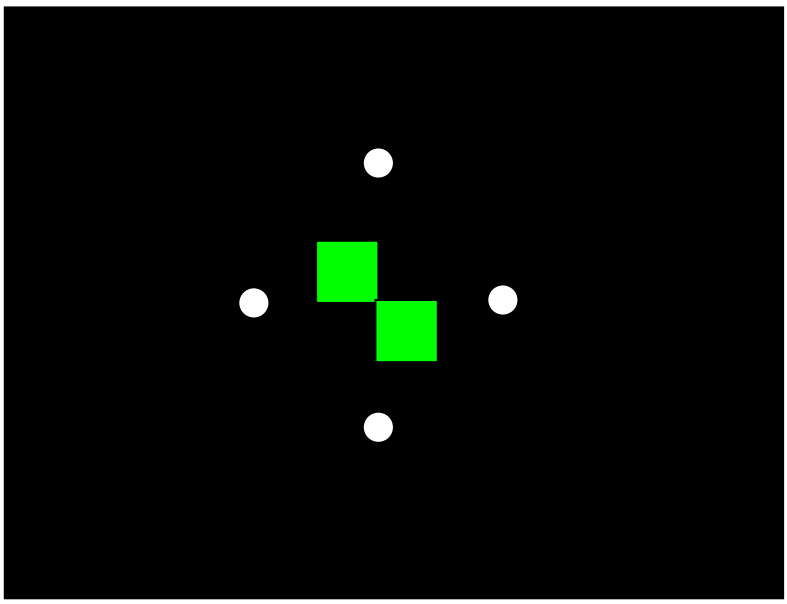

Figure 6-10 Constructed hyper-spectral object

The white light source spectral was measured with a monochrometer. The Green dye and red dye spectral transmittance were also measured as shown in figure 6-11.

The single sensor was rotated to eight different azimuthal angles and three of the output images are shown in the figure 6-12. At every rotation angle, three images were

collected: one with the object and a 525 nm narrow bandpass filter, one with the object and a 625 nm narrow bandpass filter, and one with the object only (shown in figure 6-13). The first two images were used to calibrate the information channel azimuthal angle and register the images.

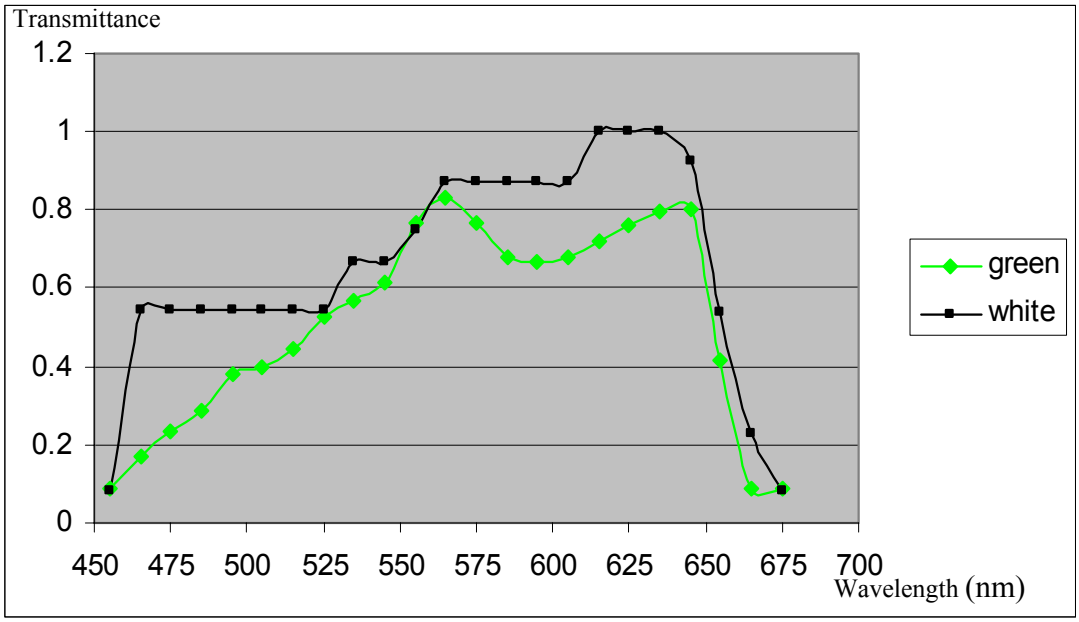

Figure 6-11 Hyper-spectral object spectral response measured with a monochrometer

After the azimuthal angle calibration and image registration, the image can be further cleaned by removing the camera background noise, as shown in figure 6-14 (a) and (b). Based on measured white light and green dye spectral information, the ideal spectrally dispersed images were simulated as shown in figure 6-14 (c).

The hyper-spectral information reconstruction was carried out base on the following three data sets: unfiltered original output image, images with noise filtering,

and the simulated ideal spectrally dispersed images. The last image can be used to predict the best achievable reconstructed spectral information. The data set without background noise are expected to be better reconstructed than the original images.

In figure 6-15, the left column constrains the green dye spectral information and the right column constrains the white light spectral. They all follow the true spectral shape with some errors. As expected, the one without the background noise generates the better spectral response than the original images.

The reconstructed spectral information based on the ideal images also shows the large deviation from the measured spectral. The primary reason for this is: with more than 40x40 spatial points and 13 spectral bins, the spatial/spectral bandwidth product of this experiment is too large for this linear algorithm, as predict by the computer model in Chapter 3. A stronger algorithm such as maximum-likelihood algorithm should be used to achieve better resolution.

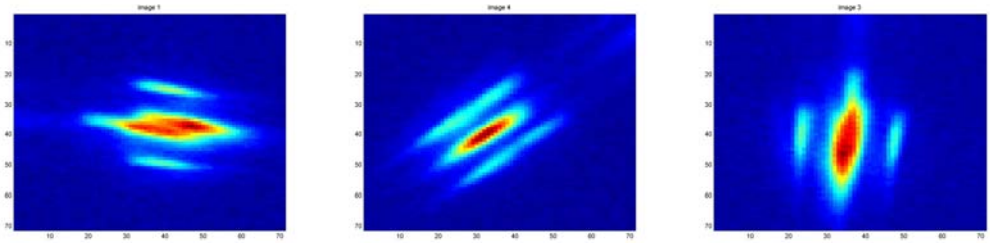

(a) 10° (b) 55° (c) 100°

Figure 6-12 Spectrally dispersed images at different azimuthal angles

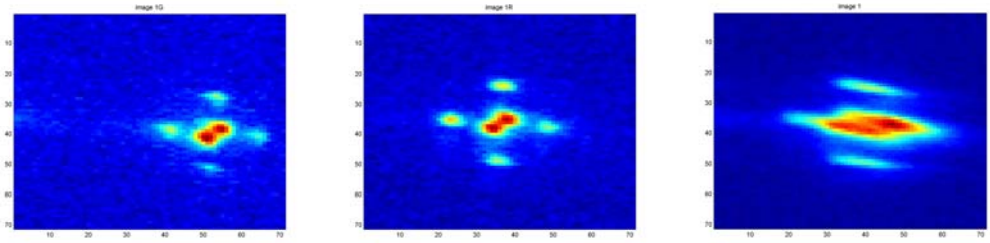

(a) (b) (c)

Figure 6-13 Collected hyperspectral data: (a) Image from the object and 525nm filter, (b) image from the object and 625nm filter, (d) image from the object only

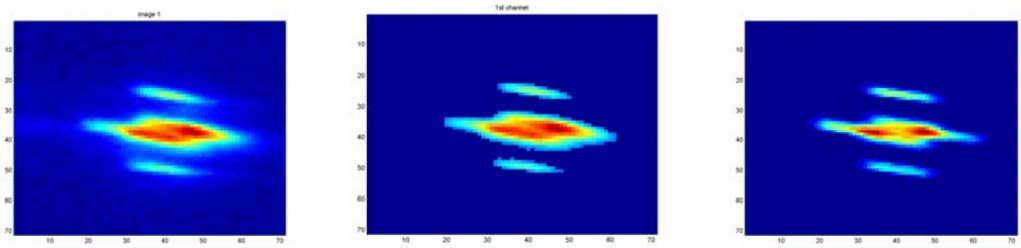

(a) (b) (c)

Figure 6-14 Data used in reconstruction algorithm: (a) True output image, (b) image with background noise removed, (c) generated ideal output

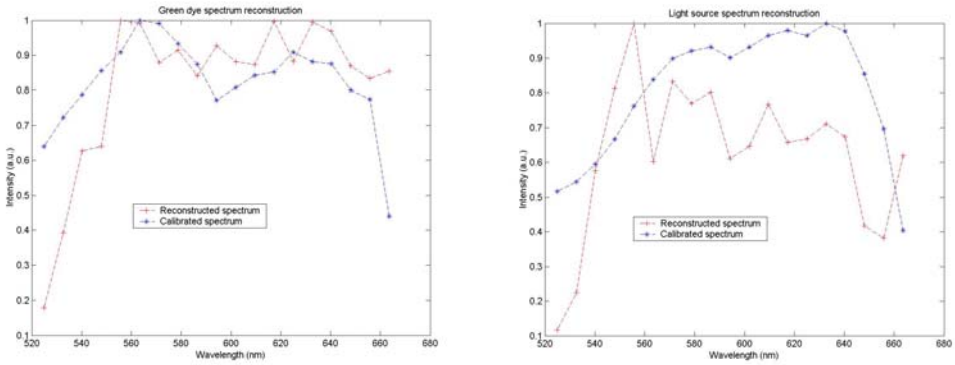

(a) Reconstructed green dye and white light spectral based on the original images

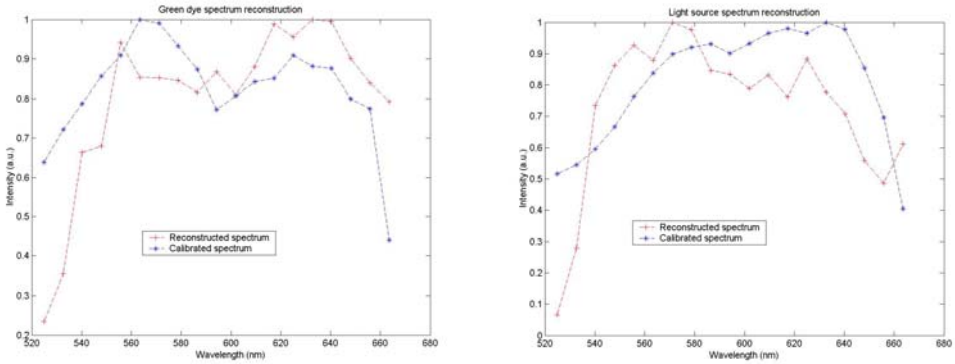

(b) Reconstructed green day spectral based on the images without background noise

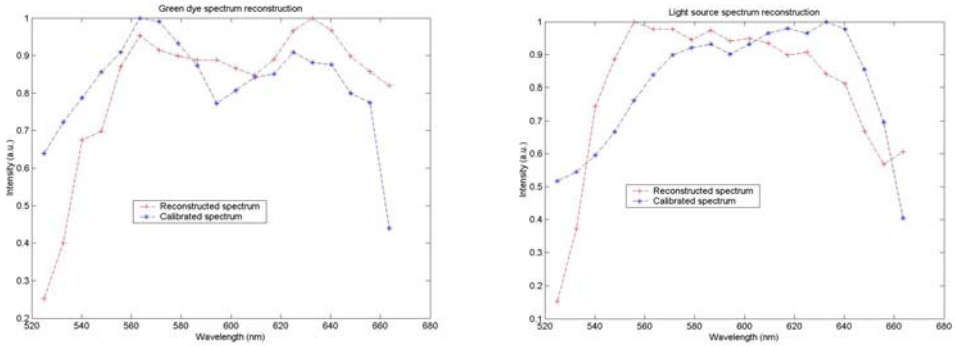

(c) Reconstructed green day spectral based on the ideal images

Figure 6-15 Reconstructed green dye and light source spectral information based on these three data sets.

7. Conclusions and future work

7.1. Conclusions

A novel micro-imaging spectrometer design methodology is presented in this dissertation. The Computer-Tomography concept is adopted for non-scan mode hyper-spectral information detection. A miniaturized sensor structure is the primary objective of this project, and spectral and spatial resolution was thoroughly studied. A simple but efficient hyper-spectral information reconstruction algorithm was built to help understanding the fundamental theory of the CTIS sensor and evaluate the micro sensor's performance. One CTIS sensor was designed with sixteen independent information channels in a 1 mm x 1 mm x 2 mm cube. One information channel was fabricated and tested with a variety of hyper-spectral objects. We successfully retrieved hyper-spectral information, which match the theoretical prediction very well.

A simple algorithm based on an optimized-error-redistribution concept was developed to study the relationship between CTIS sensor resolution and the objects' spatial and spectral frequency distribution. A CTIS sensor design rule is deduced to describe the relationship between the required information channel numbers and the desired hyper-spectral resolution.

In order to achieve minimum sensor physical size in three spatial directions, an "independent information channel" concept was defined and a sensor array architecture was utilized. Refractive, diffractive and graded index (GRIN) optics were combined into a single optical element with advanced micro-fabrication technology. An imager was constructed to provide the required spectrally dispersed imagery. By using commercially

available GRIN rod lenses, one compact CTIS sensor information channel was designed and demonstrated successfully.

7.2. Future work

In this research, a commercial GRIN rod lens was utilized, while the lens' material information and refraction profile parameters were not available. In our computer model, this lens was described as a simple GRIN lens with a parabolic refractive index profile. This simple model was not able to predict the true GRIN lens aberrations resulting in an optical system design and optimization with some uncertainty. Even though the experiment showed near diffraction limited imaging ability, a rigorous lens study should be able to improve the sensor's performance.

Because of the physical size of the individual optical element, the opto-mechanical design is a substantial challenge. In this project, only one information channel was fabricated. By rotating this single information channel into different azimuthal angles along optical axis, multiple images with different dispersion were generated to simulate the snap-shot output of an integrated CTIS sensor with multiple information channels. Because of the non-perfect optical mechanics, the optical axis of this information channel was shifted randomly when rotated. Therefore those images had to be registered relative to each other before they could be used for hyper-spectral information reconstruction. This additional image registration process inevitably introduces certain registration errors that degrade the system detection resolution. So for rigorous system performance

evaluation, a CTIS sensor with multiple information channels should be fabricated and tested for the detection.

The hyper-spectral information reconstruction algorithm developed in this project was chosen for its simplicity. However, more complex algorithms have been shown to be better suited to images with large special points and spectral bandwidth products. In addition, these algorithms are less sensitive to system noise. So in order to achieve an efficient sensor, a better information retrieval algorithm should be developed.

Reference:

[1] Newton, I. (1704) *Opticks*, (London: Royal Society).

[2] Fraunhofer, J. (1817) Denkschriften der Müch. Akademie der Wissenchaften 5, 193.

[3] Freek, D. (2001) "Imaging Spectrometry: Basic principles and prospective applications" Kluwer Academic Publishers

[4] Davis, R.M. and Niblack, C.A. (1987) "Design and test of the airborne visible/infrared imaging spectrometer (AVIRIS) focal plane assemblies," Proc. SPIE 782, 142-146.

[5] Basedow, R.W., Carmer, D.C., and Anderson, M.E. (1994) "HYDICE system: implementation and performance," Proc. SPIE 2480, 258-267.

[6] Elvidge, C.D. (1988) "Vegetation reflectance feature in AVIRIS data", proceedings of the 6th Thematic conference: remote sensing for exploration Geology, pp. 169-182

[7] Gaddis, L.R. etc, (1996) "Decomposition of AVIRIS spectra: extraction of surface-reflectance, atmospheric and instrumental components", IEEE trans. Geosci. Rem. Sens., 34, 163-178

[8] Chen, S.Z. etc, (2000) "Remote sensing and GIS for urban growth analysis in China" Photogrammetric Egnineering and Remote Sensing, 66, 593-598

[9] Morgan, R.P.C. (1995) "Soil Erosion and Conservation" Addison Wesley Longman Ltd,. Essex, 198 pp.

[10] Grant, W.B., etc., (1992) "Optical remote measurement of toxic gases" Journal of air waste manag. Assc., Vol. 42, 19,

[11] Carrasco, O. etc., (2003) "Hyperspectral imaging applied to medical diagnostics and food safety" SPIE, 2003

[12] Gat, N., etc., (1996) "Spectral imaging spplications: remote sensing, environmental monitoring, medicine, military operations, factory automation and manufacturing" SPIE vol. 2962,

[13] Shields, E., etc., (2007) "Microelectromechanical system-based adaptive space-variant imaging microspectrometer" Applied optics, Vol. 46, Iss. 31, pp.7631-7639

[14] Heidner, R.F., (1998) "Hyperspectral imaging from space: principles, status and utility forecast" Aerospace corp.,

[15] Lohmann, A.W., (1989) "Scaling laws for lens systems", Applied Optics, Vol. 28, No. 23, PP. 4996-4998

[16] Birk, R.J. etc., (1994) "Airborne hyperspectral sensor systems," IEEE Aerospace Electron. Sys. 9(10), 26-33.

[17] Chai, S.M., etc,. (2000) "Focal-plane processing architectures for real-time hyperspectral image processing," Appl. Opt. 39(5), 835-849.

[18] Jahns, J., etc., (1989) "*Planar integration of free space optical components*," Appl. Opt. 28(9), pp.1602-1605

[19] Syms, R.R.A. (2002) "Scaling laws for MEMS mirror-rotation optical cross connect switches" J. lightwave technology, 20, pp. 1084

[20] Koester, D., etc., (2003) "PolyMUMPs Design Handbook" MEMSCAP

[21] Sloane, N.J.A., etc., (1969) "Codes for multiplex spectrometry" Applied optics, 8, 2103-2106

[22] Okamoto, T., ect., (1993) "Simultaneous acquisition of spectral and spatial intensity distribution" Appl. Spectrosc. 47, 1198-1202

[23] Mooney, J.M., (1994) "Spectral imaging via computed tomography" In Proceedings of Infrared Information Sympoisa (IRIS) Specialty Group on Passive Sensors, Vol. 1, pp 203-215

[24] Betremieus, Y., etc., (1993) "SPINR: two-dimensional spectral imaging through tomographic reconstruction" Opt. Eng. 32, 3133-3138

[25] Wall, B.F., etc., (1997) "Revised radiation doses for typical x-ray examinations" British Journal of radiology, 70(833), 437-439

[26] Deans, S.R. (1983) "The Radon transform and some of its applications" New York: John Wiley & Sons

[27] Shannon, C.E. (1949) "Communication in the presence of noise" Proc. IRE, pp. 10-12

[28] Jerri, A.J. (1977) "The Shannon sampling theorem—its various extensions and applications: a tutorial review" proceedings of the IEEE, 65. 1565-1595

[29] Kak, A.C., etc., (1987) "Principles of computerized tomographic imaging" IEEE press, New York

[30] Nguyen, M.K., etc., (2003) "On a generalized X-ray transform and a new method for defect detection using the medium electronic density" Comptes rendus methematique, Vol. 336, Iss. 2, pp. 195-200

[31] Wang, G., etc., (1993) "A general cone-beam reconstruction algorithm" IEEE trans. Med. Imaging, 12, 486-496

[32] Katsevich, A., (2003) "A general scheme for constructing inversion algorithm for cone-beam" Med. Phys. 30, 3217-3226

[33]Smith, B.D. (1985) "Image reconstruction from cone-beam projections: necessary and sufficient conditions and reconstruction methods" IEEE trans, Med. Imaging MI-4, 14-25

[34] Myung, I.J. (2002) "Tutorial on maximum likelihood estimation" Journal of Mathematical Psychology 47, pp. 90-100

[35] Borah, D.K., etc., (2006) "Maximum-likelihood estimation of a laser system pointing parameters by use of a return photon counts" Applied Optics, Vol. 45, No. 11, pp. 2504-2509

[36] Descore, M., etc., (1995) "Computerd-tomography imaging spectrometer: experimental calibration and reconstruction results", Applied optics, Vol. 34, No. 22, PP. 4817-4826

[37] Ford, B., etc., "Large-image-format computed tomorgraphy imaging specgrometer for fluorescence microscopy" optics express, Vol. 9, Iss. 9, pp. 444-453

[38] Iga, K., etc., (1984) "Fundamentals of microoptics: distributed-index, microlens, and stacked planar optics" Tokyo, Orlando: Academic press,

[39] Hu, W.S., etc., (1998) "Reduction of coupling loss in a one-to-many collimating system for a wavelength division multiplexer" Applied optics, Vol. 37, iss. 19, pp. 4084-4090

[40] Zickar, M., etc., (2006) "MEMS compatible micro-GRIN lenses for fiber to chip coupling of light" Optics express, Vol. 14, Iss. 10, pp. 4237-4249

[41] Chanclou, P., etc., (2005) "Optical fibered variable attenuator using phase shifting polymer dispersed liquid crystal" Optics communications, Vol. 248, Iss. 1-3, pp. 167-172

[42] Shiraishi, K., etc., (2005) "A micro light-beam spot-size converter using a hemicylindrical GRIN-slap tip with high index contrast" J. Lightwave Technol. 23, 3821

[43] Carlos, G.R., etc., (2002) "Gradient-index optics" Springer

[44] "SELFOC Product Catalog" NSG America Inc.

[45] Huang, W.P. (1994) "Coupled-mode theory for optical waveguides: an overview" J. Opt. Soc. Am. A, 11, 963-983

[46] Stauffer, J.M., etc., (1992) "Electron beam writing of continuous resist profiles for optical applications," J. Vac. Sci. Technol. B. 10(6), 2526-2529.

[47] Larsson, M., etc., (1994) "Successive development optimization of resist kinoforms manufactured with directwriting, electron-beam lithography," Appl. Opt. 33(7), 1176-1179.

[48] Owen, G. (1990) "Methods for proximity effect correction in electron lithography," J. Vac. Sci. Technol. B. 8(6), 1889-1892.

[49] Parikh, M. (1980) "Proximity effects in electron lithography: magnitude and correction techniques," IBM J. Res. Dev. 24(4), 438-451.

[50] Dubonos, S.V., etc., (1993) "Evaluation, verification and error determination of proximity parameters alpha , beta and eta in electron beam lithography," Microelectron. Eng. 21(1-4), 293-296.

[51] Nikolajeff, F., etc., (1995) "Measuring and modeling the proximity effect in direct-write electron-beam lithography kinoforms," Appl. Opt. 34(5), 897-903.

[52] Aparshina, L.I., etc., (1997) "Energy dependence of proximity parameters investigated by fitting before measurement tests," J. Vac. Sci. Technol. B. 15(6), 2298-2302

[53] MicroChem Corp.

[54] Raith GmbH, Dortmund, Germany

[55] Hirasawa, S. etc., (1997) "Analysis of drying shrinkage and flow due to surface tension of spin-coated films on topographic substrates" IEEE trans. on semiconductor manufacturing, Vol. 10, No. 4, pp. 438-444

[56] Matsui, S. (1993) "Cross-sectional observation of resist patterns by focused ion beam etching" Nanotechnology, 4, pp. 170-174

[57] Stanishevsky, A., etc., (1998) "Focused ion-beam patterning of nanoscale ferroelectric capacitors" Journal of vacuum science & technology B: Microelectronics and nanometer structures, Vol. 16, iss. 6, pp. 3899-3902

[58] Irani, M., etc., (1991) "Improving resolution by image registration" CVGIP: Models image process, 6, 1646-1658